MANCHESTER 1824

The University of Manchester

Engineering Novel Porous Materials for Carbon Capture and Storage

A thesis submitted to The University of Manchester for the degree of Doctor of Philosophy
in the Faculty of Science and Engineering

2017

Nadeen Al-Janabi

School of Chemical Engineering and Analytical Science

Table of Contents

Word count: 47,973

List of Tables

List of Figures

The University of Manchester

Abstract of thesis submitted by **Nadeen Al-Janabi** for the degree of **Doctor of Philosophy** and entitled "**Engineering novel porous materials for carbon capture and storage**" in the year **2017**.

Global warming along with the climate change derived from the World's demand for energy are among the greatest challenges to our society. To tackle climate change issue, research must focus on proposing practical approaches for carbon emissions reduction and environmental remediation.

This thesis focuses on carbon dioxide separation mainly from flue gases (major sources of carbon dioxide emissions) using metal organic frameworks (MOFs) to reduce its impact on the global warming hence the climate change. MOFs are a class of crystalline porous adsorbents with structures that attract CO_2 selectively and store it in their porous frameworks.

Over the course of this PhD research, the fundamental aspects of these materials, as well as their practical applications, have been investigated. For example, the synthesis recipe of copper (II) benzene-1,3,5-tricarboxylate (CuBTC) MOF was improved to deliver a product of high yield (> 89%) and free of by-product. Also, a mechanism study on the hydrothermal stability CuBTC MOF was carried out under simulated flue gas conditions and delivered the first experimental proof of the decomposition mechanism of CuBTC MOF caused by the water vapour. The fundamental understanding of the stability of materials then motivated the research into the development of a facile method of using an economic functional dopant (*i.e.* glycine) to strengthen the structure of CuBTC MOF (completely stable towards water vapour), as well as to improve the selectivity of resulting materials to CO_2 (by 15% in comparison to the original CuBTC MOF). The suitability of the CuBTC MOF for fixed bed adsorption processes was also assessed using a combined experimental and process simulation method.

In addition to the experimental approaches, molecular simulation based on grand canonical Monte Carlo method was also used to understand the effect of structural defects of MOFs on the CO_2 adsorption isotherms.

Declaration

I declare that this research is the result of my own work except as cited in the references and no portion of this work has been submitted in support of an application for another degree of qualification of this or any university or other institute of learning.

Copyright

Acknowledgements

First and foremost I would like to express my sincere gratitude to my main supervisor, Dr Xiaolei Fan. Undertaking this PhD would not have been achievable without his knowledge, his guidance, his advice and his support. I would like to acknowledge him for motivating and encouraging me to grow as a research scientist. I would not have imagined having a better supervisor for my PhD.

Besides my main supervisor, I would like to convey my special appreciation and gratitude to my co-supervisor, Dr Flor R. Siperstein. I am so grateful to her for being a great mentor for me.

Thanks must also be extended to Dr Arthur Garforth who was my internal assessor in the first and second year of this PhD. His wise advice and the interesting discussions we had helped me a lot in my work.

I am also so grateful for the staff at The University of Manchester who made some experimental instruments available for me to use, Prof Roger Davey, Dr Stuart Holmes, Dr Patricia Gorgojo and Dr Patrick Hill. Also, I would like to thank Dr James Raftery, Dr Abdullatif Alfutaimi, Dr Joanna Stevens, Dr Aleksandra Gunciaruk, Dr Sara Sorribas, Sharlinda Binti Salim and Shahla Khan for training me to use the laboratory instruments during my PhD.

Also, a special thank goes to the technicians at the School of Chemical Engineering and Analytical Science, Mr Loris Doyle and Mr Craig Shore for their help and assistance.

I wish to thank all my friends, my colleagues and especially my officemates for their support and for making an enjoyable environment.

I am so grateful to my wonderful family; my aunt, my parents, my sisters and my brother for their love which made me feel them close to me despite the distance. I want to thank them for their encouragement, their caring and for helping me in any way they could.

Finally, I would like to thank the Higher Committee for Education Development in Iraq (HCED) for sponsoring my PhD scholarship.

Chapter 1

Background, motivation and achievements

1.1 *CO_2 emissions and climate change*

Carbon Dioxide (CO_2) is a greenhouse gas emitted to the environment naturally by the carbon cycle in the Earth, in addition to various human activities such as fuel burning for energy/electricity generation, transportation and industry. CO_2 emission is the major contribution to the global warming, *ca.* 60% [1], and the average CO_2 concentration in the atmosphere keeps increasing over the decades. It is now reaching about 400 parts per million by volume (ppmv), exceeding the acceptable pre-industrial level of about 300 ppmv [2].

The Intergovernmental Panel on Climate Change (IPCC) predicted that by the year of 2100, the amount of CO_2 in the atmosphere might reach values of up to 570 ppmv. This increase can cause the mean global temperature to rise by 1.9 °C and the mean sea level to increase by 3.8 m [3, 4]. The climate response to carbon emission is estimated at roughly 1–2.1 °C per 3600 gigatonnes (Gt) of CO_2 emitted to the atmosphere [5].

Therefore, a big concern has been raised for CO_2 depletion, by developing of relevant CO_2 capture and storage technologies known as CCS, in order to reduce CO_2 emission and accordingly the average atmospheric CO_2 level to 350 ppmv [4]. In addition to reducing the contribution of CO_2 to the global warming from 60% to 19% by 2050 [6]. Furthermore, Paris agreement [7] added urgency to CCS development to keep the global temperature from rising above the pre-industrial level by 1.5 °C. After 2050, the net negative emission is needed in order to reduce the risk of not matching the climate goals in addition to the reduction of the cost required to achieve the emissions' reduction by 2100 [8]. The IPCC's Fifth Assessment Synthesis Report [8] stated that '*the net negative emissions can be*

accomplished if more greenhouse gases are sequestered than released to the atmosphere, for example, by using bioenergy in combination with CCS'.

According to the Global CCS Institute, there are globally 15 large-scale CCS projects in operation and 7 more under construction [9], with total capture capacity of CO_2 of around 40 million tonnes of CO_2 per annum (Mtpa). The Global CCS Institute Report also indicated that 6 more large-scale CCS projects are at advanced stages of project planning with 6 Mtpa total CO_2 capture capacity and 12 more large-scale projects with 25 Mtpa total CO_2 capture capacity are in earlier stages of project planning [9].

In CCS technology, CO_2 is separated from other gases, then; the mostly pure CO_2 is either used later for enhancing the oil recovery or be securely stored underground in the depleted oil and gas fields or deep saline aquifer formations. However, an alternative to CCS, carbon capture and utilisation (CCU), is also being widely considered. CCU technology is a process that uses CO_2 for the chemical industry, where CO_2 molecules are converted into molecules such as urea, carbonates, carbamates and polymers [10]. It should be noted that this thesis mostly focuses on CO_2 separation stage regardless the following stage of either storing or utilising the separated CO_2.

1.2 *Separation of CO_2 from emitted gases*

In order to reduce the CO_2 emission from fuel combustion processes, three approaches have been proposed for carbon depletion as shown in Figure 1.1, where: (*i*) CO_2 can be captured from the resultant stream out of combustion chamber, *i.e.* post-combustion capture, (*ii*) it can be separated from the designated separation unit (after the fuel gasifier-reformer) to yield syngas, which is then burned for heat and power generation, *i.e.* pre-combustion capture and (*iii*) combustion with pure O_2 is also being developed, *i.e.* oxy-fuel combustion, where the combustion with pure O_2 rather than with air gives nearly pure CO_2 as the combustion product [1, 3, 11].

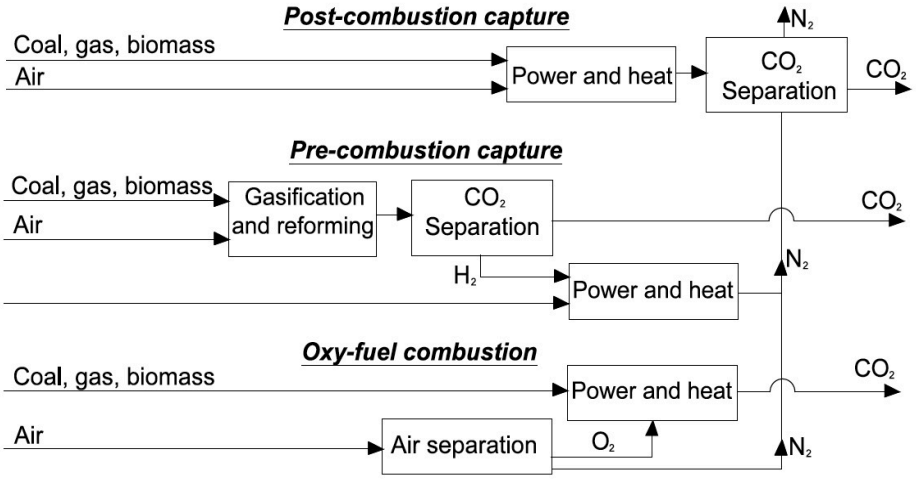

Figure 1.1. CO_2 capture technologies, adapted from reference [1].

Each capture technology has advantages and drawbacks. Pre-combustion capture has the advantage of low energy requirements. However, the efficiency of the turbine with hydrogen fuel is low, and the associated capital cost (*i.e.* for new constructions) is high with the public resistance to the bigger footprint of plants. The oxy-fuel method has the advantage of producing nearly pure CO_2 which can be directly stored. However, it requires pure oxygen and also high capital cost [11]. The post-combustion treatment is the most promising approach since (*i*) it can be easily retrofitted to the existing power plants and (*ii*) it is the only process in which the CO_2 capturing unit does not jeopardise the power generation processes [3, 11].

At present, the commercially available post-combustion CO_2 capture process is the chemical amine-based absorption. Although this process is the most mature technology, it has several drawbacks, such as: (*i*) the requirement for large size equipment (leading to high capital cost), (*ii*) high equipment corrosion rate (leading to high maintenance cost), and (*iii*) large demand for make-up solvent due to the continuous degradation of amine in the presence of O_2, SO_X, and NO_X [1, 3]. Furthermore, the cost of solvent regeneration is also considerable, accounting for about 70–80% of the overall operating cost of the system [3], because of the high regeneration temperature required of about 120 °C [12].

Due to the aforementioned drawbacks of absorption processes involving liquid, research attention has been given to developing membrane separation and

adsorption processes with solid porous materials as alternatives to the current liquid-phase CO_2 capture processes. Membrane separation uses a composite polymer composed of a selective thin layer bonded to a non-selective thicker and low cost layer to mechanically support the membrane. The membrane selectively permeates the desired gas (*e.g.* CO_2), while retains the unwanted, resulting in separation of the gas mixture constituents. Membrane separation possesses several advantageous such as it is ideal as an energy saving process, the equipment is simple, compact, easy to operate and control and is easy to scale up. However, low CO_2 partial pressure (*e.g.* in flue gas) represents the main hurdle for this process due to the low driving force for separation [13, 14].

Adsorption processes using solid adsorbent have several potentials for CO_2 capture, such as their ease of handling [1] and high adsorption capacity with high selectivity. For example, a magnesium-based metal organic framework solid adsorbent (Mg-MOF-74) showed high CO_2 adsorption capacity of 8.61 mmol/g at 25 °C and 1 bar [15]. Also, less energy is usually required for the regeneration of solid adsorbents due to the low regeneration temperature at about 60 °C [1, 12]. Therefore, different porous 'adsorbents' have been explored for CO_2 capture such as inorganic porous carbon, zeolites, metal organic frameworks (MOFs), polymers of intrinsic microporosity, etc.

The design of porous materials for CO_2 separation should be focused not only on their intrinsic adsorption capacities and selectivities but also on their potentials for practical applications, in which some adsorbent may suit a particular application but not another. For example, as a major class of porous materials proposed for CO_2 capture, zeolites such as 13X (or NaX) showed good adsorption capacities for CO_2, *e.g.* 5.5 mmol/g at 30 °C and 20 bar [16]. However, zeolites are highly influenced by the presence of water vapour in the feed stream due to the formation of bicarbonates on their surfaces [1]. On the other hand, porous materials can also be structured as thin sheets to be used as membrane materials or as a part of mixed matrix membrane (polymer matrix doped with solid porous materials) [17, 18]. Both methods have advantageous of the higher mechanical and thermal stabilities compared to polymers as well as higher permeabilities allowing a smaller layout and investment cost than polymer membranes [17].

1.3 *Research motivation, thesis outline and outputs*

The global emissions of CO_2 undoubtedly lead to global warming with considerably negative influences on ecology, farming, food supply, wellbeing and economy. Carbon capture from various resources is one of the solutions to tackle the global warming issue, in addition to the use of renewable energy resources and increase the energy efficiency. The development of new porous materials has shown that MOFs, as an emerging class of porous materials, possess the potential to make an effective impact in gas adsorption and separation, especially for CO_2 capture. But, investigation in the area of assessing MOFs' capability and suitability for industrial applications is still required.

The work presented in this thesis focuses on the development and evaluation of MOFs-based adsorbents for practical CO_2 capture. CuBTC MOF (or HKUST-1, HKUST represents the Hong Kong University of Science and Technology) was reported by Chui *et al.* in 1999 [19]. CuBTC MOF was chosen as the model MOF in this work because of its desirable framework characteristics such as its *(i)* ease of synthesis, *(ii)* high BET surface area of > 2000 m^2/g [20], *(iii)* thermal stability of up to 350 ºC [21], and *(iv)* moderate hydrothermal stability (steaming conditions: 28.9% relative humidity at 180 ºC) [22]. CuBTC framework is composed of copper metal nodes (the inorganic part) and benzene tri-carboxylate (BTC, the organic ligands). These two parts form cubic units porous cells that have two types of primary pores with *ca.* 11 and ~13 Å diameter, secondary pores (or side pockets) with *ca.* ~5 Å diameter and triangular windows (for connecting primary and secondary pores) with *ca.* 3.5 Å diameter [23, 24]. The molecular structure of CuBTC MOF is shown in Figure 1.2.

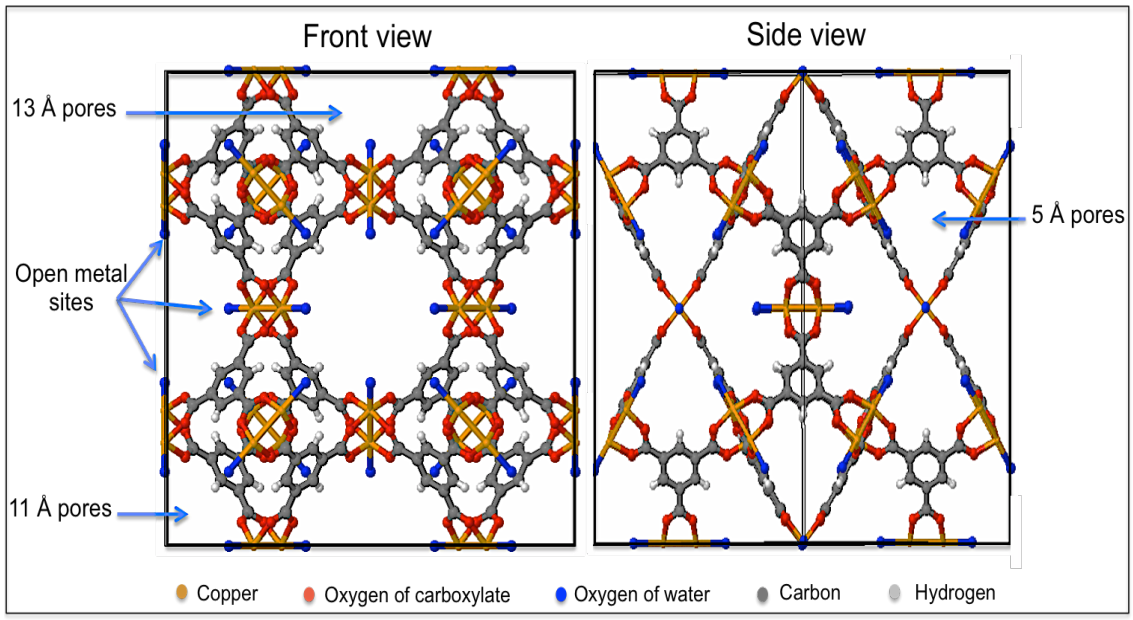

Figure 1.2. A front and side view of the molecular structure of CuBTC MOF.

1.4 *Thesis structure*

This thesis is presented in journal format, according to the thesis submission guidelines approved by The University of Manchester[1].

Chapter 2 provides a general literature review including commonly studied solid adsorbents for CO_2 capture, as well as a description of metal organic frameworks structure, design, synthesis and modification. Grand Canonical Monte Carlo (GCMC) molecular simulation and process modelling are also discussed in brief.

Chapter 3 presents an improved hydrothermal synthesis method of CuBTC MOF. The reaction time was reduced by more than 90% of the reported synthesis time with no formation of by-products. Additionally, the synthesis yield was increased to 89.4%, which is the highest reported one in the literature so far for batch synthesis. Detailed characterisation of the structure of the synthesised sample is given along with the pure CO_2 and N_2 adsorption data simulating flue gas emissions conditions.

[1] http://documents.manchester.ac.uk/display.aspx?DocID=7420

In Chapter 4, detailed analysis of the structural hydrothermal stability of CuBTC MOF, under various temperatures and water vapour partial pressures, is given. CuBTC MOF was also characterised using cyclic water vapour experiments to assess its stability under natural gas or flue gas emissions conditions. Furthermore, the effect of the exposure time to water vapour and outgassing condition on the adsorption behaviour and structure properties of CuBTC MOF was also studied.

Based on the decomposition mechanism explained in Chapter 4, CuBTC MOF structure was modified to enhance its hydrothermal stability while maintaining its CO_2 capture properties, which is given in Chapter 5. A dopant molecule of glycine was used to modify CuBTC MOF by saturating the copper centres and preventing water molecules from destroying their bonds to the organic ligands. The new MOF (denoted as Gly-CuBTC) was characterised experimentally to determine its structural properties. Gly-CuBTC MOF was found to be hydrothermally stable with improved CO_2:N_2 selectivity compared to the parent CuBTC MOF.

Chapter 6 provides a detailed analysis of the effect of the propagation velocity of mass transfer zone on the breakthrough curves and adsorption isotherms using fixed bed column. Three porous solids were used; bulk activated carbon, bulk CuBTC MOF and pelleted CuBTC MOF for CO_2 separation from a CO_2/N_2 mixture. A combined approach of experimental and numerical study was used showing that CO_2 adsorption behaviour of materials in a fixed bed column is different from that measured by the gravimetric method. These results suggested that, in addition to the equilibrium measurement, the evaluation of porous materials for adsorption applications should be complemented by the fixed bed experiments for a fair evaluation.

In Chapter 7, a quantitative method for assessing the defects originated during synthesis in MOFs structures is presented based on grand canonical Monte Carlo (GCMC) simulations. CuBTC MOF was used as the model material to show the effect of different pores blockages on the measured adsorption isotherms. The presented method is generic and can be applicable to other materials, showing that the combination of experimental study with molecular simulation can be used to identify the defective features of solid porous materials.

In Chapter 8, a summary of the main findings is presented with recommendations for future works.

The content presented in this thesis has been previously published and/or presented in several peer-reviewed journals, national/international conferences and research seminars, as follows:

1.4.1 Publications

1. N. Al-Janabi, H. Deng, J. Borges, X. Liu, A. Garforth, F. Siperstein, X. Fan, A facile post-synthetic modification method to improve hydrothermal stability and CO_2 selectivity of CuBTC metal-organic framework, *Ind. Eng. Chem. Res.*, DOI: 10.1021/acs.iecr.5b04217, 4 times cited.
2. *N. Al-Janabi, X. Fan, F. Siperstein, Assessment of MOF's quality: quantifying defect content in crystalline porous materials*, J. Phys. Chem. Lett., *7 (8) (2016) 1490,* 4 times cited.
3. N. Al-Janabi, A. Alfutaimi, F. Siperstein, X. Fan, Underlying mechanism of the hydrothermal instability of $Cu_3(BTC)_2$ metal-organic framework, *Front. Chem. Sci. Eng.*, 10 (1) (2016) 103. (Cover story), 4 times cited.
4. N. Al-Janabi, P. Hill, L. Torrente-Murciano, A. Garforth, P. Gorgojo, F. Siperstein, X. Fan, Mapping the Cu-BTC metal-organic framework (HKUST-1) stability envelope in the presence of water vapour for CO_2 adsorption from flue gases, *Chem. Eng. J.* 281 (2015) 669. This publication has been cited 21 times. It was listed as ***hot paper*** and ***highly cited paper*** on Web of Science, 2016. It also received the media mention in Industry Today.

Publications not included in this thesis:

1. P. Hester, S. Xu, Wei Liang, N. Al-Janabi, R. Vakili, P. Hill, C. A. Muryn, X. Chen, P. Martin, X. Fan, On thermal stability and catalytic reactivity of Zr-metal-organic framework (UiO-67) encapsulated Pt catalysts, J Catal., 340 (2016) 85, 5 time cited.
2. A. Alfutaimi, N. Al-Janabi, R. Curtis, G. J. T. Tiddy, The effect of monoglycerides on the crystallisation of triglyceride, *Colloid Surf. A*, 494 (2016) 170, 2 times cited.

1.4.2 Presentations

1.4.2.1 Conference presentations

1. 'Fixed-bed adsorption for carbon capture: analysis of propagation velocity effect' in the ChemEngDay 2017, Birmingham, UK, March 2017. (**Poster**)
2. 'Carbon capture processes: from chemistry to application' in the Manchester Energy Conference, Manchester, UK, February 2017. (**Poster**)
3. 'Assessment of MOF's quality: quantifying defects content in crystalline porous materials; A case study: $Cu_3(BTC)_2$' in the 14th International Conference on Carbon Dioxide Utilisation 2016, Sheffield, UK, September 2016. (**Oral**)
4. 'Fixed-bed adsorption process for carbon capture from industry' in the 14th International Conference on Carbon Dioxide Utilisation 2016, Sheffield, UK, September 2016. (**Poster and Flash presentation**)
5. 'Porous materials for carbon dioxide capture (synthesis, characterisation and application)' in the Postgraduate Summer Research Showcase (PSRS) 2016, Manchester, UK, June 2016. (**Poster**)
6. 'Porous materials for carbon dioxide capture (synthesis, characterisation and application)' in the CEAS PGR conference, Manchester, UK, May 2016. (**Oral**)
7. 'Fixed-bed adsorption for carbon capture from industry' in the ChemEngDay 2016, Bath, UK, April 2016. (**Poster**)
8. 'Assessment of MOF's quality: quantifying defects content in crystalline porous materials; A case study: $Cu_3(BTC)_2$' in the ChemEngDay 2016, Bath, UK, April 2016. (**Poster**)
9. 'Engineering novel porous materials for selective carbon capture' in the 8th Manchester Metropolitan University PGR conference, Manchester, UK, November 2015. (**Oral**)
10. 'Novel porous materials for water remediation and carbon dioxide capture' in the ECO-systems@manchester networking and showcasing event, Manchester, UK, October 2015. (**Oral**)
11. 'Adsorption in HKUST-1: reconciliation of differences by molecular simulation' in the 38th BZA Annual Meeting, Chester, UK, July 2015. (**Oral**)
12. 'Engineering novel metallic-organic-frameworks based on HKUST-1 for selective carbon capture' in the 13th International Conference on Carbon Dioxide Utilisation, Singapore, July 2015. (**Oral**)

13. ‘Engineering novel metallic-organic-frameworks (MOFs) for carbon capture from flue gas’ in the Postgraduate Summer Research Showcase (PSRS) 2015, Manchester, UK, June 2015. (**Poster**)
14. ‘Engineering novel metallic-organic-frameworks (MOFs) based on HKUST-1 for carbon capture’ in the CEAS PGR conference, Manchester, UK, May 2015. (**Poster**)
15. ‘Engineering novel metallic-organic-frameworks (MOFs) based on HKUST-1 for carbon capture’ in the ChemEngDay 2015, Sheffield, UK, April 2015. (**Poster**)

1.4.2.2 Invited talks and posters

3. ‘Understanding the CO_2 capture from flue gases in MOFs using molecular simulation’ in The University of Manchester Postgraduate Open Day, October 2015. **(Poster)**
4. ‘Hydrothermal stability characterisation of microporous materials (Metal-organic frameworks) using dynamic vapour sorption’ in the Advances in Dynamic Vapour Sorption Methods and Surface Energy Characterisation Workshop, Imperial College London, London, UK, July 2015 (travel was paid by the organiser). **(Talk)**
5. ‘Engineering novel metallic-organic-frameworks (MOFs) based on HKUST-1 for carbon capture’ in the Joint IIT-Madras–University of Manchester Workshop, July 2015. **(Poster)**
6. ‘Hydrothermal stability characterisation of microporous materials (Metal-organic frameworks) using dynamic vapour sorption’ in the Advances in Dynamic Vapour Sorption Methods and Surface Energy Characterisation Workshop, Manchester, UK, June 2015. **(Talk)**

Chapter 2

Overview

2.1 *Porous materials for CO_2 capture*

A variety of solid porous materials have been proposed and explored for carbon dioxide capture using adsorption process. The main criteria to assess a porous material for practical adsorption application [1, 25, 26] is:

1. High CO_2 adsorption capacity, high CO_2 selectivity;
2. Fast adsorption kinetics;
3. Ease of synthesis and activation;
4. Good thermal and hydrothermal stability;
5. Tolerance to feed gas impurities;
6. Scalability;
7. Possibility for low temperature regeneration; and
8. The cost associated with synthesis, activation and regeneration.

In general, for CCS, the purity of captured CO_2 needs to be higher than 95% in order to enable the compression of CO_2 to high pressure [27]. By using Eq 2.1 [27], the working capacity of an adsorbent can be determined, and hence the suitability of the adsorbent for practical CO_2 capture can be estimated. It is worth to note that, for practical application, a suitable adsorbent for CO_2 capture should exhibit an adsorption capacity of 2–4 mmol of CO_2/g of adsorbent [1].

$$x_{CO_2} = \frac{\Delta q_{CO_2}\rho_g\left(1-\varepsilon\right) + y_{CO_2}\dfrac{\varepsilon P_{feed}}{RT}}{\Delta q_{CO_2}\rho_g\left(1-\varepsilon\right) + \dfrac{\varepsilon P_{feed}}{RT}} > 0.95 \tag{2.1}$$

where Δq_{CO_2} is the adsorbent working capacity (mol/kg), ρ_g is the grain density (kg/m^3), ε is the void fraction of the adsorption column, P_{feed} is the pressure of the feed and T is the temperature of the feed.

During the past two decades, significant efforts have been made to explore different types of porous materials, such as inorganic carbonaceous materials, zeolites, metal organic frameworks (MOFs), polymers of intrinsic microporosity (PIM) and others for gas adsorption. In this work, the focus was put on using MOFs for CO_2 adsorption because MOFs have been regarded as the new generation of porous materials for gas adsorption and separation with a combination of features of high adsorption capacity, tunable selectivity, ease of synthesis and low-cost regeneration. A comprehensive evaluation of the candidate MOF was carried out to reveal the potential for future applications in industrial processes of CO_2 capture.

2.1.1 Inorganic porous carbonaceous materials

Carbonaceous materials are available in several forms, including activated carbon (AC), graphene, carbon nanostructures such as nanotubes and nanofibers. AC is widely used for CO_2 adsorption and separation because of its high porosity, thermal stability, availability, good resistance to moisture and tunable surface chemistry [2, 28]. Activated carbon can be derived from coal, industrial by-products, wood and other biomass materials, which means the adsorption by activated carbon an attractive option due to the low cost of its raw materials [1, 28].

AC can be prepared by a two-step method including carbonisation of raw materials, which takes place at temperatures below 800 °C, and the activation of produced carbon samples, which is performed at temperatures ranging from 850–1000 °C [2, 29].

A review on solid adsorbents for CO_2 capture showed that AC has CO_2 adsorption capacity ranging from 1.53–3.23 mmol/g at 25 °C and atmospheric pressure [28]. In order to enhance the adsorption capacity of AC, various attempts have been made to modify AC, for example, Somy et al. [30] performed a post modification of a commercial AC with chromium oxide and zinc carbonate hydroxide by impregnation. With the presence of these metal oxide species, the resulting sample demonstrated a CO_2 capture capacity of 2.73 mmol/g at room temperature and atmospheric pressure whereas the original AC only showed an uptake of 1.79

mmol/g. This improvement was attributed to the introduction of basicity into the pore surface of AC promoting the adsorption of an acidic gas, *i.e.* CO_2.

Shafeeyan and co-workers [31] treated commercial carbons thermally with ammonia. They showed that CO_2 adsorption capacity could be enhanced due to the increase of the surface basicity by adding nitrogen functionalities, resulting in an increase of CO_2 adsorption capacity from 1.18 to 1.67 mmol/g at 30 °C and atmospheric pressure.

Adsorption temperature was also found to have a substantial influence on the CO_2 adsorption capacity of activated carbon [1, 31, 32]. Rashidi *et al.* [33] investigated the effect of the adsorption temperature on the CO_2 capture capacity of AC, showing that the adsorption capacity dropped significantly from 1.82 mmol/g to < 0.4 mmol/g with increasing adsorption temperature from 25 °C to 100 °C. Furthermore, activated carbon was also found to have low selectivity at a low partial pressure of CO_2, low tolerance to contamination, such as the presence of SO_X and NO_X in flue gases and weak adsorption capacity for high-pressure gases [1, 31, 32].

2.1.2 Zeolites

Zeolites are three dimensional inorganic microporous materials with well defined structures that contain a collection of silicon and aluminium joined by oxygen atoms [34]. Zeolites are considered as basic compounds with strong electropositivity that allows them to have the preferable interaction with the adsorbate with acidic character such as CO_2 [16].

Bonenfant *et al.* [16] reviewed several zeolites that were used for CO_2 capture such as zeolite 5A, 13X (or NaX) and M-ZSM-5 (M = Li, Na, K, Rb, Cs). Where, zeolite 13X showed the highest adsorption capacity of 3.4 mmol/g at 25 °C and atmospheric pressure. They concluded that the variation in CO_2 adsorption capacity of different types of zeolites depends on their pore sizes and Si:Al ratio (low Si:Al zeolite ratio leads to the increase of the basicity of zeolites' surfaces, hence higher CO_2 adsorption capacity).

Post treatment of zeolites was also investigated to improve the CO_2 adsorption capacity of zeolites, *e.g.* treating zeolites with an aqueous solution of amines to introduce alkaline groups onto zeolites surfaces [35, 36]. Su *et al.* [36] employed tertraethylenepentamine to treat the Y60 type zeolite, resulting in an enhancement of CO_2 adsorption capacity from 0.4 to 2.45 mmol/g at 60 °C and atmospheric pressure. Chatti *et al.* [35] demonstrated the immobilisation of monoethanolamine on commercial 13X zeolites, showing an improvement of adsorption capacity from 0.848 mmol/g to 1.105 mmol/g at 75 °C and atmospheric pressure.

Although zeolites were reported for their fairly good CO_2 adsorption capacities, their potential for practical applications is limited due to zeolites' sensitivity to water vapour. The presence of water vapour causes the formation of bicarbonates on the surface of zeolites, resulting in strong bonding with CO_2 molecules; hence high temperature for regeneration is needed. Therefore, drying processes are essential for the feed stream before introducing the feed to zeolites-based adsorption beds [1, 16, 36]. Either additional drying of feed stream or high regeneration temperature is required for zeolites beds, leading to an additional operating cost which makes zeolites unfavourable for industrial carbon dioxide capture from wet stream [1, 16, 36]. In addition, the CO_2 adsorption capacity of zeolites also decreases with increasing the adsorption temperature [16, 36]. For example, at 1 bar, the adsorption capacity of zeolite 13X (or NaX) dropped from 4 to 2 mmol/g with the increase of adsorption temperature from 0 to 80 °C, which was associated with the deterioration of adsorbent-adsorbate interactions [16].

2.1.3 Metal organic frameworks (MOFs)

Metal organic frameworks are a special type of hybrid porous materials existing as crystalline lattices with inorganic vertices linked by organic connectors, which result in three-dimensional structures [37, 38]. MOFs have been proposed for different applications, such as gas separation, purification and storage, heterogeneous catalysis and drug delivery due to their appealing properties, such as large internal surface areas (*e.g.* BET of 7140 m^2/g for NU-110E [39]), uniformly structured cavities, high porosity (up to 90% free volume), and low regeneration temperature (*e.g.* 55 °C for Cr-MIL-101 [40]) [25]. In addition, MOFs are also easy to be synthesised and have a high degree of flexibility for the choice

of their organic and inorganic components [25, 38]. Different MOFs have been reported for CO_2 capture, such as MOF-5 [41, 42], MOF-74 [41, 43, 44], MOF-177 [41, 45], CuBTC [46-49], MIL-101 [50] and MIL-102 [51], where CO_2 adsorption capacity are found to depend on various parameters, *i.e*. the specific surface area, pore size, rigidity, sensitivity to impurities that may exist in the feed gas mixture and stability at high temperatures [3].

Similar to the other porous materials that have been investigated for carbon dioxide capture, such as zeolites, application of certain MOFs (such as Zn-based MOFs) are also limited when a significant amount of moisture is present in the feed gas. For example, MOF-177 has an excellent adsorption capacity of 33.5 mmol/g at ambient temperature and 35 bar pressure [47]. But the framework structure of MOF-177 was found to be unstable upon the existence of humidity, which causes the decomposition of MOF-177 after 3 day exposure to ambient air [22]. The low stability of Zn-MOFs in moisturised gas feeds can be attributed to the strong bonding between water molecules and Zn atoms, which is more stable than the bonds between the organic linkers and metal centres. Therefore, when water molecules are present, they attack the Zn centres within Zn-MOFs and gradually displace the organic linkers' connections, leading to the collapse of MOFs' structures [22]. However, there are also other MOFs showing excellent stability against moisture, such as Cr-based MOFs [21, 22].

2.2 *Structure and design of MOFs*

MOFs are three-dimensional hybrid porous materials that compose inorganic metal centres serving as the 'joints' and organic ligands serving as rigid 'struts'. The structural architectures of MOFs depend on how the inorganic and organic components are assembled [2, 52]. The organic linkers are responsible for the flexibility and the diversity of MOF structures as well as their functionalities. MOFs are different from other porous materials as they comprise open scaffolds that have pores without walls [2, 52], as illustrated in Figure 2.1.

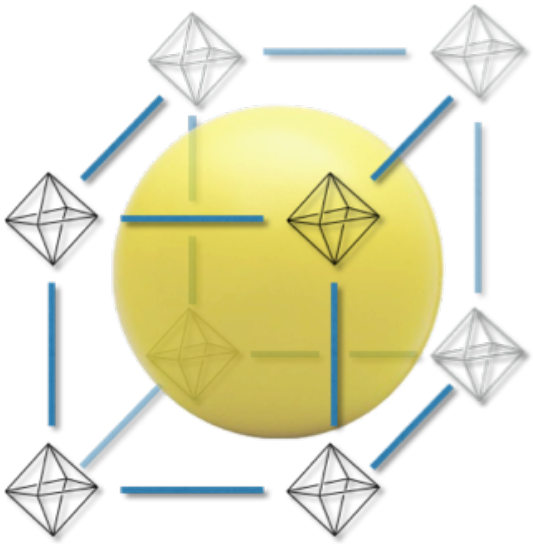

Figure 2.1. The unit cell of MOFs. Black diamonds = inorganic joints; blue rods = organic linkers; the yellow sphere = void space within the framework.

Carboxylate groups of organic linkers are usually used to combine the metal ions and lock them to rigid metal-oxygen-carbon clusters. The point of extension of these clusters is defined by geometrical shapes of the metal clusters knowing as secondary building units (SBUs). The SBUs approach offers a possible avenue towards the design and construction of various MOFs, in which the properties can be designed and symmetrically tuned by a judicious choice of SBUs [37, 52]. On the other hand, the organic ligands are also playing an important role in designing new MOFs. They are not only responsible for enriching the diversity of MOFs, but also for manipulating structures of MOFs, *e.g.* long organic linkers promote bigger void volumes of the resulting MOFs [37, 52, 53].

The adsorption sites on which the gases favour to adsorb are different from one MOF to another. They are either controlled by the metal sites or by the linkers. The role of metal clusters becomes significant when the MOF has open metal sites (unsaturated metal sites) that can attract the gas molecules [54]. On the other hand, when the MOF has saturated metal sites, or the metal sites are inaccessible within the pores, the adsorption of gas molecules will be induced mainly by the polarity of the organic linkers. Some MOFs such as MIL-53 and MIL-88, demonstrate flexible structures that are also explored to manipulate their adsorption properties, *e.g.* their frameworks can expand their pore structures to capture more gas molecules, known as breathing or swelling effect. Such

breathing phenomenon is a reversible transition of unit cell atoms, *i.e.* the change of unit cell volume without changing the unit cell shape [52, 55-57].

Careful attention must be paid to the preparation of MOFs in order to overcome the natural tendency of collapse or deformation of the open networks of materials, which can result in the closing of the accessible pores and channels of MOFs during the exposure to high temperatures [58]. Usually, MOFs are thermally treated (at 120–300 ºC, depending on solvents used in the synthetic method) after the synthesis in order to remove the solvent molecules from frameworks, known as activation [58-60]. Deformation of framework structure may happen during the activation process, for example, the structure of MIL-103 was found to deform and lose its crystallinity when it was heated to 280 ºC [60]. However, other MOFs, such as MOF-5 shows good thermal stability up to a temperature of 400 ºC [41]. The MOFs' thermal stabilities are found to depend on the strength of bonds between metal ions and oxygen molecules that form the inorganic SBUs [61].

2.3 *Synthesis of MOFs*

In general, MOFs can be synthesised directly using metal salts and organic linkers in an appropriate solvent. The organic linkers connect two metal oxide clusters using their donor atoms *e.g.* oxygen, and the bonds between the metal ions and the donor atoms are strong enough to render a quite robust structure [21, 62]. After dissolving both parts in a solvent, the structure of MOFs is formed by self-assembly at temperatures ranging from room temperature to 200 ºC, within hours or days of reaction time [21, 62, 63]. Activation of the resulting MOFs is usually required for the synthesis using solvents as media. The produced MOFs are activated under vacuum and at elevated temperatures in order to remove the guest molecules, *e.g.* solvents [21, 59]. Figure 2.2 illustrates an example of MOF synthesis, *i.e.* from metal-containing nodes and bridging organic ligands to a three-dimensional porous framework.

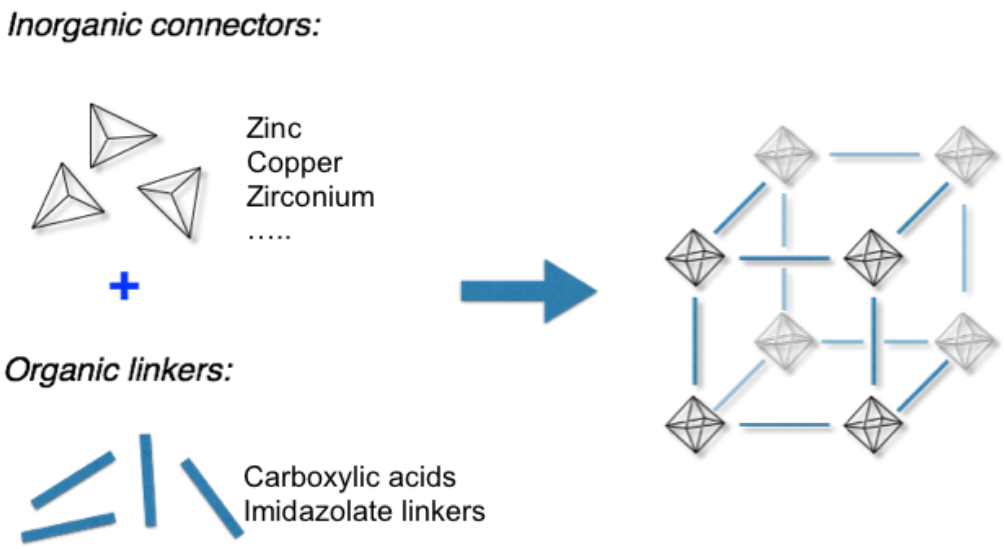

Figure 2.2. Synthesis of MOFs. Black diamonds = inorganic joints; blue rods = organic linkers.

Different methods/strategies have been developed for the synthesis of MOFs. MOFs are commonly prepared by conventional methods of hydrothermal and solvothermal syntheses using electrical heating at laboratory scale with long reaction times from several hours to days [41, 50, 51, 64-67]. However, the increased attention towards using MOFs in practical applications promoted the development of novel synthetic methods with alternative energy and/or facile steps [2, 21]. Recently, new methods for synthesis MOFs have been proposed and investigated, such as microwave assisted [21, 43, 68, 69], ultrasonic assisted [70-72], sonochemical [21, 44, 45, 73], electrochemical [21, 74, 75], mechanochemical [21, 76-78] and ionothermal methods [21, 79]. Though all the aforementioned synthetic methods are being investigated for the synthesis of MOFs, they have advantageous and disadvantages, as summarised Table 2.1 that may limit their specific uses at scale.

Table 2.1
Advantages and disadvantages of common synthetic methods for preparing MOFs.

Methods	Advantages	Disadvantages
Hydrothermal and Solvothermal [41, 50, 51, 64-67]	No hot spots formation	Long reaction time High vapour pressure of the used solvent
Microwave [21, 43, 68, 69]	Short reaction time Low temperature	High vapour pressure of the used solvent Hot spots formation
Ultrasonic [70-72]	Short reaction time Low temperature	High vapour pressure of the used solvent Hot spots formation
Sonochemical [21, 44, 45, 73]	Short reaction time	High vapour pressure of the used solvent Hot spots formation Uncontrollable synthesis temperature
Electrochemical [21, 74, 75]	Short reaction time	Requiring electrolytes in the system (may damage porous structures of MOFs)
Mechanochemical [21, 76-78]	Short reaction time	Difficulty in controlling product properties
Ionothermal [21, 79]	Low solvent vapour pressure	Long reaction time Eutectic phenomena (may lead to problematic handling or damage porous structures of MOFs)

2.4 *Modification of the structure of MOFs*

MOFs are promising materials for carbon dioxide capture due to their high surface areas, large pores' cavities, and high adsorption capacities. But most intriguingly, MOFs offer the possibility of shaping their pores size and tailoring their surface properties by design to enhance the CO_2 adsorption capacity and selectivity. The

functionalisation of MOFs can be achieved by tuning the chemical properties of pore walls through the decoration of relevant functional groups on either the organic ligands [80, 81] or the unsaturated metal centres [82, 83]. Figure 2.3 shows a schematic representation of the modification of MOFs by ligand functionalisation.

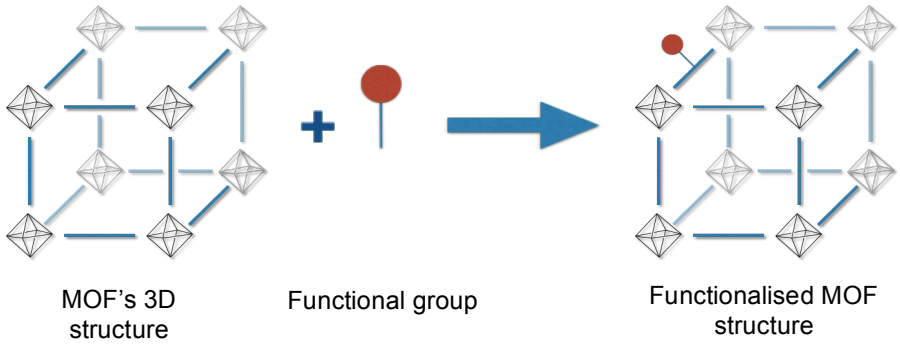

Figure 2.3. Schematic diagram of ligands functionalisation used for modification of MOFs.

Different polar functional groups, such as $–NH_2$, $–CH_3$, –OH, $–OC_3H_7$, –OH and others [80, 83-86], have been identified as being able to boost the CO_2 adsorption capacity and selectivity of MOFs because of the augmented polarity of the MOF structure by the significant quadruple moment of these functional groups [84]. In addition to the modification of surface chemical properties, pores sizes of MOFs can also be adapted by using organic linkers of different lengths, allowing the selective capture of molecules with different molecular sizes.

2.5 *Computational modelling of gas adsorption in porous solids*

2.5.1 Molecular modelling

Molecular modelling is the theoretical and computational techniques used to mimic the behaviour of molecular systems or molecules by constructing their structures in three-dimensional representation [87]. Adsorption simulation via molecular modelling is important since the data collection based on experimental adsorption studies is time/labour consuming. If an adequate and appropriate model of a particular MOF is proposed and validated, then it is convenient to employ the model to perform the screening of this MOF for different applications and to predict

the performance of the MOF under different conditions to reduce the time and capital investment on experimental work [88].

The structures of MOFs are uniform and periodic; therefore, molecular simulation can be an appropriate tool to complement the adsorption experiments facilitating the design of materials and processes. Grand Canonical Monte Carlo (GCMC) method (chemical potential, volume and temperature are kept constant) is widely used for gas adsorption simulation. GCMC method is comparable to the experimental procedures where the gas pressure and system's temperature are set, and gas uptake is measured. Molecular simulations are usually performed using the crystallography information file (CIF) of MOFs to specify the atoms' positions. Hence, a comparison with the experimental results can give insights to the impurities and defects present in the experimental samples. Valuable information, such as the favourable adsorption sites, isosteric heat of adsorption and simulated adsorption isotherms can be provided by molecular simulations.

MCCCS Towhee is an example of Monte Carlo codes used in molecular simulations including gas adsorption simulation, which was developed by M. Martin [89]. In adsorption simulation, Towhee uses Monte Carlo moves to randomly insert, rotate, translate or delete molecules with individually set probabilities. In Towhee, parameters to specify the type of atoms in adsorbate and adsorbent can be provided by various force fields. Interactions between adsorbate-adsorbate and adsorbate-adsorbent molecules can also be set properly to describe the simulated system. Partial charges of the guest molecules and MOFs can be provided to Towhee for better representation of system properties. A large number of Monte Carlo steps needs to be performed for the system to reach equilibrium.

2.5.2 Process modelling

Practical applications of the adsorption for gas separation are commonly carried out in fixed bed columns. Recent studies indicated that pressure swing adsorption (PSA) is a promising choice for CO_2 separation since it is applicable over a wide range of pressure and temperature conditions, as well as has low energy requirements and low capital cost [90].

The design of adsorption process in a fixed bed necessitates the development of an appropriate model to describe the adsorption dynamics using specific adsorbent. Mathematical modelling is a useful tool that can facilitate the optimisation of the adsorption process helping to reduce the time and capital investment for repetitive experiments. Due to the absence of an efficient and universal fixed bed adsorption simulator, the use of relevant experimental data is always required to develop a new process [90]. A predictive and experimentally validated model that uses equilibrium and kinetic parameters, which are independently estimated, can serve the purpose of establishing the column's working capacity. It can also provide the insight into the properties of the adsorbent under adsorption and desorption cycles, estimate the breakthrough curves and temperature profiles of the bed, as well as study the effect of different parameters on the performance of PSA cycle.

The prediction of the column dynamics requires the simultaneous solution of a set of partial differential equations representing mass, energy and momentum balances of the fixed bed column based on appropriate boundary conditions. Since the solution of complex partial differential equations is computationally intensive, assumptions are usually being made to simplify the model providing fairly accurate description of the system with less computational time.

Chapter 3

Improved hydrothermal synthesis and structural characterisation of CuBTC metal organic framework (MOF)

This Chapter contains the content of a published peer-reviewed article in the Chemical Engineering Journal (281 (2015) 669. DOI: 10.1016/j.cej.2015.07.020). This Chapter sheds light on improving the hydrothermal synthesis of CuBTC metal organic framework, as well as characterising the material to assess its structural quality and adsorption properties in comparison to the reported results in the literature. Substantial improvement of the hydrothermal synthesis of CuBTC MOF was achieved with the increase of the synthesis yield to 89.4% (100 ºC, 24 h).

The structural characterisation of the prepared CuBTC MOFs including crystallinity and morphology showed high purity of the prepared samples with no formation of by-products. It also showed good thermal stability of up to *ca.* 280 ºC and large surface area of *ca.* 1507 m^2/g, which are comparable results to the literature data.

Single-component adsorption experiments (CO_2 and N_2) were investigated in the range of (0–20) bar at 25 and 50 ºC, in which the conditions relevant to flue gases emissions (50 ºC, 1 bar, 15% CO_2 composition) were used to evaluate the performance of CuBTC MOF. The adsorption experimental results showed that CuBTC MOF has an uptake of CO_2 (*ca.* 2.39 mmol/g) higher than that of N_2 (*ca*. 0.03 mmol/g) at 1 bar total pressure and 15 % CO_2 composition. These results were also used to calculate the Ideal Adsorption Solution Theory (IAST) selectivity that showed high selectivity of CO_2/N_2 of 16 at a CO_2 partial pressure of 0.15 bar, suggesting that CuBTC MOF can be a good candidate for CO_2 adsorption from a CO_2/N_2 mixture.

3.1 *Introduction*

Global warming is still a major threat to human society limiting its sustainable development by a complex range of factors. Infant mortality is closely linked to undernutrition and food insecurity, both affected by climate change induced by the global warming [7].

Flue gases from power plants and industrial furnaces are major sources of CO_2 emissions to the atmosphere. Emitted at 50–75 ºC and 0–1 bar [1], flue gases contain large amount of CO_2, as much as 5–15 vol.%, together with other gases such as nitrogen (70–75 vol.%) and water vapour of (5–7 vol.%), depending on the fuel being used [1, 2]. However, the target concentration of CO_2 in the exhaust clean gas to be released into the atmosphere is only 0.03 vol.% [32, 91].

Various porous adsorbents have been investigated for CO_2 adsorption, including carbonaceous material, zeolites and metal organic frameworks (MOFs) [2, 16, 92]. MOFs represent one of the major classes of crystalline porous materials that have shown a potential for CO_2 capture due to their remarkably large surface areas, ease of synthesis and tunable structural/chemical properties [38, 40]. The suitability of MOFs for carbon capture was mainly evaluated at the laboratory scale using gravimetric methods. The application of MOFs in different industrial settings depends on several factors including the CO_2 adsorption capacity, selectivity, thermal and hydrothermal stabilities, operation windows (*e.g.* temperature and pressure), availability and cost. Therefore, trade-offs among these factors need to be considered for the materials' selection and capture system's design.

CuBTC framework (BTC = benzene-1,3,5-tricarboxylate) [19], is well-known MOF for its good CO_2 adsorption capacity (5 mmol/g at 1 bar and 25 ºC [93]). CuBTC MOF has been successfully prepared using various synthetic methods, including the conventional hydrothermal/solvothermal methods [19, 21, 64, 65, 94], alternative synthetic methods based on unconventional energy sources (*i.e.* microwave [21, 69] and ultrasound [21, 71]), mechanochemical procedure [21, 78] and electrochemical procedure [21, 75]. Although alternative synthetic methods offer quantitative yields of CuBTC MOF at the laboratory scale with relatively short reaction times, they usually result in products of inconsistent yields, porous

structures and crystallinity. For example, a microwave-assisted solvothermal synthesis has been developed as the fastest method to produce pure CuBTC MOF (10–30 min synthesis time [69, 94]). However, the yields and qualities of the resulting product and the optimum reaction conditions are found to significantly depend on the choice of the microwave system [69, 94]. Considering the possible hot spot formation in the system using alternative energy for intensive heating, the scalability of such processes to produce consistent, high-quality materials is limited. Therefore, the conventional hydrothermal methods are still attractive for the large-scale manufacturing of CuBTC MOFs, though the balance between the reaction conditions (temperature and synthesis time) and the by-product (*e.g.* Cu_2O) formation is still a challenge.

In this Chapter, CuBTC framework was used as the model MOF, presenting (*i*) an improved synthesis of CuBTC MOF using static hydrothermal methods to enable their production at scale and (*ii*) the experimental investigation of gas adsorption on CuBTC MOF under conditions close to real flue gas streams.

3.2 *Experimental*

3.2.1 Materials

Copper (II) nitrate trihydrate [$Cu(NO_3)_2 \cdot 3H_2O$, 99%] and benzene-1,3,5 tricarboxylic acid (BTC, 95%) were obtained from Sigma Aldrich and ethanol (absolute, EtOH) was purchased from Fisher. All materials were used as received without further purification.

3.2.2 Hydrothermal synthesis of CuBTC MOF

The general procedure of preparing CuBTC MOF using hydrothermal synthesis was based on the method reported by Chui *et al.* [19] and Schlichte *et al.* [65] where BTC (0.42 g, 2 mmol) was dissolved in 24 cm^3 of 50:50 vol.% mixture of ethanol and deionised water. The mixture was stirred for 10 min until a clear solution was obtained. $Cu(NO_3)_2 \cdot 3H_2O$ (0.875 g, 3.62 mmol) was then added to the mixture and stirred thoroughly for another 10 min. Once the reactants were completely dissolved in the solvent, the resultant blue solution was transferred to a 50 cm^3 teflon-lined stainless steel autoclave, heated at 100 ºC for the

crystallisation to occur. After synthesis, the reactor was cooled down to room temperature and a blue crystalline powder was formed. The powder was then filtered and washed thoroughly with 60 cm^3 mixture of water and ethanol (% v/v of water = 50%). The powder was finally activated under vacuum at 120 ºC for 16 h and then stored in vials at 80 ºC for further experiments.

3.2.3 Characterisation methods of CuBTC framework

Powder X-ray diffraction (PXRD) data of CuBTC MOF samples were collected on a Rigaku Miniflex diffractometer (Cu*Kα* radiation, 30 kV, 15 mA, λ = 1.5406 Å). The used radiation was in the range of 5º < 2θ < 46º to cover the essential section of PXRD patterns of the studied samples for structure determination. The scan speed used was 3 º/min with a step size of 0.02.

Scanning electron microscopy (SEM) analyses of CuBTC MOF samples were carried out using FEI Quanta 200 ESEM equipment with a high voltage mode of 20 kV. All samples were coated with gold prior to the SEM imaging in order to create a conductive layer on materials to inhibit their surfaces charging. The gold coating was performed using the Emitech K550X sputter coater under vacuum conditions of 1×10^{-4} mbar.

Nitrogen adsorption/desorption isotherms of CuBTC MOF samples at −196 ºC were obtained using a Micrometrics Accelerated Surface Area and Porosimetry (ASAP) 2020 analyser. Prior to the isotherms' measurement, samples were degassed at 200 ºC under vacuum for 8 h. Equilibration time of 45 s was specified for each data point of isotherms during the analysis. Brunauer–Emmett–Teller (BET) method [95] was applied to determine the specific surface areas (SSAs) of materials. Details of BET calculations can be found in Appendix A.1.

Thermogravimetric analysis (TGA) was carried out with a TA Q5000 (V3.15 Build 263) thermogravimetric analyser. The temperature range was (room temperature – 450 ºC) with a heating rate of 5 ºC/min in a nitrogen atmosphere (25 cm^3/min).

Differential scanning calorimetric (DSC) analysis was carried out using Mettler DSC30 instrument, with explorer software to perform the peak analyses. The samples were dispensed into aluminium sample pans and hermetically sealed to

prevent sample losses. The sample pan (with its lid) was weighed before and after sealing to determine the exact weight of the sample. The reference chambers contained an empty pan with its lid. The accuracy of the enthalpy measurements is ±1%. Samples were heated at a rate of 5 ºC/min and the scan was completed over a range of 50 ºC to 350 ºC.

3.2.4 Single-component adsorption equilibrium of CO_2 and N_2 on CuBTC MOF

Pure CO_2 and N_2 adsorption/desorption experiments on synthesised CuBTC MOF were carried out using the intelligent gravimetric analyser (Hiden Analytical, IGA-001). Samples were thermally degassed at 100 ºC for 3 h then heated up to 200 ºC (heating rate = 2 ºC/min) and kept at 200 ºC for 8 h under vacuum. Buoyancy effects were assessed to determine the density of materials with helium adsorption at 20 ºC prior to CO_2 and N_2 adsorption measurements. The measured density was then used for CO_2 and N_2 adsorption/desorption isotherms acquisition at 20 ºC and 50 ºC from 0 to 20 bar. At each pressure point, the system was left to equilibrate for a minimum of 35 min and maximum of 2 h. The samples' masses that have been used were in the range of 70–80 mg.

Langmuir theory was employed to study the collected adsorption data in this study [96, 97]. Langmuir model assumes a monolayer adsorption where the interaction between the first adsorbed gas layer and the solid surface is significantly stronger than the one between gas layers, yielding a negligible number of molecules in the second gas layer.

The Langmuir model for the solid-gas system is commonly expressed as Eq 3.1.

$$\theta = \frac{kP}{1 + kP} \tag{3.1}$$

where k is the Langmuir constant in (bar^{-1}), θ is the fraction of the adsorbed gas molecules over the maximum adsorption capacity at equilibrium, and P is the pressure (bar).

Eq 3.1 suggests that, at low pressure, the quantity of adsorbed gas is linearly proportional to the pressure, while the amount of adsorbed gas will increase slowly

till full saturation of gas molecules on solid surface with the rise in pressure [96, 97].

The fraction of adsorbed amount θ is equal to N/c, where N is the equilibrium number of adsorbed gas molecules and c is the saturation capacity (the maximum number of gas molecules required to form a monolayer). Accordingly, Eq 3.1 can be rewritten as Eq 3.2:

$$\frac{N}{c} = \frac{kP}{1+kP} \tag{3.2}$$

3.3 *Results and discussion*

3.3.1 Improving the hydrothermal synthesis of CuBTC framework

The hydrothermal synthesis of CuBTC MOF has been optimised based on the original recipe developed by Chui *et al.* [19] and Schlichte *et al.* [65], *i.e.* starting with $Cu(NO_3)_2 \cdot 3H_2O$ salt and BTC as reactants and H_2O and EtOH mixture as the reaction media. The original work was carried out at 180 ºC for 12 h to obtain CuBTC MOF and the yield achieved was *ca.* 60% [19] due to the formation of Cu_2O as the by-product at 180 ºC [19, 64].

Over the past decade, effort has been made by varying the synthesis temperature and time to improve the quality and yield of CuBTC MOF from hydrothermal synthesis, as summarised in Table 3.1. In general, it was found that low synthesis temperatures tend to suppress the formation of Cu_2O promoting the formation of CuBTC MOF with high purity [64]. However, long reaction times are usually required to achieve the high yields. Well-shaped pure octahedral crystals of CuBTC MOF (evidenced by the SEM analysis) were obtained at 75 ºC with a maximum yield of 84% after a prolonged reaction time of 320 h [64]. Most of the previous studies focused on the comparison of resulting products in terms of BET surface area and pore volume for the potential gas adsorption and storage applications. However, only a few studies have investigated the effect of the variation of synthesis conditions on the yield of CuBTC MOF [64, 94]. In order to gain a fundamental understanding of the effect of the synthesis conditions of CuBTC MOF on its yield, a systematic study was carried out.

Table 3.1

Selected studies of reaction conditions and yields for the hydrothermal synthesis of CuBTC MOF.

Year published	Synthesis temperature (°C)	Synthesis time (h)	Solvents	Yield (%)	BET surface area (m^2/g)	P/P^0 range used in BET analysis	Ref.
1999	180	12	H_2O + EtOH	*ca.* 60	692.2	N/A	[19]
2002	110	18	H_2O + EtOH	*ca.* 74*	964.5	N/A	[98]
2004	120	12	H_2O + EtOH	*ca.* 60	N/A	N/A	[65]
2006	110	15	H_2O + EtOH	N/A	N/A	N/A	[99]
2007	85	8	H_2O + EtOH + DMF	N/A	1482	0.1–0.3	[100]
			EtOH + DMF + CH_2Cl_2	N/A	698		
2008	120	14	H_2O + EtOH	N/A	1510	N/A	[74]
			EtOH	N/A	1253		
2008	Room temperature	23	H_2O + EtOH + DMF	44	N/A	N/A	[41]
			+ Triethylamine				
2008	95	15	H_2O + EtOH	N/A	N/A	N/A	[101]
2009	75	320	H_2O + EtOH	*ca.* 80	N/A	N/A	[64]
2010	120	24	H_2O + EtOH	*ca.* 94*	1143	0.05–0.33	[94]
			DMF	N/A	1323		
2012	110	18	H_2O + EtOH	N/A	1055	N/A	[102]

***CuBTC MOF yield was calculated based on substrate *i.e.* $Cu(NO_3)_2$.**

The yield of CuBTC MOF at 100 ºC (calculated using Eq 3.3, based on the limiting reactant) increased with increasing the reaction time until it reaches a maximum value of 89.4% at 24 h (Figure 3.1), details of the yield calculation are given in Appendix A.2. Further increase of the reaction time beyond 24 h resulted in a decrease in the yield, which is in agreement with the observations by Seo *et al.* [69]. Prolonged contact time between the formed crystals and the synthesis medium can lead to the re-dissolution of CuBTC MOF due to the shift of equilibrium between the crystallised and dissolved material. Reproducibility was confirmed by repeating each experiment twice with an error in produced masses of less than 3%.

$$\text{Yield of CuBTC MOF (\%)} = \frac{\text{mass of activated CuBTC MOF sample}}{\text{theoretical mass based on the limiting reactant}} \times 100\% \qquad (3.3)$$

In addition, the as-made sample obtained at 100 ºC (before activation under vacuum) has a blue colour, while the colour of the activated framework is dark violet, Figure 3.1. The colour change of CuBTC framework before and after activation is caused by the removal of the covalently bonded water molecules from copper centres [65], and the associated *d-d* transition of copper ions [102].

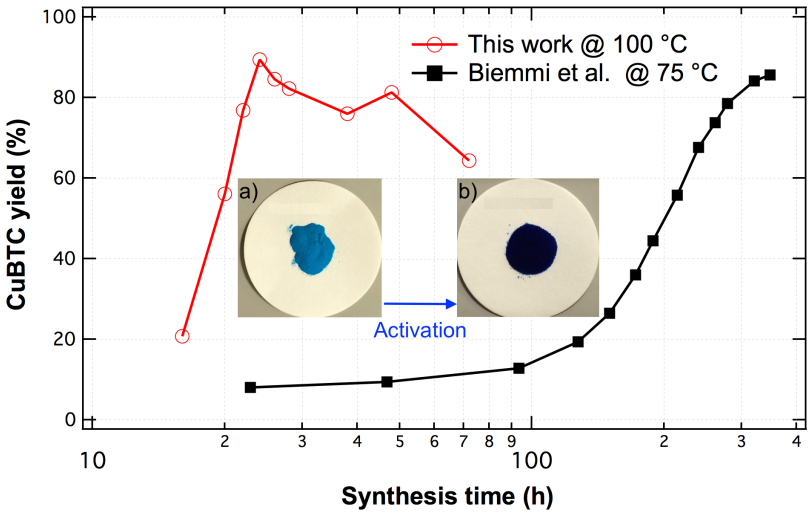

Figure 3.1. Yields of CuBTC MOF at different synthesis temperatures as a function of reaction time compared to Biemmi *et al.* [64] reported yield. Inset: CuBTC MOF synthesised at 100 °C under static hydrothermal conditions for: (a) as-made sample and (b) activated sample.

3.3.2 Characterisation of CuBTC MOFs

The crystallinity of the synthesised samples as a function of reaction time at 100 °C was investigated using PXRD analysis as shown in Figure 3.2. CuBTC MOF is one of the most frequently investigated MOFs and its crystalline phase, which is usually exemplified by a PXRD pattern with characteristic peaks at 2θ ≈ 6.5º, 9.5º, 11.5º and 13.4º [19, 64, 65, 69, 102]. A commercial sample of CuBTC MOF (Appendix A.3) has been analysed and is in a good agreement with this work, confirming the formation of CuBTC MOF crystalline phase. The variations in intensities of the different diffraction peaks can be attributed to the degree of hydration of different samples since CuBTC MOF crystals can rapidly adsorb

moisture from the air [65, 102]. The characteristic diffraction peaks of Cu_2O are reported as the main peaks at 2θ ≈ 36.4º, 42.3º and 43.3º [64] are not observed in the PXRD patterns of CuBTC frameworks synthesised at 100 °C under static hydrothermal conditions suggesting high purity of CuBTC MOF product.

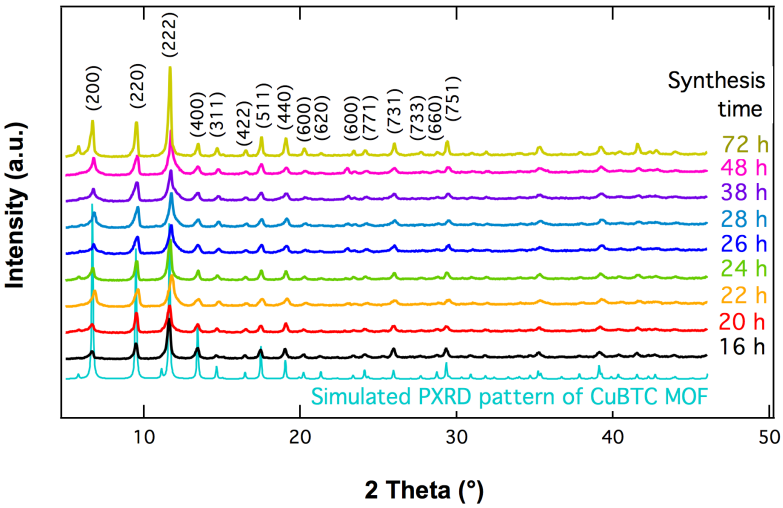

Figure 3.2. PXRD patterns of CuBTC frameworks synthesised with different reaction times under hydrothermal conditions at 100 ºC. Simulated pattern has been adapted from Chui *et al.* [19].

The effect of synthesis time on the morphology of CuBTC MOF crystals at 100 °C was studied using SEM characterisation. Representative images are shown in Figure 3.3. For samples synthesised with reaction time < 24 h, clean crystals with average sizes of *ca.* 20 µm were obtained as shown in Figure 3.3a and b**.** These crystals are well-defined octahedrons with sharp edges, and such findings are consistent with the typical octahedral shape of CuBTC MOF crystal previously reported [64, 83, 102].

The octahedral morphology of CuBTC MOF crystals becomes less defined for a reaction time of 28 h, *i.e.* losing the sharp edges while maintaining the crystal's size as *ca.* 20 µm, as seen in Figure 3.3c. Further increase of the reaction time to 38 h and above leads to the deformation of CuBTC MOF crystals with a shrinking of crystals' sizes and losing the octahedral shapes completely, Figure 3.3d. The change of CuBTC MOF morphology as the synthesis time increases is directly related to the decrease in yield, indicating the re-dissolution of CuBTC MOF crystals in the reaction media caused by the prolonged reaction time. Similar

observations were reported in the hydrothermal synthesis of ceramic materials [103, 104].

In addition, Figure 3.3d also reveals that prolonged synthesis time resulted in the formation of small particles/crystals on the surface of CuBTC framework octahedrons. These small particles are possibly the re-crystallised CuBTC MOF phase or the by-product formed with long reaction time at 100 ºC. Further investigation is needed to understand the equilibrium dynamics between the crystallised MOFs and the MOFs that remain in the solution for optimising the synthesis of MOFs under hydrothermal conditions.

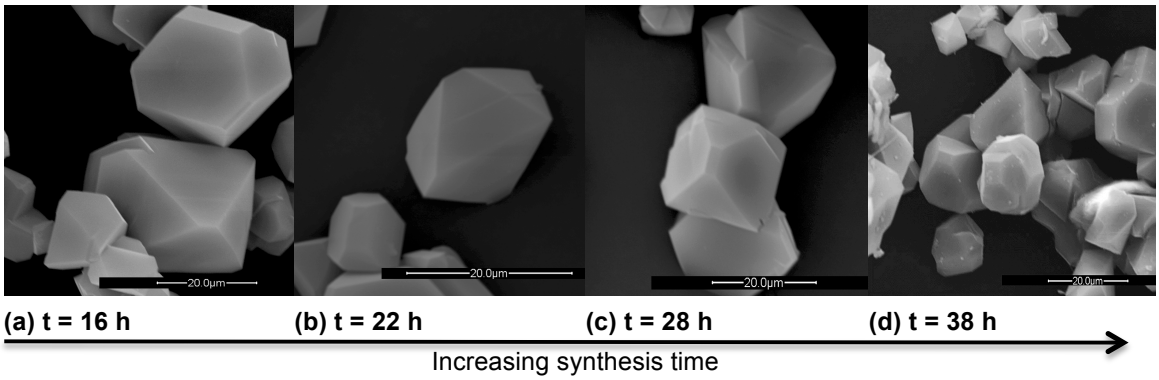

Figure 3.3. The influence of the synthesis time at 100 ºC on the morphology of CuBTC MOF. SEM images of synthesised CuBTC samples at reaction times of (a) 16 h, (b) 22 h, (c) 28 h and (d) 38 h.

Nitrogen adsorption and desorption isotherms of the sample that was synthesised at 100 ºC and 24 h were measured. The BET specific surface areas and pore volume were calculated as 1507±26 m^2/g and 0.609 cm^2/g, respectively, comparable to the previously reported values (Table 3.1 and refs [105, 106]). Variations in the measured BET surface areas and the pore volume from different investigations may be attributed to the difference in post-synthesis work-up procedures, *i.e.* washing and activation of CuBTC MOF samples.

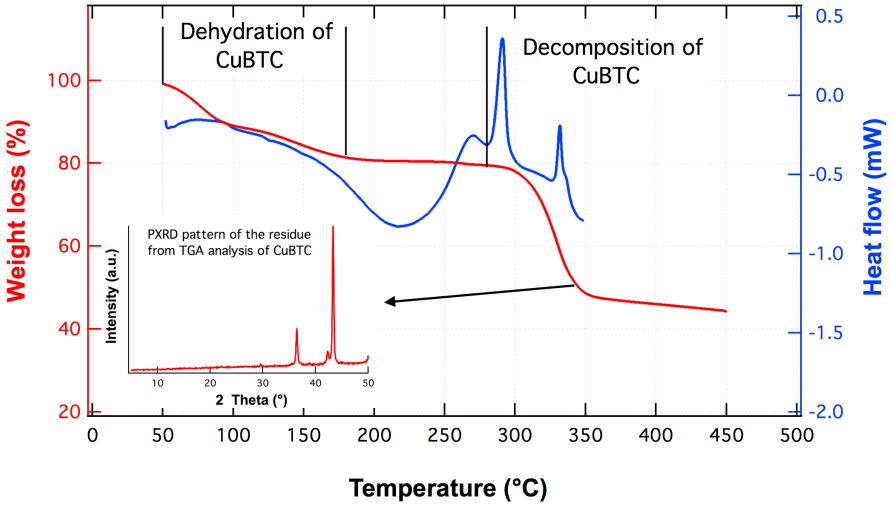

Figure 3.4. TGA and DSC analyses of CuBTC MOF synthesised at 100 ºC and 24 h (after activation). Inset: PXRD pattern of the residual material after the TGA analysis.

TGA thermogram (Figure 3.4) shows the thermal stability of CuBTC framework synthesised in this work at 100 ºC and 24 h. Dehydration of the material takes place up to *ca.* 180 ºC with total weight loss of *ca.* 20 wt.%, corresponding to three water molecules per Cu centre in the framework (fully hydrated CuBTC MOF is reported to hold up to 40 wt.% water [98]).

DSC result correlates well to the TGA showing an endothermic peak at 100–280 ºC, due to the dehydration of CuBTC MOF. CuBTC MOF was found to be thermally stable up to 280 ºC before starting to disintegrate gradually at higher temperatures [69, 98]. The weight loss of decomposition was measured as 36%, which is very close to the theoretical loss of 36.7% accounting for decomposition into Cu_2O and CuO [69] (PXRD analysis of the residue after TGA is shown in the inset of Figure 3.4). Two exothermic peaks were discovered by DCS analysis after 280 ºC, where the first exothermic peak (280–300 ºC) corresponds to the formation of Cu_2O [107] and the second one corresponds to the phase transformation of Cu_2O to CuO [63].

3.3.3 CO_2 and N_2 adsorption on to CuBTC MOF

The experimental adsorption isotherms of CO_2 and N_2 on to CuBTC MOF were measured over a pressure range of 0–20 bar at 25 and 50 ºC, as shown in Figure 3.5a. No hysteresis loops were detected between the adsorption and desorption isotherms suggesting no tensile strength effect caused by ink-bottle type pores. In

addition, these results showed that the adsorption of CO_2 and N_2 on CuBTC MOF is completely reversible upon the studied pressures and temperatures, two cycles of CO_2 adsorption on CuBTC MOF are presented in Appendix A.4. The adsorption capacity on CuBTC MOF decreases with the increase in temperature for both gases. CuBTC MOF has a higher affinity to CO_2 than to N_2, evidenced by the significant difference in adsorption capacities at any studied pressure. Figure 3.5a also presents the correlation of the CO_2 and N_2 isotherms with the Langmuir model, with a squared residual (R^2) larger than 0.9995.

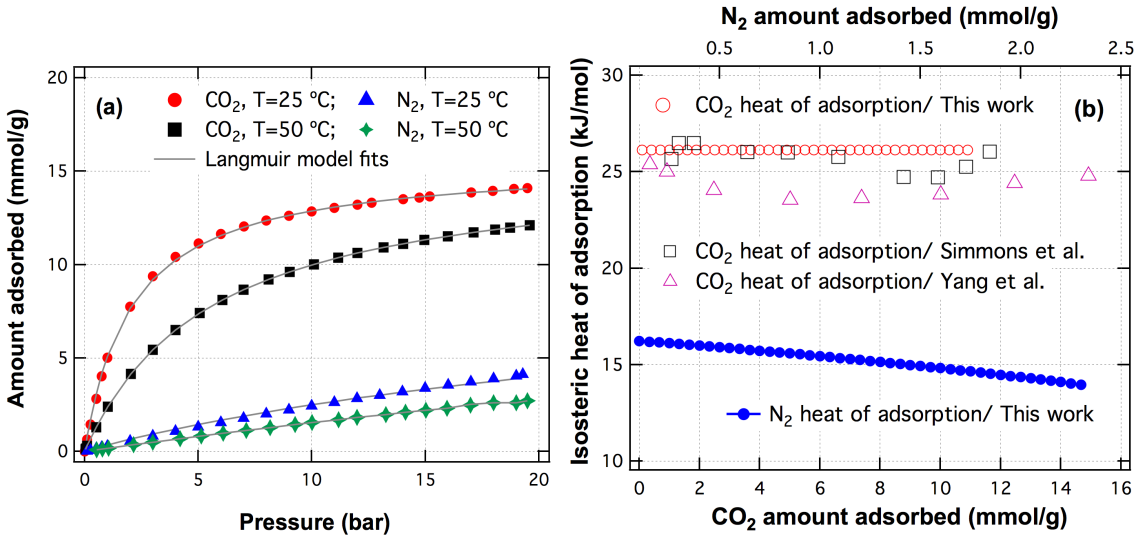

Figure 3.5. (a) Single-component CO_2 and N_2 adsorption isotherms for CuBTC MOF measured at 25 ºC and 50 ºC over a pressure range of 0–20 bar, (b) Calculated isosteric heat of adsorption as a function of uptake for CO_2 and N_2 onto CuBTC MOF compared to Simmons *et al.* [106] and Yang *et al.* [108].

Considering the application of CuBTC MOF as potential materials for CO_2 adsorption from flue gases, only the data from the pressure range of (0–1 bar) at 50 ºC and 15% CO_2 composition is of interest. Here, the selectivity of CO_2 to N_2 (under conditions of 50 ºC, 1 bar total pressure and 15 % CO_2 composition) calculated with the Ideal Adsorption Solution Theory (IAST) method [109, 110] was found as *ca.* 16.

Obtained constants of Langmuir model were also used to calculate the isosteric heat of adsorption for CO_2 and N_2 gases using Eq 3.4, as shown in Figure 3.5b, which are in good agreement with previously reported data [106, 108].

$$\left(\frac{d\ln P}{dT}\right)_n = \frac{q^{st}}{RT^2} \tag{3.4}$$

where q^{st} is the isosteric heat of adsorption, n is the amount adsorbed at a pressure P and temperature T and R is the ideal gas constant.

The calculated isosteric heat of CO_2 and N_2 adsorption is found to be almost constant over the range of adsorbate loading, indicating an energetically homogeneous surface of the adsorbent (CuBTC MOF), *i.e.* all the available adsorption sites have the same adsorption energy for the probing gases [111, 112]. The obtained values of isosteric heat for CO_2 and N_2 adsorption onto CuBTC framework are *ca.* 27 kJ/mol and *ca.* 14.5 kJ/mol, respectively, which are in the typical range of physisorption.

3.4 *Conclusions*

Hydrothermal synthesis of CuBTC MOF has been extensively investigated in the last decade. This Chapter demonstrated the optimisation of its hydrothermal synthesis process leading to a high quantitative yield of 89.4% in the synthesis at 100 ºC over 24 h. This work provides a good understanding of the effect of the synthetic hydrothermal parameters of temperature and time on the quality and yield of CuBTC MOF.

Prepared samples in this work were characterised to assess their crystallinity and morphology, thermal stability and surface area. The synthesised samples showed high purity based on the PXRD analysis (where no peaks intensities related to the formation of by-products, CuO or Cu_2O were observed) and SEM images (which showed clean crystals).

Additionally, single-component adsorption experiments were conducted at 50 ºC and 0–20 bar which showed reversible adsorption of CO_2 and N_2 on CuBTC MOF over this pressure range. Evaluation of the performance of CuBTC MOF under conditions relevant to flue gas emission (*i.e.* 50 ºC, 0–1 bar) suggested that CuBTC MOF have higher affinity to CO_2 than N_2 at total pressure of 1 bar and 15% CO_2 composition (uptake is *ca.* 2.39 mmol/g for CO_2 and *ca.* 0.03 mmol/g for N_2, respectively) as well as high IAST selectivity of CO_2/N_2 of *ca.* 16.

The above results showed that CuBTC MOF can be a promising candidate for CO_2 capture, whereas further investigation of the effect of flue gas impurities such as water vapour is required.

Chapter 4

Understanding the hydrothermal stability of CuBTC MOF under humid conditions

This Chapter contains the content of published peer-reviewed articles in the Chemical Engineering Journal (281 (2015) 669. DOI: 10.1016/j.cej.2015.07.020) and Frontiers of Chemical Science and Engineering (10 (2016) 103. DOI: 10.1016/j.cej.2015.07.020) as well as unpublished work.

This Chapter presents a comprehensive analysis of the stability of CuBTC MOF under dynamic humid conditions. The vapour adsorption experiments were carried out in a temperature range of 25–50 ºC and relative humidity range of 0–90% at atmospheric pressure. Dynamics of material deformation of the porous structure of CuBTC MOF was captured, and associated decomposition mechanism was revealed based on various characterisation techniques. The results showed that the aggregation of water molecules near copper centres under humid conditions could displace the coordination of copper centres and carboxylic ligands leading to the collapse of the framework of CuBTC MOF.

The hydration process of CuBTC MOF was also investigated using cyclic dynamic vapour adsorption experiments in the range of natural gas and flue gas emissions conditions. It was found that the hydration of CuBTC MOF is affected by the temperature, vapour partial pressure and degassing conditions (pre-treatment). CuBTC MOF showed reasonable stability under natural gas emission conditions. However, it could not survive under flue gas emission conditions.

This Chapter provides a good understanding of the performance of CuBTC MOF, as well as an insight into the decomposition mechanism of CuBTC under humid conditions. Based on the decomposition mechanism, methods of modifying the material to enhance its hydrothermal stability can be devised.

4.1 *Introduction*

Metal-organic frameworks (MOFs) have been demonstrated as promising materials for addressing key societal challenges, such as climate change and renewable energy [38, 113]. For example, CuBTC MOF has been identified as a potential candidate for energy storage [102] and CO_2 capture [11]. Considering the promising applications of MOFs as storage media and adsorbents for gas adsorption and separation, the hydrothermal stability of MOFs is a paramount issue to be addressed. Hydrothermally unstable adsorbents at process conditions or during regeneration, where water vapour may exist, *e.g.* < 7 vol.% water vapour (*ca.* 60% relative humidity, RH) in flue gases at 50 °C, can limit their usefulness significantly [114]. Therefore, understanding the stability of MOFs under humid conditions for CO_2 capture is necessary.

CuBTC MOF is one of the MOFs that has been widely investigated by the community since it was first reported at the end of the 20th century [19]. A recent development showed that the synthesis of CuBTC MOF could be enabled by a continuous mechanochemical technique (based on the screw extruder) [115]. The major advantage of this method is the great reduction in solvent usage which enabled the commercial availability of CuBTC MOF with a relatively competitive price. Comparing to the improved hydrothermal method for CuBTC MOF synthesis reported in Chapter 3, the mechanochemical synthesis could produce CuBTC MOF with a significant rate of 1 kg per hour with merely 0.25% solvent consumption (solvent usage in the improved hydrothermal method was calculated based on synthesising 1 kg of CuBTC MOF in the laboratory). Furthermore, the mechanochemical method based on the screw extruder was also estimated to reduce the energy input by up to 50% in comparison to the lengthy synthesis of the hydrothermal method. Therefore, CuBTC MOF can potentially be manufactured at a large scale with reasonable cost for applications' practical settings.

It was shown in the literature that CuBTC MOF is a good candidate for CO_2 adsorption under various operating conditions [47, 93, 98, 105, 106, 116-118]. The only concern is its hydrophilic nature that enhances the water vapour adsorption under humid conditions, leading to serious stability issues. Although it was proved

that a low water vapour content of 4 wt.% in CuBTC MOF could enhance the CO_2 adsorption capacity (*ca.* 11.36 mmol/g of dry structure compared to *ca.* 15.45 mmol/g of 4 wt.% hydrated structure at 25 ºC and 5 bar) [49], the use of CuBTC MOF for CO_2 capture at conditions with high water vapour partial pressure is still questionable. The hydrothermal stability of CuBTC MOF has been extensively studied in the literature with contradictory conclusions as summarised in Table 4.1. Some reports claimed that the structure of CuBTC was stable with reversible water vapour adsorption. Others suggested the partial degradation of CuBTC MOF based on various characterisation methods, *e.g. (i)* loss of the characteristic diffraction peaks by powder X-ray diffraction (PXRD) analysis, *(ii)* loss of BET surface area, *(iii)* variation in the morphology, and *(iv)* the regression in the CO_2 uptake of the spent CuBTC MOF samples from water vapour adsorption or hydration experiments. On the other hand, numerical and modelling studies were also carried out to understand the interaction of water vapour and CuBTC MOF using either classical or quantum mechanical simulations [119].

In this Chapter, the hydrothermal stability envelope of CuBTC MOF using dynamic vapour adsorption experiments was mapped providing a guidance of using CuBTC MOF in presence of humidity. In addition, detailed characterisation of the spent CuBTC MOF samples from dynamic water vapour adsorption experiments using PXRD, scanning electron microscopy (SEM), small angle X-ray spectroscopy (SAXS), Fourier transform infrared (FTIR) and differential scanning calorimetric analysis (DSC) was carried out, which provided insight into the decomposition mechanism of CuBTC MOF under dynamic humid streams. Furthermore, the ability of CuBTC MOF to withstand cyclic humid flows under natural gas and flue gas emissions conditions was investigated in order to determine the performance of CuBTC MOF under various dynamic circumstances including short exposure times and different degassing routines.

Table 4.1

Selected studies of water adsorption/hydrothermal stability of CuBTC MOF.

Year and Ref.	Water conditions	Tempera-ture (ºC)	Exposure time per point	Characterisation methods of the used samples	Observations
2008 [120]	Water vapour, *P/Pº* = 0–0.68 *P/Pº* = 0.4	25	– 7 days	PXRD and BET analysis	The structure is stable for all the studied P/Pº range with no differences in the PXRD patterns or surface area of used and fresh samples
2008 [121]	Water vapour, *P* = 0–2.7 mbar	22	–	GCMC and MC simulations using NVT ensemble to calculate pure adsorption isotherms, Henry's coefficient, free energy, entropies, and enthalpies of water vapour adsorption	
2009 [122]	Liquid water Water vapour, *P/Pº* = 0–0.98	50 25	24 h 60 s	PXRD and BET analysis	Irreversible structure's change. *ca.* 52% of surface area reduction of used sample compared to the fresh sample
2009 [49]	4 and 8% hydrated sample	25	–	CO_2 sorption of dry and hydrated samples.	The 4% hydrated sample showed 71% increase in CO_2 adsorption at 0.1 bar pressure, while the 8% adsorbed less than the dry sample
2009 [116]	Water vapour, *P/Pº* = 0–0.97	25 32	2–8 h	PXRD and pure CO_2 adsorption	The used samples exhibited different PXRD patterns suggesting structure's degradation. 75% decline in pure CO_2 adsorption capacity after three water vapour adsorption cycles
2009 [114]	50 mol% of Steam/N_2	85, 200, and 300	2 h	PXRD, SEM and QM calculations	CuBTC MOF collapsed at 300 ºC. The ligand displacement was suggested as the degradation reason based on the bonds strength calculations
2010 [123]	Water vapour, *P/Pº* = 0–0.99	25	–	CO_2, CO_2/H_2O sorption after the pure H_2O sorption*	CO_2 adsorption capacity is prone to CuBTC MOF degradation with *ca.* 7% decrease after 5 runs of water vapour adsorption measurements
2010 [124]	1:1–1:7 water/DMF Vapour *P/Pº* = 0.18, and liquid	25	1 h 24 h	PXRD	The structure is stable for all the studied water/DMF ratios, water vapour with *P/Pº* = 0.18 for 24 h, and liquid water for 5 h. New PXRD peaks were observed after 24 h in liquid water
2011 [125]	0.5–5 mole equivalent to one copper site	Ambient conditions	6–60 days	^{1}H and ^{13}C solid state NMR	CuBTC MOF is stable at 0.5 mole equivalent during 60 days. Different pathways of decomposition were noticed, without showing the possible mechanism
2012 [126]	Water vapour, *P/Pº* = 0–0.95	25	–	CO_2 adsorption-desorption with 0.03–0.4 *P/Pº*. PXRD, BET and 6 sorption cycles were reported	90%, 20%, and 60% reversibility for *P/Pº* = 0.03, 0.1–0.2, and 0.4 due to the adsorption in low quantity, pore surface, centre of pores, respectively The BET decreased by 14% when was kept free of moisture, 71% and 78% upon exposure to ambient air and 70% RH% for 80 h, respectively. Slight change in the PXRD patterns was observed
2012 [127]	20–120 mbar	20–52	–	Pure water vapour adsorption studies and adsorption cooling cycles	

2012 [128]	Water vapour, P/P^o = 0–0.9	25	24 h max	PXRD and BET analysis	The used samples retained their crystallinities based on PXRD results with a partial degradation due to the change in peak intensities. *ca.* 26% of BET loss after pure water vapour adsorption was observed.
2013 [129]	Atmospheric water	Ambient conditions	3 min–80 h	^{1}H solid NMR and average chemical shift calculations	Each two Cu pairs in the paddle wheel are firstly occupied by one H_2O molecule, and later, a second H_2O molecule is added. Then, a shift and exchange in the adsorb water molecules was found
2013 [130]	0.25–4 mole equivalents to one copper site	28–292	200 ps	ReaxFF molecular simulation	CuBTC MOF is stable up to a temperature of 125 °C, and the structure collapsed at 277 °C. The reactive adsorption of NH_3 and NH_3/H_2O mixture on hydrated CuBTC MOF was also studied
2013 [131]	2 water molecules	-	–	DFT and MP2 approaches were used to describe the water-CuBTC MOF interactions. Simultaneous adsorption on the OMS cluster $Cu_2(HCOO)_4$ was used throughout the study	
2013 [132]	Water vapour, P/P^o = 0–0.63	25	–	New force field describing the water vapour adsorption on CuBTC MOF was developed, using the dispersion-corrected DFT calculations with classical atomistic simulations. The results' transferability was tested using two other analogous MOFs; CuMBTC and CuEBTC, where both agreed fairly with the experimental results	
2013 [133]	Water vapour, P/P^o = 0–0.9 90% RH 40% RH 90% RH	25, and 40 25 40 40	— 0, 1, 3, 7, 14, and 28 day	PXRD, SEM, TGA, FTIR, and BET	Water vapour adsorption isotherms were reported at two temperatures At up to 14 days, CuBTC MOF structure showed minor signs of decomposition, and then it degraded and lost the porosity, surface area, and crystallinity. The degradation product was claimed to be copper hydroxide based on the sample's colour change
2015 [134]	Water vapour, P/P^o = 0–0.8	25	–	Calculations of water vapour adsorption isotherms and metal–O/ H_2O binding energies by GCMC and CMC simulations	
2015 [135]	Water vapour, P/P^o = 0–0.95	15–45	–	Pure water vapour and benzene/water vapour binary mixture isotherms and desorption activation energy studies	
2015 [136]	Water vapour, P/P^o = 0–1	25	–	Calculation of H_2O-CuBTC MOF's copper binding and hydrogen bonding using GCMC and MC simulations, pure and competitive water vapour, methanol and ethanol adsorption isotherms	
2015 [137]	Water, P = 0–100 bar	25	–	GCMC simulations to compute the adsorption isotherms for selective water removal from methanol, ethanol, and 1-propanol mixtures	
2015 [138]	Water vapour, P/P^o = 0–1	25	–	GCMC simulations to compute pure water vapour adsorption isotherm, and the effect of pre-adsorbed perfluoro-alkanes on water vapour and ammonia adsorption	
2015 [139]	Wastewater and washing mixture of 90:10 water: methanol	Ambient conditions	–	CuBTC MOF was evaluated, with other porous materials, for removing the organic impurities in wastewater produced by membrane fabrication process. It has been tested by cyclic continuous adsorption/regeneration of wastewater and washing solution, respectively, where CuBTC MOF showed 15% decay in performance after the 10th regeneration cycle	

*The max used CO_2 partial pressure was 0.1013 bar, which is comparable to the partial pressure of CO_2 in flue gases.

4.2 *Experimental*

4.2.1 Materials

Samples of CuBTC MOF synthesised and activated according to the method presented in Chapter 3 (at 100 ºC and 24 h) were used.

4.2.2 Characterisation methods

PXRD, SEM and DSC analyses were performed according to the experimental procedure given in Chapter 3.

Dynamic water vapour adsorption analysis on CuBTC MOF was performed using a dynamic vapour sorption (DVS) analyser (Surface Measurements Systems Ltd., DVS 1). The analyser was housed inside an environmental chamber at a constant temperature to ensure a stable baseline and an accurate delivery of the required relative humidity. Relative humidity values are controlled by mixing dry nitrogen and nitrogen saturated with water vapour in appropriate proportions using mass flow controllers. The DVS analyser is a gravimetric technique using a sensitive microbalance (Cahn D200) to measure changes in sample mass with the capability of recording the change in mass of lower than 1 part in 10 million. Dry nitrogen at a pressure of 2 bar is used to purge the head of balance prior to loading the sample in order to prevent the condensation of vapour inside the balance head and ensure accurate measurements. All samples were dried at 0% relative humidity (RH) for 6 h before the measurement of adsorption/desorption isotherms at various water vapour partial pressures. The water vapour adsorption isotherms of CuBTC MOF were measured at a temperature range of 25–50 ºC with relative humidity values ranging from 0–90%.

The equilibration time for each vapour pressure stage was set as maximum 6 h per stage. The criterion of changing adsorption pressures was determined by the rate of changing the mass of sample with respect to time (*i.e.* dm/dt) and a critical value of dm/dt = 0.002 (max) was specified in the instrument. When a value of dm/dt is measured as equal or smaller than 0.002, the adsorption of water vapour on the sample is believed to reach the equilibrium at the specified pressure. Then

the system moves to the next pressure stage. However, the system will move to the next pressure stage after 6 h even if the equilibrium is not reached. Changes in the sample's mass are recorded every 20 s as a function of relative humidity. The total time of an adsorption experiment is the sum of the time required for all equilibria in the adsorption/desorption stages. It is worth to note that the error associated with all dynamic water vapour experiments carried out in this work was less than 5%.

It should be noted that an experiment of water vapour adsorption on CuBTC MOF sample (degassed under vacuum) was measured using DVS vacuum in the Surface Measurements Systems Ltd. laboratory by Dr Vladimir Martis. However, all the calculations and data analysis were performed by the author.

The obtained water vapour adsorption data of studied samples were interpreted with the Dual-Site Langmuir Freundlich (DSLF) adsorption model, which has two independent sets of Langmuir model sites, Eq 4.1, [135, 140]. DSLF model is represented by the sum of two independent forms of Langmuir and Freundlich sites.

$$N = q_1 \frac{b_1 P^{1/n_1}}{1 + b_1 P^{1/n_1}} + q_2 \frac{b_2 P^{1/n_2}}{1 + b_2 P^{1/n_2}} \tag{4.1}$$

where N is the amount adsorbed per mass of adsorbent (mmol/g) at pressure P (mbar), b_1 and b_2 are the affinity coefficients of sites 1 and 2, respectively ($1/mbar^{1/n}$), and $1/n_1$ and $1/n_2$ are the heterogeneity factors (deviations from an ideal surface).

Small angle X-ray scattering (SAXS) studies: CuBTC MOF samples were filled to Lindeman capillaries (1 mm diameter, quartz capillary) and examined using the Hecus SA X-ray S3-Micro Pix Camera. SAXS patterns were recorded at a fixed wavelength λ of 1.54 Å. The PSD 50M detectors were used to acquire the data. The long spacing was calculated from the scattering angles according to Bragg formula, Eq 4.2, [141].

$$n\lambda = 2d\sin\theta \tag{4.2}$$

where n is an integral number describing the order of reflection, λ is the wavelength of the incident X-ray, d is spacing between the lattice planes and θ is the diffraction angle.

Data for SAXS experiments were represented in the form of a two dimensional image consisting of 512 vertical and 512 horizontal channels. FTI2D software was used in order to obtain *d*-spacing from the data. A one dimensional representation of the data was produced from two dimensional images by using the FTI2D to convert the two-dimensional spots to the corresponding scattering angles and then generating a plot of intensity versus 2*θ*. The analysis was carried out at room temperature and atmospheric pressure.

Fourier transform infrared (FTIR) analysis was carried out using solid FTIR Avatar 360 ESP spectrometer instrument in the wavenumber range of 650–4000 cm^{-1} with ATR accessory that contains a germanium crystal conjointly with Nicolet's OMNIC software. The analysis was carried out at room temperature and atmospheric pressure.

4.3 *Grand Canonical Monte Carlo (GCMC) simulation*

CuBTC MOF was modelled as a rigid structure with a cubic unit cell of 26.343 Å length following the work of Castillo *et al.* [121]. Lenard-Jones parameters of all atoms were taken from Dreiding force field [142] except those of copper, which were taken from UFF [143]. Partial charges of all atoms were adopted from the literature [121]. Lenard-Jones cross interactions were calculated using Lorentz-Berthelot mixing rules. A cut-off radius of 12 Å radius was used for Lenard-Jones interactions and Ewald sum was used for the electrostatic interactions' computations. The H_2O molecules were modelled as five sites molecules, in which, the Lenard-Jones parameters and partial charges were taken from TIP5P force field [144]. GCMC simulation of pure H_2O adsorption was carried out using MCCCS Towhee code [89]. The chemical potentials that are required for the GCMC simulation were computed using NPT ensemble.

4.4 *Results and discussion*

4.4.1 Dynamic water vapour adsorption onto CuBTC framework

Water vapour adsorption on CuBTC MOF was measured at 25–50 ºC and 0–90% relative humidity range. Figure 4.1a shows the measured dynamics of water vapour uptake for the CuBTC framework at 25 ºC, where the relative pressure is defined as the ratio of the water vapour pressure to the saturation pressure at the experimental measurement temperature. It was found that the interaction between the adsorbed water vapour molecules and CuBTC MOF is strong, *i.e.* significantly longer time was required for desorption to reach equilibrium than that of adsorption at the same vapour partial pressure (Figure 4.1a). The water adsorption isotherms on CuBTC MOF at 25, 35 and 50 ºC are shown in Figure 4.1b.

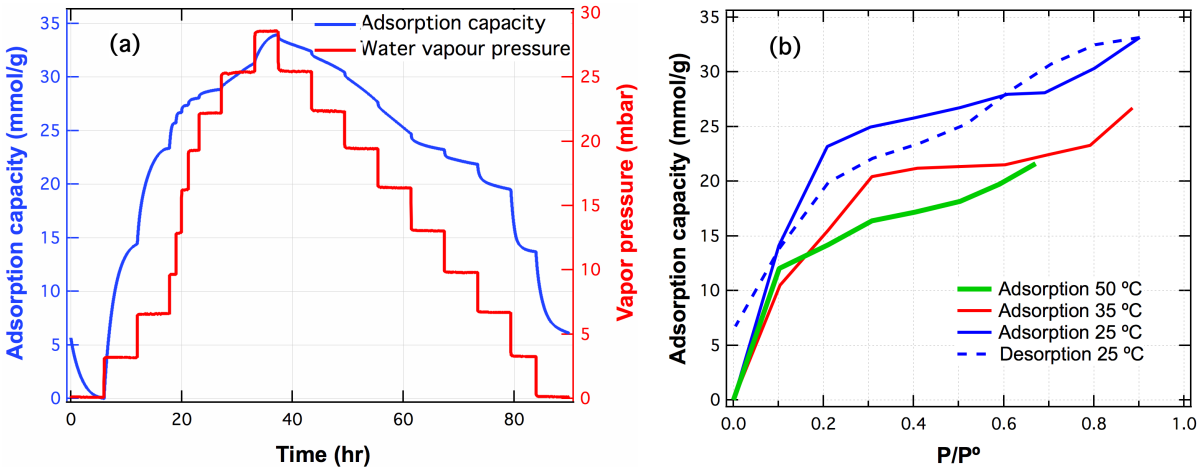

Figure 4.1. (a) Temporal water vapour adsorption and desorption on CuBTC MOF at different vapour partial pressures, 25 ºC and 90% relative humidity, (b) Water adsorption and desorption isotherms on CuBTC MOF at 25 ºC (up to 90% RH, in comparison to literature data [128]), 35 ºC (up to 90% RH) and 50 ºC (up to 70% RH).

According to the water adsorption isotherm at 25 ºC, CuBTC MOF can be classified as a type II adsorbent, which is characterised with two steep slopes and one intermediate flat region. The first rising slope at a low relative vapour pressure range (0–0.2) is largely attributed to the preferential adsorption of water vapour in the region near the copper atoms of the primary pores. Molecular simulations showed that water molecules have a strong affinity to copper centres due to their large dipolar moment [121]. Therefore, the interactions between the water vapour

molecules and the unsaturated copper centres are expected as immediate under humid conditions, leading to a sharp increase of water vapour uptake at the initial stage of adsorption.

The shallow slope over the relative pressure range between 0.2 and 0.8 corresponds to the filling of the CuBTC MOF primary pores caused by the formation of water clusters due to hydrogen bonding [126], *i.e.* saturation of the primary pores. This hypothesis was based on the theoretical calculation of Henry coefficient using the grand canonical Monte Carlo simulations reported in the literature [121]. Simulation results showed that Henry's coefficient of water vapour molecules adsorption within the void space of CuBTC MOF cages (*ca.* 4.6×10^{-6} mmol/g.Pa) is significantly lower than one for the unsaturated copper centres (*ca.* 2.0×10^{-2} mmol/g.Pa) [121].

The final rise of adsorbed uptake for water vapour, which occurs at a high relative pressure of >0.8, is associated with the adsorption of water molecules in the side pockets or small pores. The nature of these side pockets in the CuBTC framework is believed to be hydrophobic [135], *i.e.* the reluctance to form strong interactions with water vapour molecules, and hence the filling of the side pockets with water vapour only occurs at the final stage of adsorption with relatively high vapour partial pressure. The adsorption isotherms at 35 and 50 ºC are similar to the one at 25 ºC with shifted relative pressure ranges for relevant adsorption stages.

CuBTC frameworks have shown clear hysteresis between adsorption and desorption isotherms at 25 ºC but in a thermodynamically impossible manner, *i.e.* the crossing of desorption isotherm with the adsorption isotherm. Such hysteresis phenomena are likely caused by the partial decomposition during the adsorption step. Therefore, in the desorption step, a significant amount of water desorbs from the decomposed CuBTC MOF due to the weak binding between water molecules and the decomposed solid phase resulting in a steep decline of the desorption isotherm. To confirm these results, PXRD analysis of the fresh (after activation) and used CuBTC MOF was carried out, and the relevant patterns are shown in Figure 4.2. For the sample used in the dynamic vapour adsorption experiment at 25 ºC (denoted as U-25), PXRD pattern shows that the incoming water molecules

can interrupt the CuBTC MOF coordination evidenced by the variation in the peak intensity of (222) and (200) crystallographic planes (Figure 4.2), where Cu atoms are present [145], in addition to a disruption in the baseline of PXRD pattern. These results confirm that the water adsorption at 25 ºC caused alteration of CuBTC MOF coordination with partial structure decomposition, while the overall crystalline structure of CuBTC MOF is still reasonably maintained.

Furthermore, it is also found that not all the water vapour was desorbed when the partial pressure of water was returned to zero, indicating the retention of water vapour molecules within the partially decomposed framework. This phenomenon is probably the result of the water-unsaturated copper centres strong binding. The theoretical value of adsorbed water on unsaturated copper sites can be estimated as 5 mmol/g assuming one molecules of water per copper atom, which is close to the remaining uptake (*i.e.* 6.73 mmol/g) at the end of desorption process. Such absorbed water molecules on unsaturated copper sites can only be removed by activation at high temperatures.

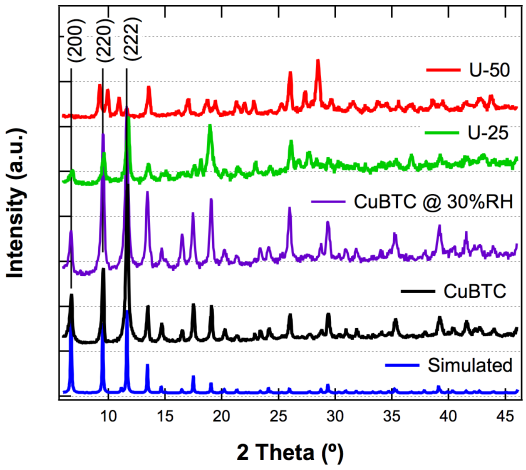

Figure 4.2. PXRD patterns for used CuBTC MOF from dynamic water vapour adsorption under various conditions in comparison to the PXRD pattern of fresh CuBTC MOF.

The water vapour adsorption capacity of CuBTC framework at 25 ºC and *ca.* 28 mbar water vapour pressure (RH = 90%) was measured as 33.3 mmol/g, which is in good agreement with reported values in the literature [126, 128, 135], Figure 4.1a and b. Water vapour adsorption capacity was found to decline with increasing the temperature (Figure 4.1b), where the measured adsorption uptake dropped by

ca. 35% with increasing adsorption temperature from 25 ºC to 50 ºC. It is apparent that the water vapour adsorption is much more preferable than CO_2 adsorption, *i.e.* considerable higher water vapour uptake of *ca.* 21.7 mmol/g at 50 ºC (up to 70% RH, *ca*. 94 mbar) in comparison with the CO_2 uptake of *ca.* 0.258 mmol/g (Chapter 3) under similar conditions. The isosteric heat of water vapour adsorption was estimated (based on fitting the experimental isotherms to Dual Sites Langmuir-Freundlich model [135, 140], then using Eq 3.2) as 48.6 kJ/mol, which is comparable to the reported values, *i.e.* 48.5 and 50.7 kJ/mol [127, 146], suggesting the possible chemisorption of water vapour on CuBTC MOF. Comparing the isosteric heat of adsorption of water vapour to that of CO_2 (*ca.* 27 kJ/mol, as shown in Chapter 3) gives further evidence of the high affinity of CuBTC MOF to the former. This can be explained by (*i*) the strong interaction between the unsaturated copper centres and water molecules and (*ii*) the hydrophilic nature of CuBTC MOF with water contact angles close to 0° [147]. Fitting of adsorption data of water vapour on CuBTC MOF to DSLF model and the calculations of the isosteric heat of adsorption can be found in Appendix A.5.

4.4.2 Moisture stability of CuBTC framework

Water vapour adsorption on CuBTC MOF at high temperatures of 40–50 ºC was measured, as shown in Figure 4.3. The framework structure of CuBTC MOF was found to irreversibly change by increasing the water vapour partial pressure at high temperatures. Sudden drops in vapour uptake were measured at high relative pressure, as seen in Figure 4.3, which indicates the collapse of the porous structure of CuBTC MOF.

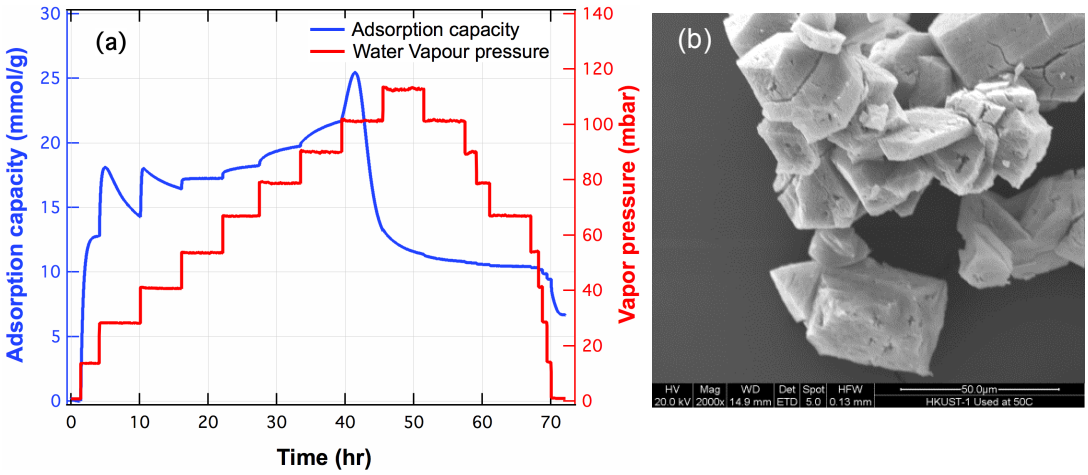

Figure 4.3. (a) Temporal water vapour adsorption and desorption on CuBTC MOF at 50 ºC (up to 90% RH). (b) SEM images for the used CuBTC MOF after water adsorption at 50 ºC with 90% RH.

The PXRD patterns of fresh and used CuBTC MOF at 50 ºC (denoted as U-50) are shown in Figure 4.2. The PXRD analysis shows that for the sample U-50, the PXRD pattern changed fundamentally from ones of the original CuBTC MOF and U-25 (Figure 4.2). Thermal stability of CuBTC MOF reported in the literature at (100–600 ºC) was evaluated using the *in situ* PXRD characterisation showing that the framework is thermally stable up to 260 ºC [65]. Therefore, the effect of temperature in the dynamic vapour adsorption experiments can be excluded. SEM characterisation (Figure 4.3b) also shows visible cracks and holes on the crystal surface in used samples.

In addition, it can be seen from Figure 4.3a that there are two anomalous peaks at adsorption stage of *ca.* 28 and 41 mbar, which can be attributed to a partial structure decomposition. This hypothesis was proved by analysing the PXRD pattern of used sample after it finished the adsorption steps up to 30% RH (*ca.* 41 mbar), Figure 4.2. The PXRD pattern showed an increase in the amorphous content which caused a disruption of the PXRD baseline, and the change in the relative length of peaks intensities.

Table 4.2 provides a summary of the temperature and relative humidity range for hydrothermally stable CuBTC MOF under dynamic vapour adsorption conditions.

Table 4.2

Conditions for maintaining moisture stability of CuBTC framework and the corresponding maximum water vapour adsorption capacity.

T (ºC)	RH (%)	P_{Vapour} (mbar)	Maximum H_2O adsorption uptake (mmol/g)
25	0–90	0–28.5	33.3
35	0–90	0–42.5	27.0
40	0–80*	0−60.0	25.0
45	0–70*	0–82.0	23.0
50	0–70*	0–89.9	21.6

*Structure collapsed at RH> 70%

The strong bonds between water molecules and the unsaturated metal sites in the framework are believed to induce the decomposition of CuBTC MOF at high adsorption temperatures and high relative humidity. Under such conditions, the aggregation of adsorbed water molecules near the metal sites may gradually displace the coordinated carboxylate groups of BTC ligands from the copper centres leading to the final break of the metal-ligand coordination. Such a phenomenon was previously observed in MOF-5 framework [$Zn_4O(BDC)_3$] (DBC = benzene-1,4-dicarboxylic acid) upon its exposure to humid air, in which the humid air not only displaced the ligand coordination of MOF-5 from the zinc metal centres but also penetrated into the metal building blocks and changed the structure into MOF-69C [$Zn_3(OH)_2(BDC)_2$], which is hydrothermally unstable at ambient conditions [22, 148].

Quantum mechanical calculations based on cluster models [114] were also developed for predicting the water adsorption on open metal sites (OMSs) demonstrating the change of metal-ligand coordination by the invasion of water molecules. Although *in situ* PXRD experiments were performed to validate the model predictions [114], the experimental evidence was not adequate to prove the true nature of CuBTC MOF decomposition under humid conditions. Recently, a mechanochemical method has been developed to quickly reconstruct the moisture-degraded CuBTC MOF [149]. However, it is still of great importance to reveal the underlying mechanism of the decomposition of MOFs with OMSs under humid conditions with concrete experimental proof, and hence help the ultimate

modification of MOFs with superior hydrothermal stability, while maintaining their properties of interest.

4.4.3 Decomposition mechanism of CuBTC MOF under humid conditions

It can be seen above that there is clear change in the peaks intensities of the PXRD patterns, in which, such changes can be attributed to changes in either types or positions of atoms on their crystallographic planes. For sample U-25, in addition to the partial structure decomposition, the positions of Cu atoms are shifted as a result of coordinating water molecules with the CuBTC MOF complex. Extended X-ray absorption fine structure (EXAFS) analysis [150] showed that the water-Cu coordination could interfere with CuBTC MOF coordination by widening Cu-O-C angle leading to the stretch of $Cu_2C_4O_8$ cage (Figure 4.4).

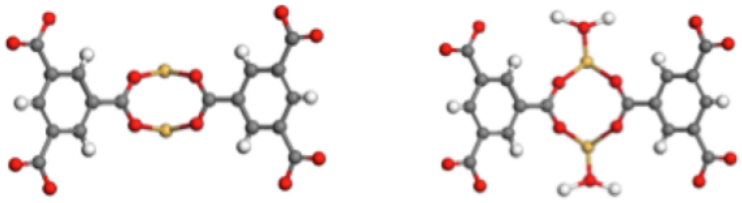

Figure 4.4. Widening of Cu–O–C angle in Cu-BTC coordination caused by water-Cu interaction (adapted from reference [150]). Yellow: copper, red: oxygen, grey: carbon, white: hydrogen.

SAXS analysis of the fresh CuBTC MOF (Figure 4.5a) shows that families of (222) and (200) planes produced diffraction peaks at 2θ angles of 5.9º and 6.9º with measured *d*-spacing of 14.7 Å and 12.7 Å, respectively, corresponding well to the theoretical values of the space between diffracting planes of (222) of *ca.*15 Å and (200) of *ca.* 13 Å [145]. Sharp diffraction peaks in Figure 4.5a also indicate a well-organised periodical porous structure of the fresh CuBTC MOF. For U-25 (Figure 4.5b), diffraction peaks were also detected at 2θ positions of *ca.* 5.9º and 6.9º suggesting the retaining parallel positions of (222) and (200) planes in the crystalline structure of U-25. However, in comparison with Figure 4.5a, the pronounced deterioration in the shape and intensity of diffraction peaks in Figure 4.5b are very noticeable implying that positions of atoms on these planes are disordered due to the water molecule coordination to OMSs.

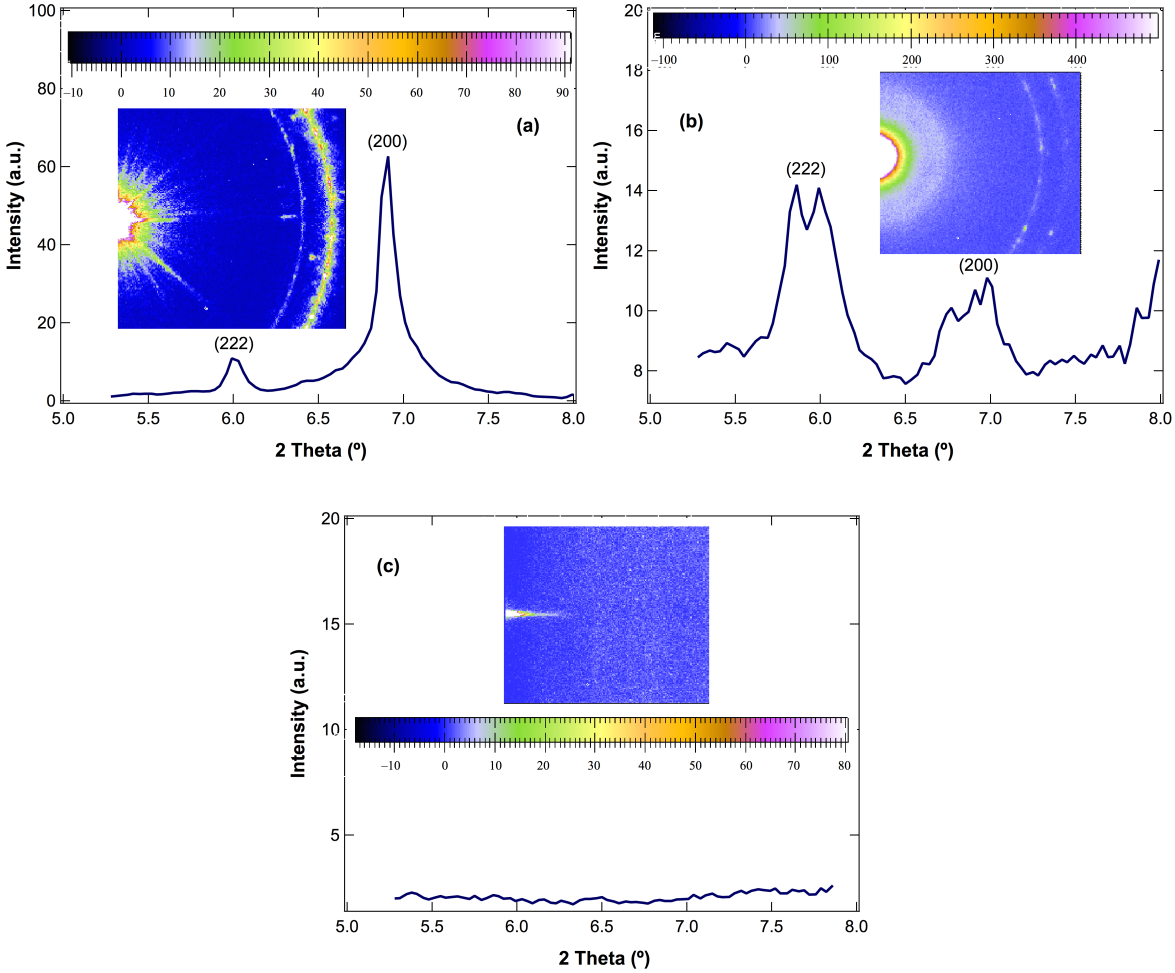

Figure 4.5. SAXS patterns of (a) activated fresh CuBTC MOF; (b) U-25 (used CuBTC MOF after dynamic water vapour adsorption at 25 °C with 0–90% RH) and (c) U-50 (used CuBTC MOF after dynamic water vapour adsorption at 50 °C with 0–90% RH). Insets: representative 2D SAXS patterns.

In a fresh CuBTC MOF sample, atoms are self-assembled in its lattice with their preferential orientations. The degree of orientation is reflected as diffraction rings around the incident beam in a 2D scattering SAXS pattern (insets of Figure 4.5a and b). For CuBTC MOF (inset of Figure 4.5a), well-defined rings with equal intensities around the primary beam were measured, indicating that atoms in the fresh CuBTC MOF are oriented perfectly according to their coordination properties with other atoms around them, *i.e.* a highly crystalline solid. In contrast, SAXS result from U-25 produces a 'halo' of intensity (inset of Figure 4.5b), which shows indistinct concentric rings with uneven and low diffraction intensities (4 times lower than the ones of fresh sample). This result demonstrated that, during and after

water vapour adsorption at 25 ºC, adsorbed water molecules within CuBTC framework could disrupt the CuBTC MOF coordination significantly.

No peak intensities were detected for U-50 using the SAXS analysis (Figure 4.5c) suggesting that the crystalline structure is no longer periodically ordered and the cubic lattice of CuBTC MOF have been destroyed after the dynamic adsorption of water vapour at 50 ºC.

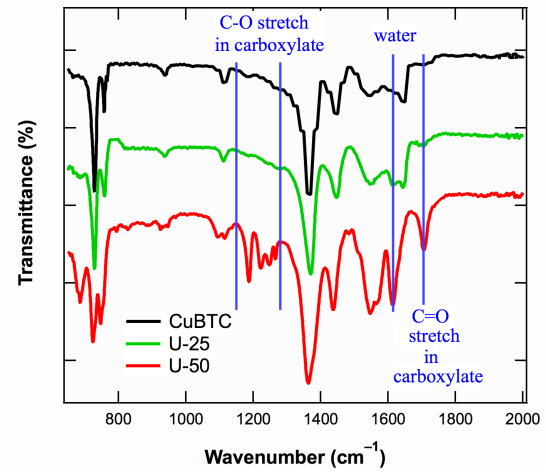

Figure 4.6. FTIR spectra of activated fresh CuBTC MOF (solid black), U-25 (solid green) and U-50 (solid red).

The structural variation of CuBTC MOF after water adsorption was further examined by FTIR spectroscopy (Figure 4.6). The FTIR spectrum of fresh CuBTC MOF is similar to that obtained for the U-25 indicating the retention of CuBTC MOF coordination in the CuBTC MOF after water adsorption at 25 ºC (with maximum 90% RH). However, the vibrational properties of the bidentate carboxylate ligands in U-25 (*i.e.* characteristic bands at 1645, 1445 and 1375 cm^{-1}) are different from ones in fresh CuBTC MOF. The bending mode of molecular water is also observable for U-25 at 1620 cm^{-1}. This is the evidence of the stretch of $Cu_2C_4O_8$ cage caused by the adsorbed water molecules near Cu sites.

Compared to the fresh CuBTC MOF and U-25, U-50 exhibits different vibrational properties in its COO moiety, *i.e.* the band shift and stronger intensity for the asymmetric stretch of O=C–O at 1645 cm^{-1} and the symmetric modes at 1445 and

1375 cm^{-1}. A notable change in the intensity of band 1620 cm^{-1} was also found for U-50, revealing more water molecules were bonded with CuBTC MOF during the water vapour adsorption at 50 ºC. Furthermore, the spectrum of U-50 clearly shows the appearance of characteristic bands of carboxylic acids, *i.e.* the band at 1705 cm^{-1} for C=O stretching and bands at 1150−1280 cm^{-1} for C–O stretching [133, 151], showing the transformation of the CuBTC MOF carboxylate groups to their protonated acid analogues during water adsorption at 50 ºC.

Therefore, in conjunction with the results from PXRD (Figure 4.2), SEM (Figure 4.3b) and SAXS (Figure 4.5), it can be confirmed that the incoming water molecules can interpenetrate CuBTC MOF complex and open coordination sites of Cu centres resulting in the decomposition of CuBTC MOF. The formation of hydrogen bonds between the protons of water molecules and the CuBTC MOF complexes is believed to play an important role for the decomposition [114].

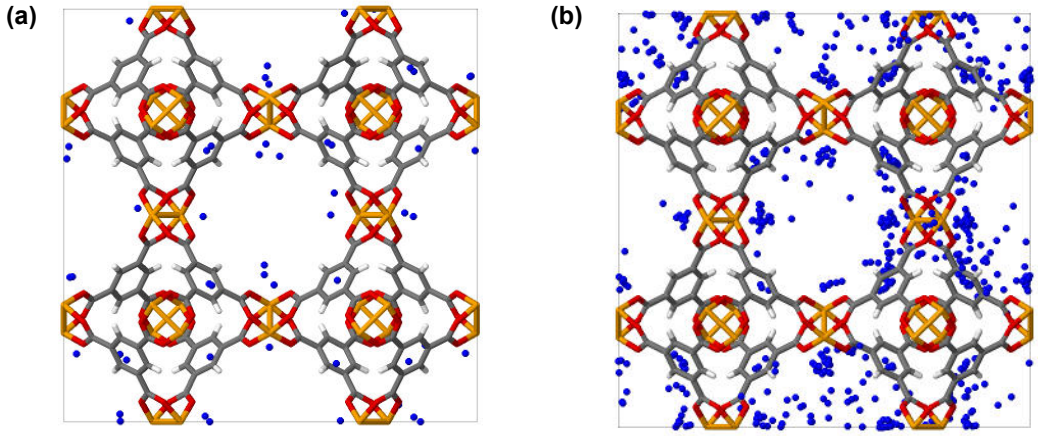

Figure 4.7. GCMC simulation of pure H_2O adsorption on CuBTC framework (snapshot based on the average of 20 configurations): (a) 2.7 mbar and (b) 8 mbar.

Grand Canonical Monte Carlo simulation has shown that water molecules prefer to aggregate around the OMSs during water adsorption (Figure 4.7). Water molecules first coordinate with OMSs in a CuBTC MOF complex, which is obviously the main reason for stretching the $Cu_2C_4O_8$ cage as confirmed by the EXAFS analysis reported previously [150]. Other water molecules near the CuBTC MOF complexes then tend to have their protons directed at the oxygen of COO

moieties in the CuBTC MOF complex forming hydrogen bonds with the complex and hence changing the coordination state of the carboxylate in the complex [114]. Such intervention of water molecules in the CuBTC MOF coordination results in the replacement of an oxygen atom of the carboxylate-Cu coordination with one oxygen atom in a water molecule; and hence leads to the displacement of BTC ligands from coordination sites on Cu and the collapse of MOF's scaffolding.

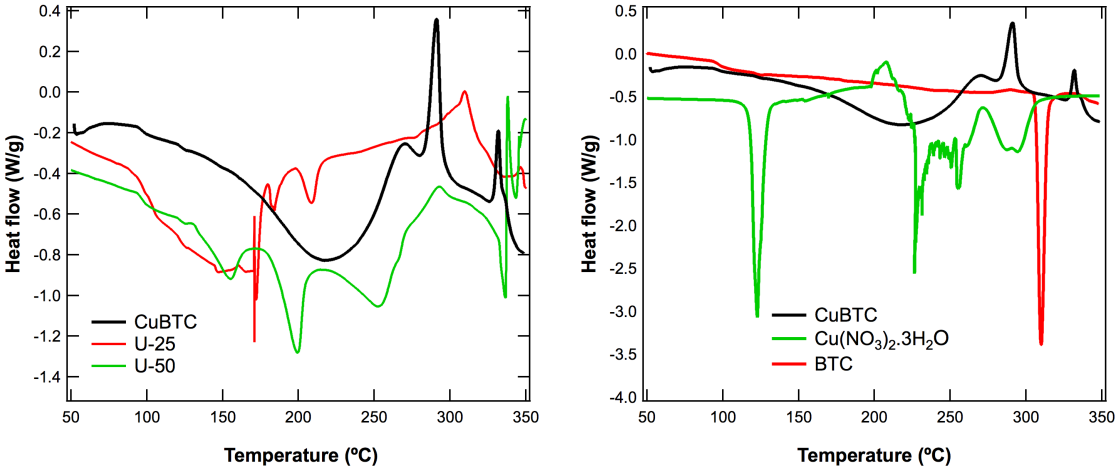

Figure 4.8. a) DSC curves of activated fresh CuBTC MOF (solid black), U-25 (solid red) and U-50 (solid green), (b) DSC curves of fresh CuBTC MOF (solid black), copper nitrate trihydrate (solid green) and BTC (solid red).

In order to prove the partial displacement of carboxylic group of BTC from Cu sites after dynamic water vapour adsorption at 50 ºC, DSC analyses were performed (Figure 4.8a). DSC curves of three materials showed endothermic events with the same onset temperature of 50 ºC and different recovery temperatures (*ca.* 220 ºC for fresh CuBTC MOF and U-25 and *ca.* 260 ºC for U-50). This thermal event can be attributed to the loss of water molecules from these three materials. Compared to the fresh sample, U-25 and U-50 are expected to have more coordinated water molecules within their frameworks leading to higher endothermic heat flows at the initial stage of heating. In curves of U-25 and U-50, sharp endothermic peaks appearing in the range of 50–260 ºC may be a result of sudden water evaporation due to the break of hydrogen bonds among water molecules within the pores of CuBTC MOF [152]. After the recovery temperature of 220 ºC, two exothermic peaks at *ca.* 284 ºC and 329 ºC were observed for CuBTC MOF corresponding to the thermal transition of Cu in CuBTC MOF during the heating process (Figure

4.8a, the black line). However, these two peaks were replaced by one broad exothermic peak at a temperature range of 280 to 340 ºC in the thermogram of U-25 (Figure 4.8a, the red line). This phenomenon is probably resulted from the overlapping of the two exothermic peaks in the thermogram of fresh CuBTC MOF due to the structure disruption by water-Cu coordination.

The thermal transition of Cu in U-50 is still identifiable. However, an endothermic peak, which starts at 310 ºC and ends up at 340 ºC (Figure 4.8a the green line), is distinguished and can be linked to the melting of BTC ligands that is displaced by water-Cu coordination. DSC curve of pure BTC ligands (Figure 4.8b) shows a sharp endothermic peak at 320 ºC. The thermal event of U-50 in the range of 310–340 ºC can be explained by the presence of fully and partially displaced BTC ligands within CuBTC MOF after water vapour adsorption reconfirming the results found by the SAXS and FTIR analyses.

4.4.4 Cyclic water vapour adsorption on CuBTC MOF at ambient temperature

In general, the stability issue of CuBTC MOF under humid conditions is the major hurdle for its application for CO_2 capture in practice. It was also found that, even at 25 ºC, long exposure of CuBTC to water vapour caused the decomposition of its framework, as evidenced by the result from the equilibrium adsorption of water vapour (Figure 4.9).

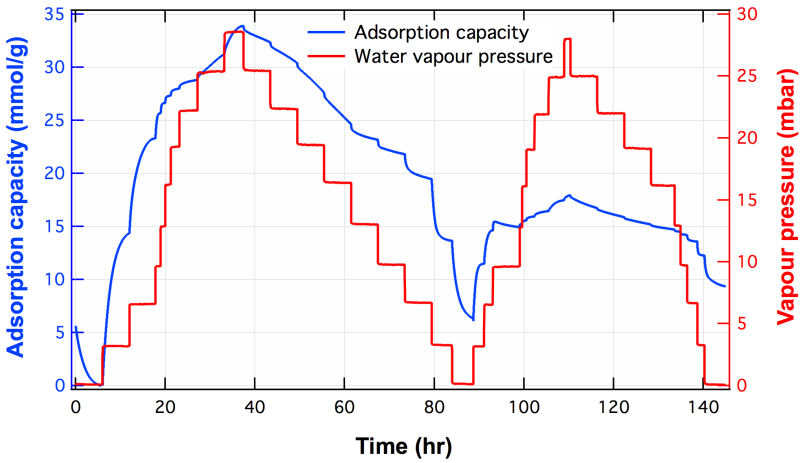

Figure 4.9. Two cycles of dynamic water vapour equilibrium adsorption and desorption on CuBTC MOF at 25 ºC.

Previously in this Chapter, it was deduced that the partial degradation of CuBTC framework occurred at 25 ºC. Herein, the second water vapour adsorption cycle was performed without the thermal regeneration in order to quantify the effect of the partial structural degradation of CuBTC MOF on the subsequent water vapour uptake behaviour. As shown in Figure 4.9, an obvious decrease of *ca.* 48% in the water vapour uptake was observed in the second cycle clearly showing the adverse impact of the partial degradation of the framework on the adsorption capacity of CuBTC, as well as indicating the relevant performance for capturing CO_2 under humid conditions. In addition, further partial structure decomposition was found in the adsorption of second cycle represented by the anomalous peak (as discussed in section 4.4.2) at the vapour pressure stage of *ca.* 10 mbar.

The CuBTC sample from the two-cycle experiment (at 25 ºC) was characterised by PXRD and SEM analysis showed further degradation of the structure as shown in Figure 4.10. In comparison to the sample from one cycle of water vapour adsorption, the baseline of the spent sample after two cycles drifted further up indicating an increased amount of the amorphous phase in the material. By comparing the PXRD patterns of spent CuBTC samples to the simulated one, the extra peaks (2θ = 18, 23 and 27) suggested the reorganisation of the CuBTC framework by the long exposure to the water vapour. The SEM image in Figure 4.10 shows the damaged CuBTC crystals losing the sharp edges and appearing the surface cracks, though the octahedral shape of CuBTC crystal is still recognisable.

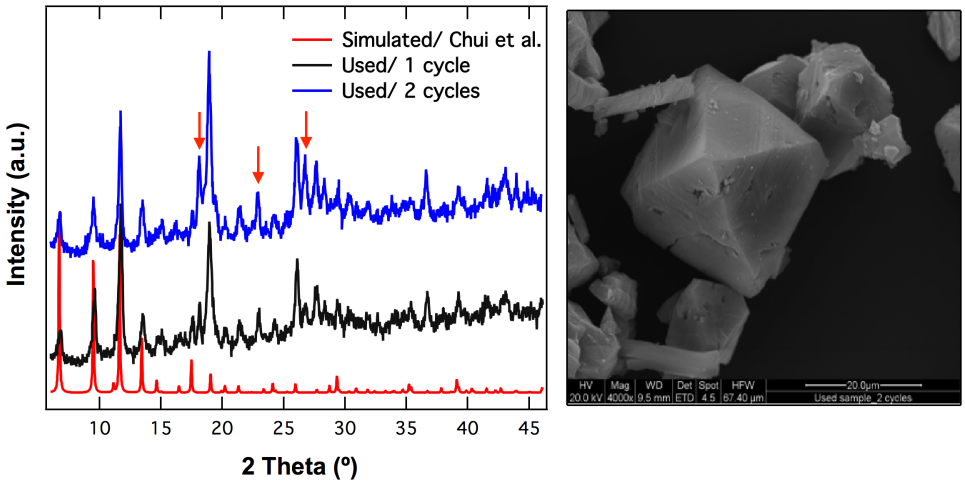

Figure 4.10. PXRD patterns of the spent CuBTC MOF sample after 1 and 2 cycles of water vapour adsorption at 25 ºC compared to simulated pattern of Chui et al. [19] and SEM image of the spent CuBTC MOF sample after 2 cycles of water vapour adsorption.

It is worth noting that, in the first cycle, the equilibrium time required in the desorption stage was much longer than that of the adsorption stage showing the strong interactions between water molecules and CuBTC MOF. Figure 4.9 also shows that in the first adsorption cycle, the time required for the adsorption equilibrium varied at different pressure stages of water vapour adsorption, *i.e.* fast equilibrium at *ca.* 7–22 mbar vapour pressure and slow equilibrium at *ca.* 0–7 mbar as well as >22 mbar. The time it took to achieve the adsorption equilibrium was about one hour in the pressure region of *ca.* 7–22 mbar, whereas about six hours for the initial adsorption stage. This phenomenon can be attributed to the adsorption behaviour of water molecules inside the pores of CuBTC MOF, where the adsorption in the intermediate region is mainly associated with the filling of main pores with water molecules as discussed in section 4.4.1. For the stages at low and high vapour pressures, the long time to achieve the adsorption equilibrium could be attributed to the affinity of the main pores and side pockets to water molecules.

Table 4.3
The chemical composition of natural and flue gases with their relevant emissions conditions.

	Natural gas [27, 153]	Flue gases [1, 2]
Separation system	CO_2/CH_4	CO_2/N_2
Pressure (bar)	60–70	0–1
Temperature (ºC)	Ambient	50–75
CO_2 (mol %), max	1–40	15
H_2O	3–8 $x10^{-3}$ % (mol)	5–7 % (mol)
N_2 (mol %)	—	70–75
CH_4 (mol %)	60–95	—
CO_2 in exhaust clean gas (mol %)	<(3–4)	0.03

Since CuBTC MOF responded differently to the vapour partial pressure during the equilibrium adsorption process, one can then utilise these features to design non-equilibrium adsorption processes (in terms of water vapour adsorption) to maintain the stability of materials during the application. Therefore, apart from the modification of the materials (*e.g.* to make MOFs hydrophobic), the design of the operation fashion for the process employing MOFs as the adsorbent may be another solution for applying MOFs in practice. The following experiments were then designed based on two scenarios, i.e. CO_2 capture from natural gas and flue gas streams. CO_2 removal from the natural gas is also a crucial step to mitigate the corrosion problem associated with the transportation of natural gas in pipelines, where water vapour usually exists with a partial pressure of *ca*. 5.6 mbar (calculated based on the total pressure and water vapour content in natural gas, Table 4.3). Table 4.3 summarises the chemical compositions and the typical emissions conditions of natural gas (after the dehydration process) and flue gas.

4.4.4.1 Hydrothermal stability of CuBTC MOF in cyclic water vapour adsorption under natural gas emissions conditions

To assess the ability of CuBTC MOF to withstand the water vapour in the natural gas for CO_2 capture, conditions of ambient temperature and 6 mbar water vapour pressure (Table 4.3) were used for the cyclic water adsorption experiments. According to the equilibrium adsorption measurement procedure of CO_2 given in Chapter 3, as well as the literature data [116, 118], CO_2 adsorption on CuBTC MOF took about 15–120 min to reach the equilibrium. Therefore, the exposure

time of 15 min and 120 min was investigated in the cyclic experiment to evaluate the stability of CuBTC MOF under the dynamic conditions with humidity. This scenario was created based on the fact that CO_2 adsorption is the primary process and the regeneration of the adsorbent is needed when it is saturated with CO_2. Figure 4.11 shows the adsorption dynamics of cyclic water vapour adsorption on CuBTC MOFs at ambient temperature with the exposure time of 15 min and 120 min, respectively.

Under natural gas emission conditions with a maximum water vapour pressure of 6 mbar (Figure 4.11a), CuBTC MOF was found to be stable with 15 and 120 min per pressure stage. With the 15 min exposure time per pressure stage, it was found that the water vapour adsorption did not reach adsorption equilibrium because (i) a continuous increase in water uptake was measured as shown in Figure 4.12a and (ii) desorption stages are less prominent than the adsorption stages. At the end of the fourth cycle, the desorption of water vapour from CuBTC was still not complete with *ca.* 78% of the water uptake retained in the framework. However, the water vapour dynamics showed no sign of the decomposition of materials, which was also confirmed by the post-adsorption's PXRD analysis, as presented in Figure 4.13. The maximum water uptake during 5.5 h cyclic adsorption (the 4^{th} cycle) with 15 min exposure time per pressure stage is *ca.* 12.8 mmol/g.

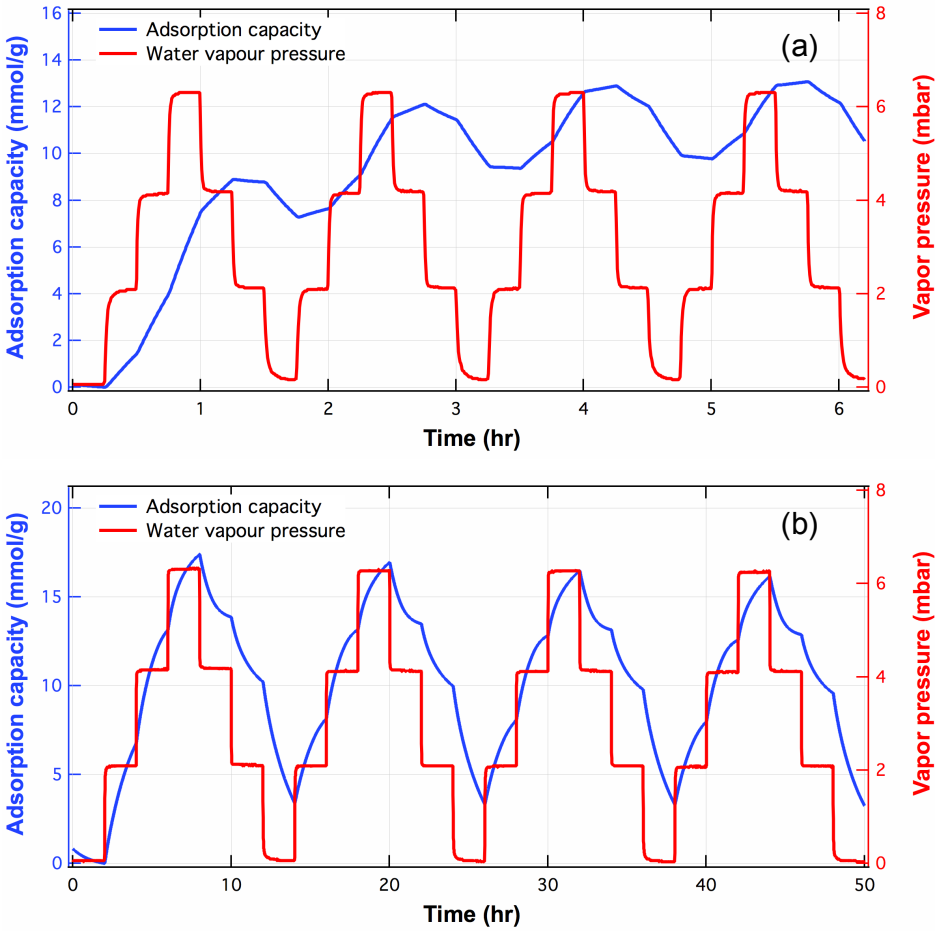

Figure 4.11. Cyclic water vapour adsorption on CuBTC MOF at 25 ºC with (a) 15 min exposure time per stage and (b) 120 min exposure time per stage.

The exposure time of 2 h per stage was found to be able to shift the system towards equilibrium even though it was not reached. A full adsorption-desorption cycle was measured as shown in Figure 4.11b, in which complete desorption of water vapour from CuBTC was not achieved either, *i.e. ca.* 3.3 mmol water in one gramme of CuBTC was always measured at the end of desorption cycle (The theoretical value of adsorbed water on unsaturated copper sites is 5 mmol/g assuming one molecules of water per copper atom). This behaviour is expected since water vapour molecules undergo chemisorption on the open metal sites of CuBTC MOF and, normally, vacuum and high temperatures were needed to enable the full desorption of water molecules from the framework as discussed earlier in this Chapter.

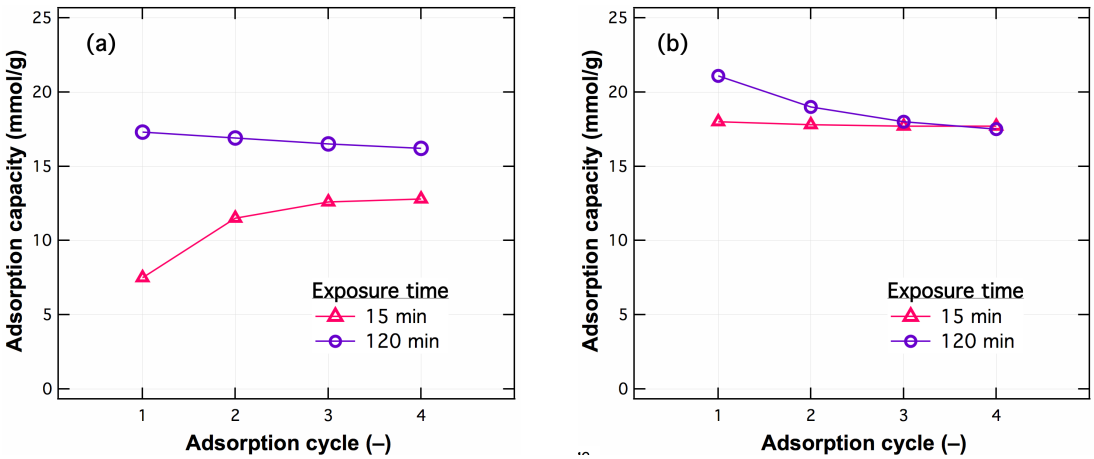

Figure 4.12. Water vapour adsorption capacity on CuBTC MOF as a function of the adsorption cycles for (a) natural gas emission conditions, 6 mbar water vapour partial pressure and 25 ºC; (b) flue gas emission conditions, 70 mbar water vapour partial pressure and 50 ºC.

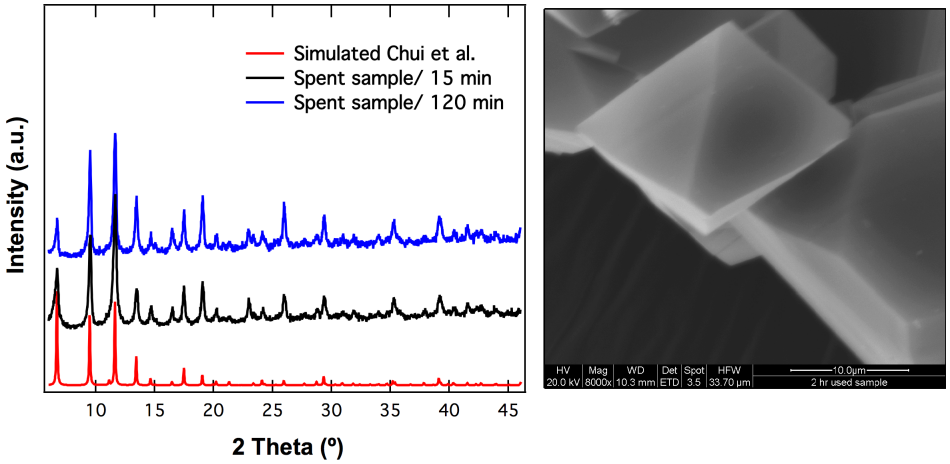

Figure 4.13. PXRD patterns of the used CuBTC MOF sample with 15 and 120 min exposure time per water vapour adsorption stage at 25 ºC and 6 mbar compared to simulated pattern of Chui et al. [19], and SEM image of the used CuBTC MOF sample with 120 min exposure time.

The 2 h per pressure stage was believed to drive the adsorption of water vapour to approach the equilibrium at 6 mbar (maximum) water vapour partial pressure since a nearly constant maximum uptake of *ca.* 16.2–17.3 mmol/g was obtained in each cycle, as shown in Figure 4.12 b. In addition, Figure 4.11 b also shows that the adsorption curves possessed the logarithmic shape rather than the linear one observed in the case with 15 min exposure time per stage. The decrease in the slope of the adsorption curve as a function of time (logarithmic shape curves) suggests that the mass change of the sample is diminishing, *i.e.* approaching the equilibrium of the adsorption.

The dynamic curves of the water uptake and the post-adsorption analysis of the spent samples (PXRD and SEM as in Figure 4.13), both suggested a stable material after 48 h of the cyclic adsorption experiment. The results indicate that CuBTC MOF might be a suitable candidate for CO_2 capture from natural gases based on a properly design swing process.

4.4.4.2 Hydrothermal stability of CuBTC MOF in cyclic water vapour adsorption under flue gas emissions conditions

Previously, the complete decomposition of CuBTC MOF was measured in the equilibrium adsorption of water vapour with long exposure time (6 h per stage, RH = 0−90%, temperatures of > 35 ºC). In this work, the non-equilibrium adsorption (in terms of water vapour) under the flue gas emission condition (50 ºC and *ca.* 70 mbar of water vapour partial pressure) was studied to assess the hydrothermal stability of CuBTC MOF in the cyclic water vapour adsorption. Figure 4.14a and b show the adsorption dynamics of cyclic water vapour adsorption on CuBTC MOFs at 50 ºC with the exposure time of 15 min and 120 min, respectively.

It was found that the non-equilibrium operation could retard the rate of CuBTC decomposition under flue gas emission conditions. As seen in Figures 4.14a and 4.14b, when 15 min exposure time per stage was applied, CuBTC MOF showed nearly complete stability, which was also evidenced by the PXRD analysis of the spent sample (Figure 4.15). Besides, in comparison to the adsorption under natural gas emission condition (Fig. 4.11a), a more equilibrated behaviour with no further increase of adsorption capacity in desorption stages was observed for the water vapour adsorption under the flue gas emission condition. This can be explained by the higher vapour partial pressure (max. 70 mbar) of flue gases than that of natural gases (max. 6 mbar). Figure 4.14a showed that the water uptake at vapour pressure stages of < 54 mbar increased in a linear fashion with respect to adsorption time, showing the non-equilibrated adsorption behaviour. On the other hand, the logarithmic growth in water uptake was measured at vapour pressure stages of ≥ 54 mbar suggesting the near equilibrium adsorption. The maximum uptake of water vapour during all cycles was in a range of 17.7–18.0 mmol/g at 70

mbar (Figure 4.12b), which was close to the value from the equilibrium adsorption (Figure 4.3) suggested an overall equilibrium of adsorption stages.

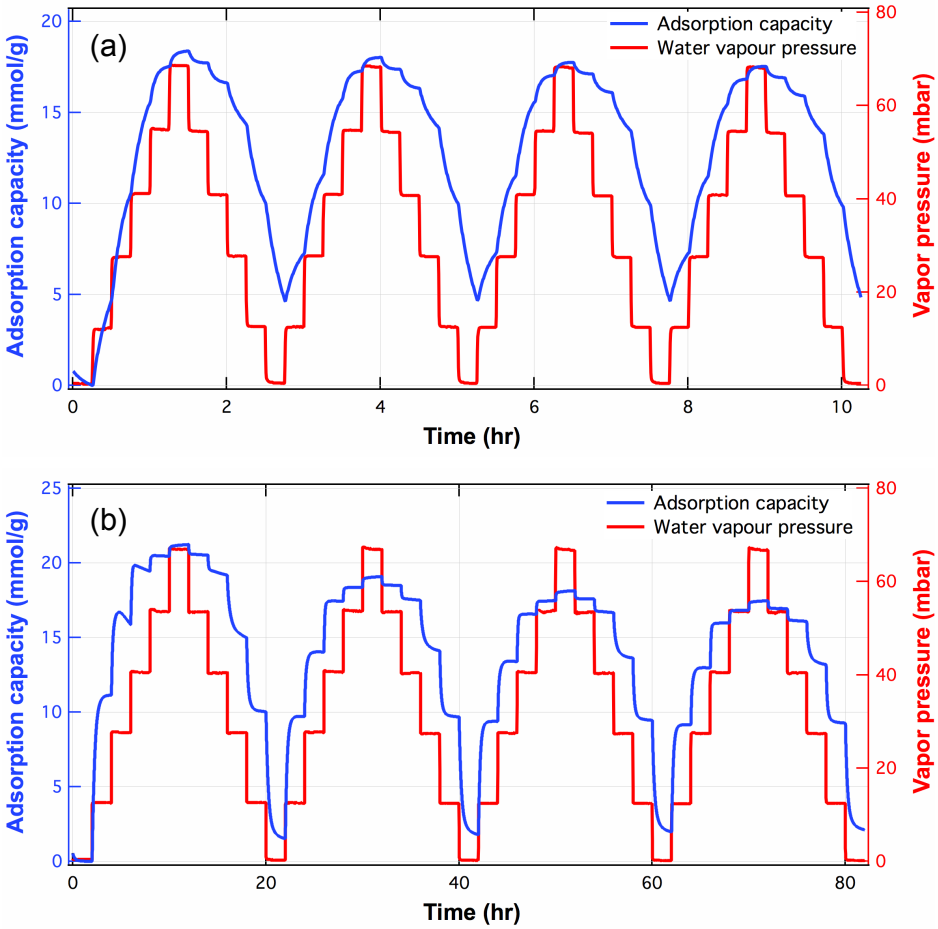

Figure 4.14. Cyclic water vapour adsorption on CuBTC MOF at 50 ºC with (a) 15 min exposure time per stage and (b) 120 min exposure time per stage.

At a high water vapour partial pressure of the flue gas condition, 120 min exposure time caused the partial degradation of CuBTC framework as evidenced by the anomalous peaks in the first adsorption cycle, as well as the adsorption equilibrium. A decline in the adsorption capacity was measured during the cyclic adsorption experiment, *i.e.* by *ca.* 22.5% by comparing the saturated uptake of the first cycle (21.1 mmol/g) to that of the fourth cycle (17.5 mmol/g), as shown in Figure 4.12 b. This could be attributed to the extended exposure time at relatively high vapour partial pressure of 70 mbar. The partial structure decomposition of CuBTC MOF under flue gas emission conditions and 120 min exposure time was

also confirmed by the PXRD and SEM analysis of the spent sample (Figure 4.15) from the cyclic experiment. As can be seen from Figure 4.15, a slight disruption in the baseline of the PXRD pattern was observed as a sign of an increase in the amorphous content of the spent sample, in addition to the significant surface damage shown in the SEM image (Figure 4.15).

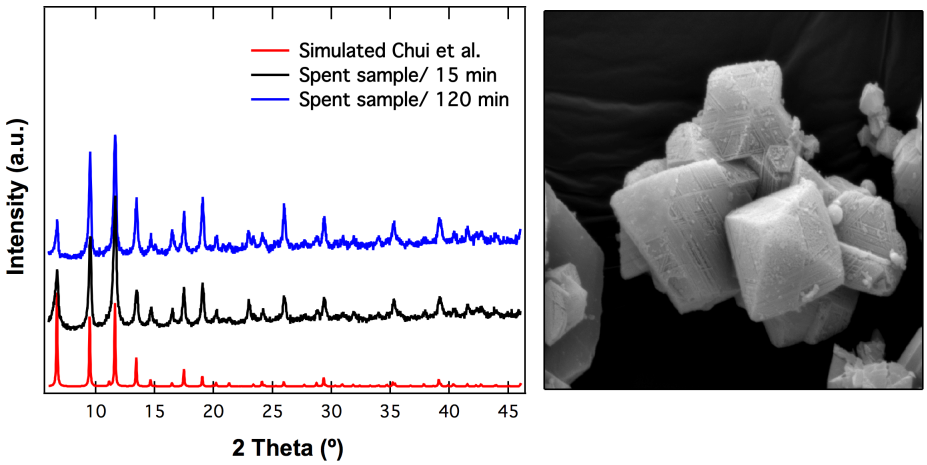

Figure 4.15. PXRD patterns of the spent CuBTC MOF sample with 15 and 120 min exposure time per water vapour adsorption stage at 50 ºC and 70 mbar compared to simulated pattern of Chui et al. [19], and SEM image of the used CuBTC MOF sample with 120 min exposure time.

4.4.4.3 Effect of the degassing conditions of CuBTC MOF on the water vapour adsorption behaviour

CuBTC is a hydrophilic MOF that rapidly adsorbs the ambient moisture on its unsaturated copper sites. It was reported in the literature that the degree of hydration of CuBTC MOF influenced the adsorption of CO_2, where the CO_2 uptake increased significantly upon the presence of coordinated water molecules to the OMSs in the framework [49]. They attributed the enhancement in CO_2 uptake to the increase in the electrostatic interactions by a factor of 2.1–4. Here, the electrostatic interactions arise from interactions of the quadruple moment of CO_2 with the adsorbent's electric field that is increased by the addition of water molecules [49]. Hence, the degree of hydration of CuBTC MOF may also affect the overall uptake of water vapour molecules.

Generally, before the adsorption experiment, degassing of materials is commonly used to activate the material using the nitrogen purge, elevated temperature and/or vacuum. Therefore, different degassing conditions were investigated in this work to understand their effect on the water vapour adsorption behaviour of the resulting CuBTC MOFs.

Three samples of CuBTC MOF were degassed at different conditions prior to the water vapour adsorption measurements (with 6 h exposure time per vapour pressure stage and 25 ºC measurement temperature), *i.e.* (i) 6 h at 25 ºC under nitrogen purge, (ii) 10 h at 25 ºC under nitrogen purge and (iii) 4 h at 150 ºC under vacuum. The degassing steps were meant to remove the pre-existing water molecules in the framework. Natural drying process with forced convection was expected for the materials exposed to dry nitrogen at room temperature with extended contact hours, whereas, high temperature of 150 ºC and vacuum provided a severer condition to force the desorption of water molecules from the framework, and hence produced 'completely' dry sample. Figure 4.16 shows the measured water vapour adsorption isotherms of the CuBTC MOF samples from different degassing steps.

Figure 4.16 shows that the hydrated structure (degassed under 6) could reach equilibrium faster than the structure degassed using 10 h nitrogen purge and the dry CuBTC degassed under high temperature and vacuum (for example, *ca.* 33, 29 and 27 mmol/g, respectively at 28 mbar), where the last two structures need more time to reach equilibrium. For further exploration into this point, the collected isotherms in this work were compared to a completely equilibrated isotherm reported by Schoenecker *et al.* [128]. Schoenecker *et al.* performed water vapour adsorption on CuBTC MOF using a maximum exposure time of 24 h per point after degassing at 150 ºC (longer exposure time of >6 h could not be used in current work due to an experimental set-up limitation). The tedious experiment with long exposure time carried out by Schoenecker *et al.* [128] was believed to be sufficient to reach the water vapour adsorption equilibrium on CuBTC MOF, and the relevant isotherm is shown in Figure 4.16 (red solid circles). It can be seen from Figure 4.16 that using of less strict degassing conditions (*i.e.* 6 h of nitrogen purge) resulted in an equilibrated isotherm that is comparable to the isotherm reported by

Schoenecker *et al.* [128], which can also be attributed to the increase in water-water interactions.

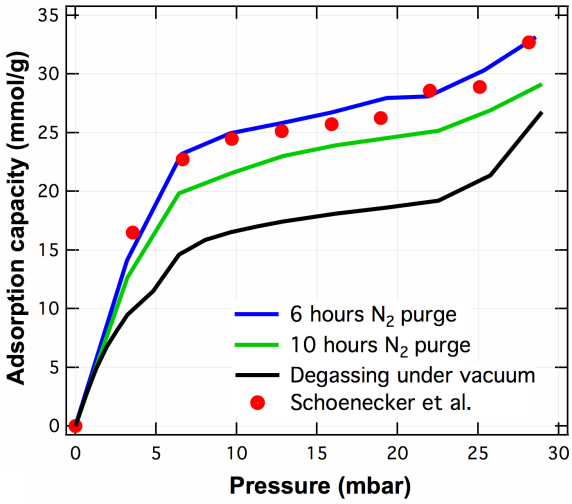

Figure 4.16. Water vapour adsorption isotherms (at 25 ºC) of CuBTC MOF from different degassing conditions compared to experimental data reported by Schoenecker *et al.* [128]. The adsorption isotherm of the sample degassed under vacuum was collected using the DVS vacuum instrument in the Surface Measurements Systems Ltd. laboratory.

On the other hand, seemingly the degree of hydration of CuBTC MOF had no effect on the equilibrium of water vapour adsorption at low vapour partial pressure regime of ≤1.5 mbar, where all isotherms showed the same trend, Figure 4.16. However, at higher vapour pressures (*i.e.* >1.5 mbar), it was found that the equilibrium adsorption of water vapour on CuBTC MOF could be significantly affected by the degassing conditions (or materials pre-treatment steps). This behaviour can be attributed to the interaction energies between water-water and water-CuBTC. Where, at low vapour pressure regime, the guest-guest (g-g, water-water) interactions are less dominant than the guest-host (g-h, water-CuBTC) interactions with a contribution of only 5% of the total energy of interactions at 1.5 mbar [121, 136]. However, as the vapour pressure of water increased, the g-h interactions diminished, whereas the contribution of g-g interactions to the total energy increased to >72% [136]. Therefore, the application of the normal degassing condition (N_2 purge) could result in partially hydrated CuBTC MOF, and hence enhance the adsorption of water molecules under humid conditions, especially in the high pressure regime as shown in Figure 4.16 where the water-water interaction is dominant.

Therefore, it is evident from the data above that the pre-absorbed/adsorbed water molecules in the structure of CuBTC MOF are helping in enhancing the adsorption of water molecules to quickly reach equilibrium. Hence, the hydrated CuBTC MOF structure possessed fast kinetics in comparison to the dry equivalent.

4.5 *Conclusions*

Characterisation of porous materials using water vapour adsorption is a valuable tool to identify their hydrothermal stabilities that dictate their final applications. This work reports an evaluation of the CuBTC MOF's capability to withstand the water vapour content. Here, temperature, relative humidity and vapour partial pressure were found to be critical parameters determining the stability of the CuBTC MOF under humid conditions. The underlying mechanism of the decomposition of CuBTC MOF upon the exposure to humid flow was investigated. In addition, detailed characterisations of samples used for dynamic water vapour adsorption using PXRD, SEM, SAXS, FTIR and DSC were given.

Partial structure degradation of CuBTC MOF was deduced at room temperature (25 °C) using dynamic vapour adsorption experiments. However, irreversible decomposition of CuBTC framework was observed at a temperature range of 40−50 °C. Such decompositions, partially or completely, of the structure of CuBTC MOF was found to be caused by the displacement of the organic linkers from the copper centres by the aggregated water molecules.

Materials modification may not be the only option for enabling the application of hydrophilic MOFs. The water adsorption behaviours of hydrophilic MOFs can be explored to design appropriate operating conditions to suit them in specific applications. In this work, the non-equilibrium adsorption (with respect to water adsorption) was designed to study the hydrothermal stability of CuBTC MOF for carbon capture from natural and flue gases under cyclic operations. It was found that the non-equilibrium adsorption process using CuBTC MOF was a suitable solution for CO_2 capture from natural gas, in which CuBTC MOF showed satisfactory tolerance to the presence of water vapour (up to 6 mbar) and no significant signs of decomposition for up to 48 h. For the high water vapour content

in the flue gas (up to 70 mbar), the fast swing operation (15 min per pressure stage) was necessary to maintain a stable framework to avoid the equilibrium adsorption of water vapour on CuBTC, as well as the structural degradation at room temperature. However, at flue gas emission temperature of 50 °C, the structure of CuBTC MOF showed signs of partial decomposition compared to complete decomposition when equilibrium adsorption was performed.

This Chapter also showed the impact of materials pre-treatment step on the water vapour adsorption on CuBTC MOF. It was found that starting with less dried CuBTC MOF sample resulted in reaching the equilibrium adsorption faster than the dry structure (*i.e.* fast kinetics). Here, the pre-adsorbed/absorbed water molecules served as nucleating sites helping to adsorb more water molecules from the feed stream.

In summary, dynamic water vapour adsorption is an important technique for characterising porous materials as well as exploring the operation window for their applications. It can provide a fair assessment of the hydrothermal stability of materials to allow the design and/or selection of appropriate processes to suit the intrinsic properties of materials.

Chapter 5

A Facile Post-Synthetic Modification Method to Improve Hydrothermal Stability and CO_2 Selectivity of CuBTC Metal Organic Framework

This Chapter contains the content of a published peer-reviewed article in the Industrial & Engineering Chemistry Research (55 (2016) 7941 DOI: 10.1021/acs.iecr.5b04217). It focuses on the development of a hydrothermally stable form of CuBTC MOF in the presence of water vapour for CO_2 capture applications. CuBTC MOF has high affinity to water molecules due to the presence of unsaturated metal sites that are ready to attract water molecules covalently. A straightforward solution to tackle this problem is to saturate the OMSs in the framework of MOFs.

A simple post-synthetic modification method for synthesis of molecular glycine-doped CuBTC MOF was developed in this work. The resulting materials, *i.e.* Gly-CuBTC MOFs, were characterised using various characterisation techniques and evaluated using single-component gas (CO_2 and N_2) adsorption in addition to dynamic water vapour adsorption experiments. The economical dopant of molecular glycine with the amine and carboxyl group was found to be able to saturate the OMSs in the parent CuBTC MOF leading to the improved hydrothermal stability as well as CO_2:N_2 selectivity by 15% at 50 ºC. It was also found that the adsorption capacity, CO_2:N_2 selectivity and hydrothermal stability of Gly-CuBTC MOFs depend on the percentage of saturation of the OMSs in the parent MOF.

5.1 *Introduction*

Open metals sites (OMSs) in certain MOFs, *e.g.* unsaturated copper centres in CuBTC MOF, are believed to be the attractive features for attracting small gas molecules [154-157], especially polar molecules such as water. Considering the practical application of MOFs with OMSs, the presence of water or humidity is inevitable, such as the post-combustion carbon capture from flue gases, where (5–7) vol.% water vapour is present [40].

CuBTC MOF is one of the most studied MOFs with OMSs [47, 49, 98, 105, 106, 118, 123, 158] since its discovery at the end of the 20th century [19]. CuBTC MOF is very sensitive to moisture, and the water-CuBTC interactions have been investigated in simulation [131, 132, 134] and experimental studies [116, 124, 125, 128-130]. The poor hydrothermal stability of CuBTC MOF has been proven to be linked directly to the vulnerability of OMSs in the framework to water molecules. The strong water affinity for OMSs results in the aggregation of water molecules near them under continuous hydration and can lead to the displacement of BTC ligands from OMSs [114, 133]. Various approaches have been developed to modify the structure of CuBTC MOF for selective gas adsorption and catalysis mainly by ligand functionalisation [80, 81, 159-162]. For example, Cai *et al.* [159, 160] demonstrated the possibility of using alkyl-functionalised BTC to construct CuBTC MOF derivatives. In comparison with the unfunctionalised CuBTC MOF, the alkyl-functionalised derivatives showed comparable uptakes of CO_2 and CH_4 at pressures of up to 5 bar and significantly lower water adsorption due to the hydrophobic functional groups. Another effective method of coating MOFs using hydrophobic polydimethysiloxane (PDMS) was also suggested [163]. This approach involved the chemical vapour deposition of a hydrophobic silicon layer over the surface of MOFs (*e.g.* CuBTC) at 235 ºC to enhance their moisture resistance. Though these approaches demonstrated the effectiveness toward improving the moisture stability of functionalised materials, they either involve tedious synthetic procedures for functionalising ligands or complex apparatus and harsh conditions for materials modification hindering their practical application.

Post-synthetic modification (PSM) of MOFs, on the other hand, is an attractive approach for facile functionalisation of MOFs [82, 83, 164, 165]. Luo *et al.* [83] developed a PSM method to graft the OMSs in CuBTC MOFs using an amino-functionalised basic ionic liquid (ABIL-OH) for enhancing the selectivity in liquid-phase catalytic Knoevenagel condensation reactions. In order to improve the CO_2 adsorption capacity and selectivity (over nitrogen) of materials, PSM methods were also used to modify relevant MOFs, *e.g.* functionalisation of Cu-BTTri with ethylenediamine [82] and of Mg_2(dobdc) with tetraethylenepentamine [165].

In this regard, PSM might be an effective method to solve the major drawback of poor hydrothermal stability for MOFs with OMSs. In this Chapter, a facile PSM method to prepare molecular glycine grafted CuBTC MOFs has been reported aiming at (*i*) hindering the water adsorption on OMSs (to improve hydrothermal stability) and (*ii*) enhancing the interaction with CO_2 (selectivity of CO_2 over N_2). The rationales behind the choice of molecular glycine as the dopant are (*i*) the dimension of glycine molecules (*i.e.* length ≈ 4.4 Å and width ≈ 3.2 Å) allowing the diffusion of glycine molecules into the CuBTC framework and (*ii*) the amine and carboxyl group in glycine allowing the interaction with both OMSs (*i.e.* unsaturated copper centres) and CO_2 molecules, respectively.

5.2 *Experimental section*

5.2.1 Materials and Synthesis

Copper (II) nitrate trihydrate [$Cu(NO_3)_2.3H_2O$, 99%], benzene-1,3,5 tricarboxylic acid (BTC, 95%) and amino acetic acid (glycine, ≥ 99%) were purchased from Sigma Aldrich and ethanol (absolute) was obtained from Fisher. All materials were used as received without further purification. CuBTC MOF was prepared using the improved hydrothermal method at 100 ºC for 24 h as described in Chapter 3. Glycine grafted CuBTC MOF (denoted as Gly-CuBTC) was prepared using a facile PSM method. Glycine crystals were fully crushed then dissolved in ethanol at 50 °C to give molecular glycine in solutions. The amount of glycine molecules was determined by the relevant percentage by weight (wt.%, glycine:Cu in CuBTC). CuBTC MOF was then added to the molecular glycine solution in ethanol. The

mixture was left to stir for 24 h at 50 °C, then washed with 60 cm^3 of ethanol and activated at 120 °C under vacuum for 16 h. Three Gly-CuBTC MOF samples were synthesised with 10 wt.%, 20 wt.% and 28 wt.% loading of molecular glycine in the parent CuBTC MOF. It was assumed that one molecule of glycine can occupy one copper atom. OMSs in 28 wt. % Gly-CuBTC were believed to be fully saturated by glycine molecules (the theoretical mass fraction of copper in the CuBTC MOF is 31.5% [139]). Accordingly, Gly-CuBTC MOFs containing 20 and 10 wt. % of glycine correspond to materials with 71% and 36% of Cu OMSs covered by glycine molecules. Details of the calculation are available in Appendix A.6.

5.2.2 Characterisation of materials

Powder X-ray diffraction (PXRD), scanning electron microscopy (SEM) analysis, thermogravimetric analysis (TGA-DTA), FTIR analysis, nitrogen adsorption and desorption isotherms at −196 °C, pure CO_2 and N_2 adsorption and dynamic vapour adsorption were performed according to the procedure given in Chapter 3 and 4.

Raman analyses were carried out using JY Horiba LabRam 300 Confocal Raman microscope. A 632.82 nm HeNe laser was used as the excitation source. The acquisition time of 100 s and 3 accumulations were used per run. The collection optics was set at 100x with 1% laser power (Full laser power = 10 mW). It is worth to note that the sample was damaged when 10% laser power was used, which is the next available laser power (after 1%).

5.3 *Results and discussion*

5.3.1 Characterisation of Gly-CuBTC MOF

Gly-CuBTC MOF was synthesised using a facile PSM method. Gly-CuBTC MOFs containing 28 wt.%, 20 wt.% and 10 wt.% of glycine were prepared, which correspond to materials with 100%, 71% and 36% of the Cu atoms coordinated to glycine molecules.

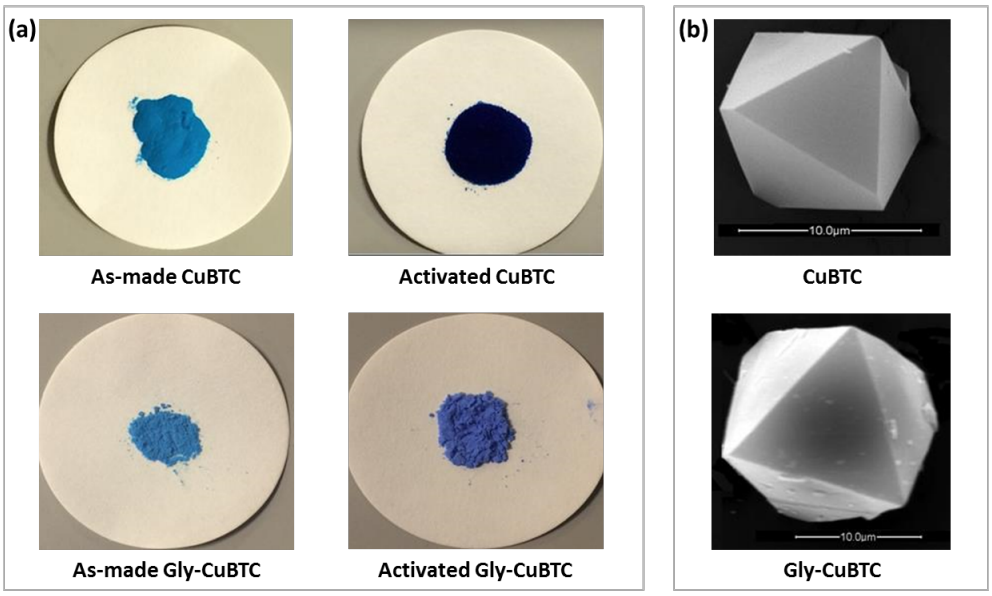

Figure 5.1. (a) The as-made and activated CuBTC and Gly-CuBTC MOFs samples; (b) SEM images of the CuBTC MOF crystal and Gly-CuBTC MOF crystal.

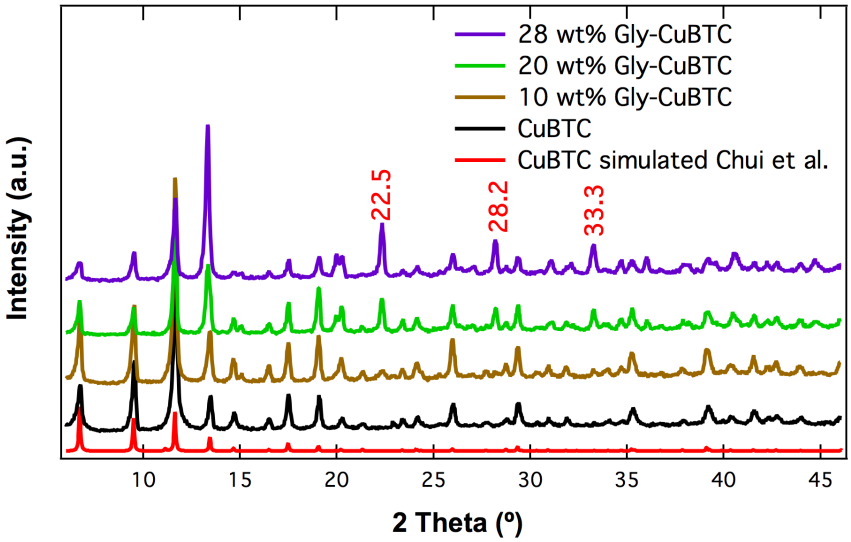

Figure 5.2. PXRD patterns of CuBTC MOF and Gly-CuBTC MOFs (10, 20 and 28 wt.% loading) in comparison to the simulated pattern adapted from reference [19].

The as-made Gly-CuBTC MOF (Figure 5.1a) exhibits a sky blue colour while the activated Gly-CuBTC MOF renders a royal blue colour differentiating them from the corresponding CuBTC MOFs samples. By comparing the PXRD patterns of Gly-CuBTC and parent CuBTC MOFs (Figure 5.2), the characteristic peaks (*i.e.* at 2θ ≈ 6.5°, 9.5°, 11.5° and 13.4°) of CuBTC MOF, as discussed in Chapter 3, are clearly identifiable in the PXRD patterns of Gly-CuBTC MOFs. These results suggest the retention of the parent framework structure of CuBTC MOF and its

crystallinity after the grafting process. In addition, the 2θ peaks positions of 22.5°, 28.2° and 33.3° are related to the peak diffraction intensity of pure glycine, which confirmed the incorporation of glycine molecules into the CuBTC framework. The intensities of these peaks were found to vary in relation to the doped amount of molecular glycine. SEM analyses also revealed that the size and morphology of the Gly-CuBTC MOF crystals were quite similar to that of the CuBTC MOF (Figure 5.1b).

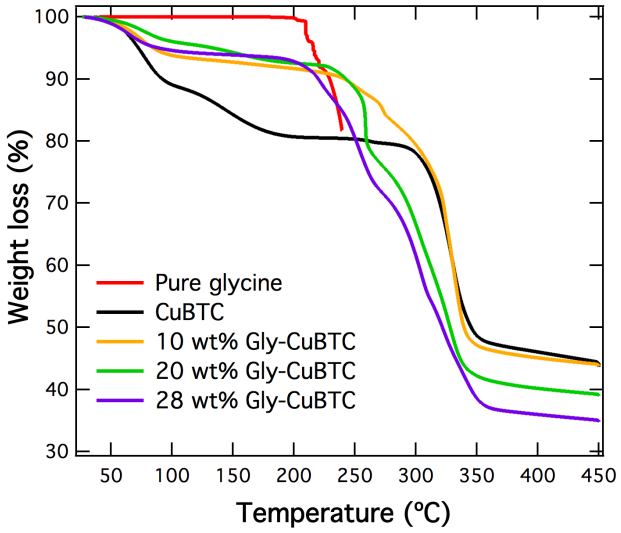

Figure 5.3. TGA curves of CuBTC MOF and Gly-CuBTC MOFs (10, 20 and 28 wt.% loading).

The thermal stability of Gly-CuBTC MOFs compared to CuBTC MOF and pure glycine were evaluated by TGA analysis (Figure 5.3). At temperature range of <220 °C, a weight loss in a N_2 atmosphere was observed for the Gly-CuBTC MOF samples, which can be attributed to the thermo-desorption of the absorbed/adsorbed water from atmosphere or solvent molecules that couldn't be fully removed during the activation process. The weight loss was lower than that of CuBTC MOF as an indication of the less hydrophilicity of the glycine modified structures. At a temperature range of >220 °C, different decomposition patterns were observed for the Gly-CuBTC MOF samples depending on the amount of glycine loaded. The more the glycine loaded in the samples, the earlier the degradation pattern recorded as a result of glycine decomposition inside the structure. Differential thermogravimetric analysis of Gly-CuBTC MOFs and CuBTC MOF showed that the decompositions of Gly-CuBTC MOFs occurred at

temperatures 220 °C, 258 °C and 270 °C for the 28%, 20% and 10% loadings, respectively, whereas the CuBTC MOF fully degraded at 310 °C.

Even though the thermal stability of Gly-CuBTC MOFs was reduced to lower than that of CuBTC MOF, it is still high enough to be used for industrial applications such as CO_2 capture from flue gases (emission temperature = 50–75 °C).

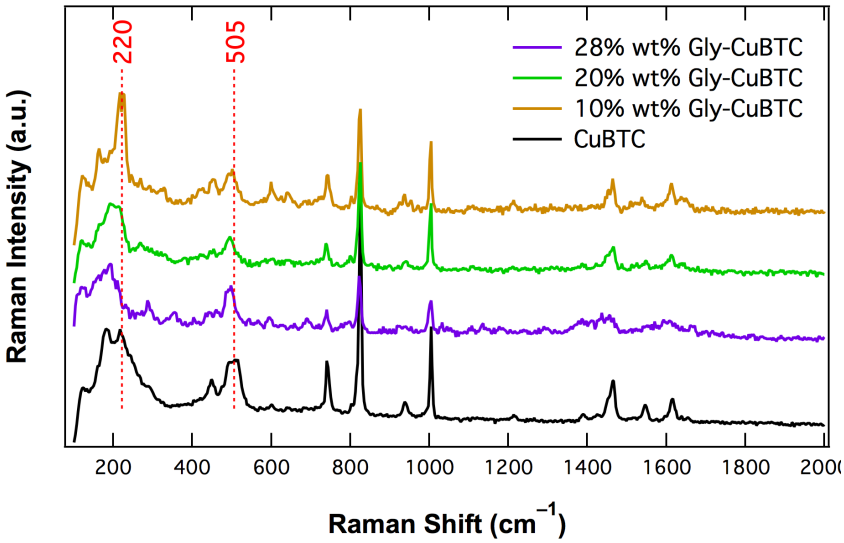

Figure 5.4. Raman spectra of CuBTC MOF and Gly-CuBTC MOFs (10, 20 and 28 wt.% loading).

The structural vibration of Gly-CuBTC MOFs, CuBTC MOF and pure glycine were investigated using Raman spectroscopy (Figure 5.4) and FTIR spectroscopy (Figure 5.5). The peaks' assignments of pure CuBTC MOF of Raman spectra have been established from a previous work reported by Dhumal *et al.* [166]. The associated vibrational bands associated with Cu bonding in CuBTC MOF appear in the wavelength range of less than 600 cm^{-1}. A band related to Cu–Cu stretching mode was observed in the parent CuBTC MOF spectra at 220 cm^{-1}. According to Dhumal *et al.* [166], the Cu–Cu stretching peak would be observed at 228 cm^{-1} for the fully degassed CuBTC MOF, however, the partial hydration caused by analysing the sample at atmospheric conditions resulted in a gentle frequency shifting to a lower value. The Gly-CuBTC MOF spectra showed a further shift in the frequency associated with Cu-Cu interaction as a result of glycine tying to the copper atom in CuBTC MOF. Such shift to a lower wavelength can be attributed to the elongation of the Cu–Cu bond that needs less energy in order to be stretched.

Another band associated with Cu–O stretching were observed at 505 cm^{-1} in the parent CuBTC MOF. This peak is also shifted to a lower wavelength in the Gly-CuBTC MOF spectra, in which, the Cu–Cu bond elongation and weakening can also explain this shift.

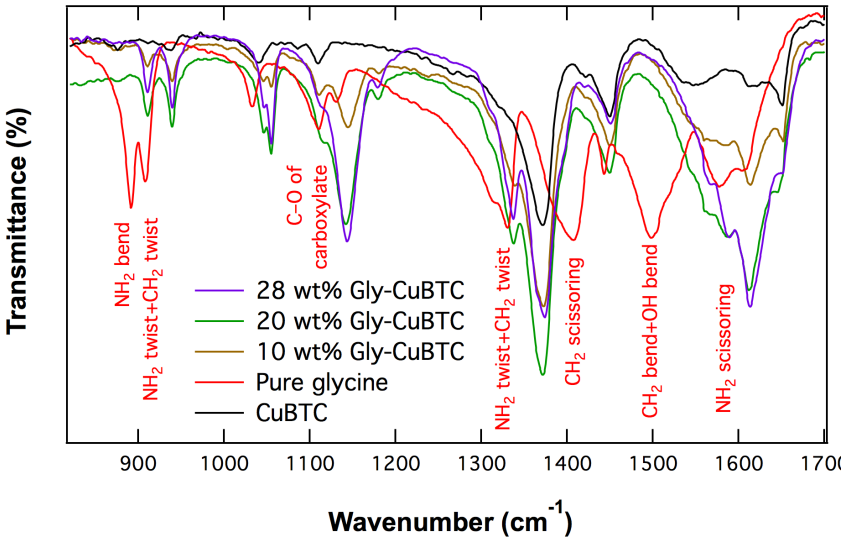

Figure 5.5. FTIR spectra of CuBTC MOF, Gly-CuBTC MOFs and pure glycine. The assignments of peaks for glycine FTIR spectrum has been adapted from the literature [167].

FTIR analysis (Figure 5.5) showed that Gly-CuBTC MOF samples preserve the vibrational properties of both parent CuBTC MOF and pure glycine. The characteristic bands of CuBTC MOF at 1645, 1445 and 1375 cm^{-1} are still evident in Gly-CuBTC MOF samples confirming the results from PXRD analyses. Such results suggest that the coordination in $Cu_2C_4O_8$ cages of the CuBTC framework is intact after the PSM modification using molecular glycine. By comparing the FTIR spectra of glycine and Gly-CuBTC MOFs, no band shift is noticed for the C–O stretch at *ca.* 1110 cm^{-1} in the carboxylic group of glycine molecules. However, the characteristic bands corresponding to NH_2 moiety were found shifted to higher wavelengths in the spectra of Gly-CuBTC MOF samples. Such shifts can be ascribed to the coordination of glycine molecules to the copper centres of parent CuBTC MOF through the nitrogen atom in glycine.

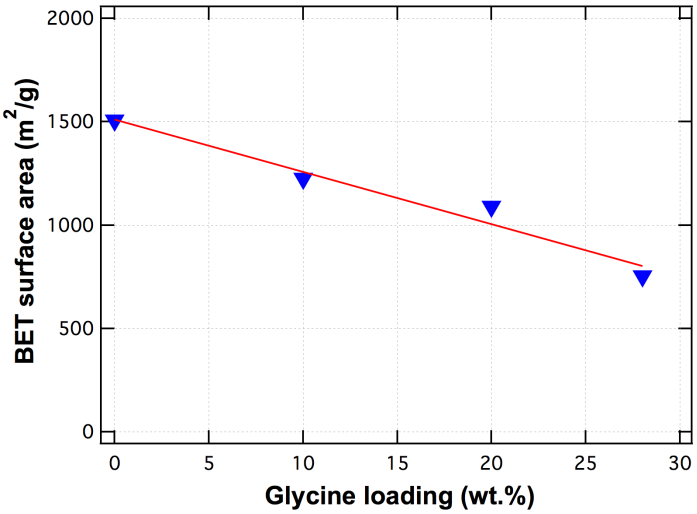

Figure 5.6. BET surface areas of CuBTC MOF and Gly-CuBTC MOFs.

Nitrogen adsorption at −196 °C was used to evaluate the effect of the PSM modification using molecular glycine on the BET surface area of materials. As it can be seen from Figure 5.6, the grafting of CuBTC MOF using molecular glycine resulted in a reduction of the BET surface area of Gly-CuBTC MOFs. In general, the BET surface area of Gly-CuBTC MOFs decreased in a linear fashion with increasing the loading amount of molecular glycine. Such phenomenon can be expected since the alien glycine molecules can diffuse into the porous structure of parent CuBTC MOF and attach to the copper centres reducing the available pore volume and surface area of Gly-CuBTC MOFs.

5.3.2 CO_2 and N_2 adsorption on Gly-CuBTC MOFs

Gly-CuBTC MOFs were evaluated using pure CO_2 and N_2 adsorption experiments and the isotherms (at 25 °C and 50 °C) for Gly-CuBTC MOF samples are shown in Figure 5.7. For both probing gases, the adsorption temperature showed a negative effect on the adsorption capacity of Gly-CuBTC MOF, *e.g.* CO_2 uptake of the 28 wt.% Gly-CuBTC MOF decreased by *ca.* 45% by increasing the temperature from 25 °C to 50 °C at 1 bar, indicating the physisorption of probing molecules on Gly-CuBTC framework. The CO_2 adsorption capacities of Gly-CuBTC MOFs (at 1 bar) were found to decrease with increasing the amount of molecular glycine, as shown in Figure 5.7 and Table 5.1. This behaviour can be attributed to the occupation of the available pore volume in the framework by glycine molecules resulting in

decreasing of BET surface area and accordingly reduces adsorption capacity of Gly-CuBTC MOFs.

Table 5.1

Calculated BET surface areas of Gly-CuBTC MOFs from N_2 adsorption at –196 °C and measured adsorption capacity of pure CO_2 and N_2 adsorption on Gly-CuBTC MOFs at 1 bar.

	BET surface area (m^2/g)	Temperature (°C)	CO_2 adsorption capacity (mmol/g)	CO_2 adsorption capacity (molecule/UC)	% Reduction in adsorption capacity/UC
Parent CuBTC	1507±26	25	4.45	43.07	
		50	2.45	23.71	
10 wt.% Gly-CuBTC	1225±57	25	3.25	35.60	17.34
		50	1.06	11.61	51.03
20 wt.% Gly-CuBTC	1090±55	25	2.42	29.59	31.29
		50	0.967	11.82	50.13
28 wt.% Gly-CuBTC	753±21	25	2.20	29.21	32.17
		50	0.450	5.975	74.80

At 25 °C and 1 bar, the measured CO_2 adsorption capacity of 28 wt.% Gly-CuBTC MOF was about 2.2 mmol/g which is comparable to that of a polydimethysiloxane (PDMS) coated CuBTC MOF [163] (red solid line in Figure 5.7). By coating the CuBTC MOF using the hydrophobic PDMS [163], all available OMSs in the parent MOF were expected to be protected by the PDMS. For 28 wt.% Gly-CuBTC MOF, a similar scenario was anticipated with all OMSs in CuBTC MOF occupied by molecular glycine. Therefore, a comparable saturating CO_2 adsorption capacity was predicted for both materials. However, the measured BET surface area of Gly-CuBTC MOF was much lower than the one of PDMS coated CuBTC MOF (<800 *versus* 1544 m^2/g) [163]. Therefore, the adsorption capacity per unit cell of solid was calculated, (Table 5.1), to show the effect of excluded volume by the align glycine molecules on the available area inside the pores. Here, the reduction percentage of CO_2 adsorption capacity on Gly-CuBTC MOF reached up to *ca.* 75% compared to that of parent CuBTC MOF. It is worth to note that the adsorption of CO_2 and N_2 on Gly-CuBTC MOFs are fully reversible and no hysteresis loops were found between adsorption and desorption isotherms.

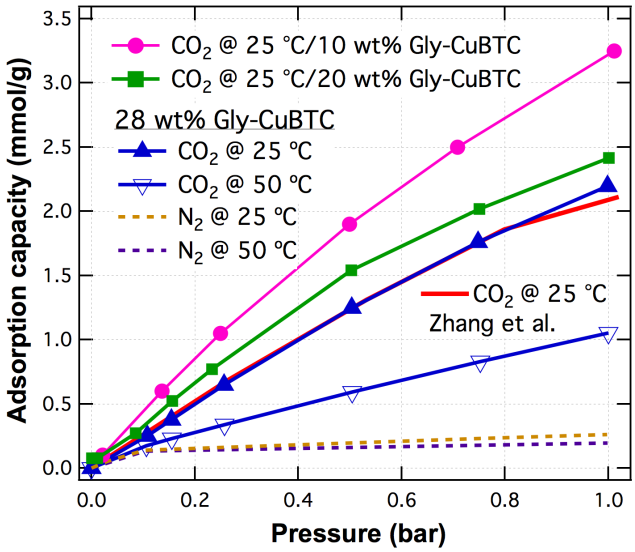

Figure 5.7. Pure CO_2 and N_2 adsorption isotherms on Gly-CuBTC MOFs compared to coated CuBTC MOF reported by Zhang *et al.* [163].

Considering the practical application of MOFs for CO_2 capture from flue gases, where nitrogen is the largest constituent (70–75 vol.%), the CO_2:N_2 selectivity of materials is of particular interest for efficient removal. Based on the single-component adsorption data measured in this study, the Ideal Adsorbed Solution Theory (IAST) [109, 168] was employed to estimate the selectivity of developed materials in multicomponent adsorption equilibria. In comparison to the parent CuBTC MOF, the CO_2:N_2 selectivity (in a system with 1 bar total pressure and 15 vol.% CO_2 assuming the remaining gas is only nitrogen) was improved for the doped CuBTC MOF, *i.e.* 33 for Gly-CuBTC MOF *versus* 26 for CuBTC MOF at 25 °C and 19 for Gly-CuBTC MOF *versus* 16 for CuBTC MOF at 50 °C.

The improved CO_2:N_2 selectivity of the Gly-CuBTC MOF can be mainly attributed to the enhanced interactions with CO_2 molecules by the addition of polar glycine molecules [169] to CuBTC framework (electric quadruple moment: CO_2 = 13.4 $C.m^2$ *versus* N_2 = 4.72 $C.m^2$) [170]. Furthermore, the reduced pore volume of the Gly-CuBTC framework also has the beneficial effect on the selectivity to CO_2 due to the intensified adsorbate-adsorbent interactions in constricted pores [171].

5.3.3 Improved hydrothermal stability of Gly-CuBTC MOFs

The hydrothermal stability of synthesised Gly-CuBTC MOF was evaluated using dynamic water vapour adsorption experiments (experiments are reproducible with *ca.* 15% standard deviation on measured adsorbed amount of water vapour). Figure 5.8 shows a comparison of the adsorption isotherms and dynamic water vapour adsorption on the parent CuBTC MOF and modified 28 wt.% Gly-CuBTC MOF at 50 °C (simulating the flue gas emitting conditions). Where, after the PSM treatment of CuBTC MOF using molecular glycine, (*i*) the saturated water vapour adsorption capacity of materials was reduced by *ca.* 50% and (*ii*) the hydrothermal stability of materials has been improved significantly.

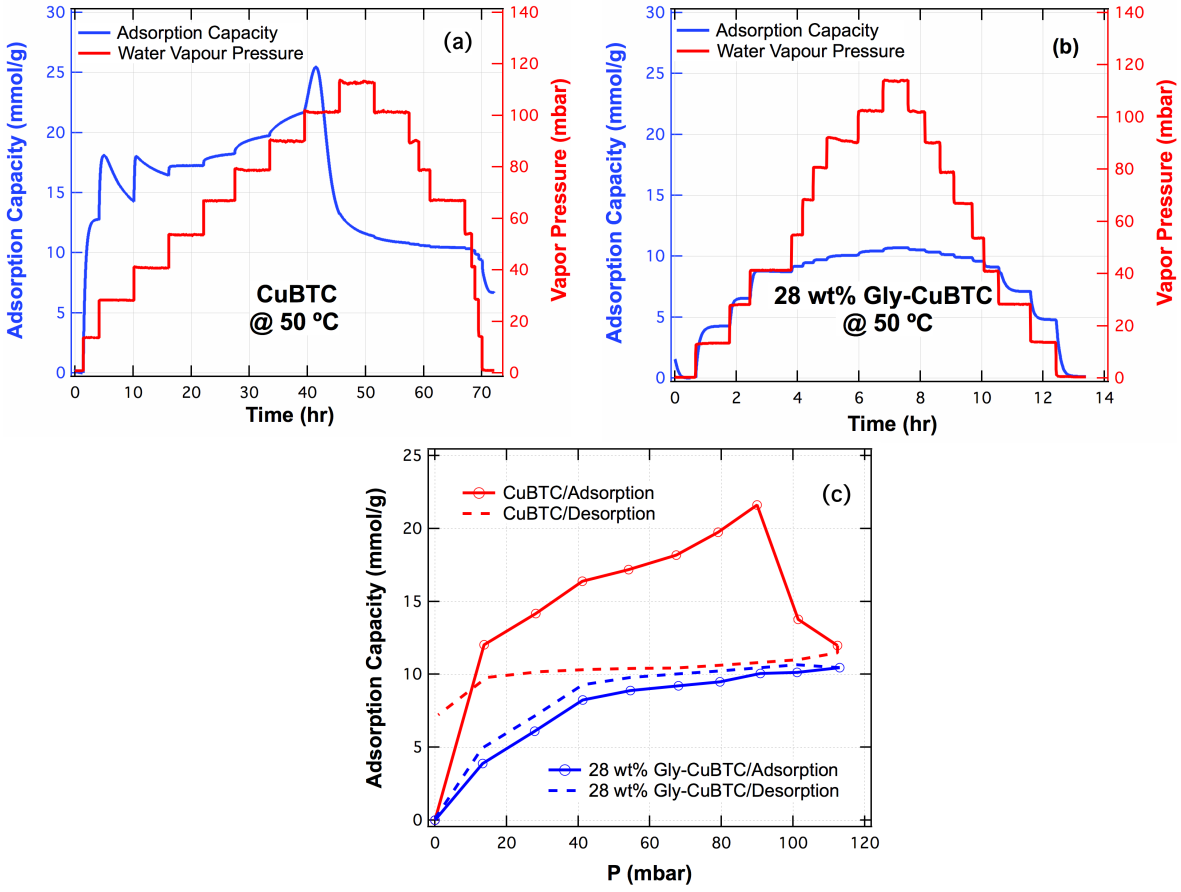

Figure 5.8. (a) Temporal water vapour adsorption on the CuBTC MOF at 50 °C, (b) Temporal water vapour adsorption on the 28 wt.% Gly-CuBTC MOF at 50 °C and (c) Adsorption isotherms of water vapour on CuBTC MOF and 28 wt.% Gly-CuBTC MOF at 50 °C.

For dynamic water vapour adsorption on CuBTC MOF (Figure 5.8a), unusual phenomena (*i.e.* two peaks showing the loss of adsorbed water molecules) were measured at partial water vapour pressures of *ca.* 24.7 and 37 mbar suggesting the possible partial decomposition of CuBTC framework during the water vapour adsorption process. At the partial water vapour pressure of 86 mbar, a sudden drop of the adsorption capacity of CuBTC MOF represented the complete collapse of CuBTC framework caused by the aggregation of water molecules in the parent framework and destroying the Cu-BTC coordination [134]. In contrast, the temporal data of water vapour adsorption on 28 wt.% Gly-CuBTC MOF demonstrated a stable material for one cycle of water vapour adsorption and desorption. Furthermore, a much shorter equilibrium time was required for the 28 wt.% Gly-CuBTC MOF than the CuBTC MOF in the experiments of dynamic water vapour adsorption demonstrating the high moisture/water resistance of Gly-CuBTC MOFs developed by the PSM treatment on the parent CuBTC MOF.

The 10 wt.% and 20 wt.% Gly-CuBTC MOFs were also evaluated using dynamic water vapour adsorption experiments at 25 and 50 °C, respectively, and the results are presented in Figure 5.9. The 10 wt.% and 20 wt.% Gly-CuBTC MOF samples demonstrated good moisture stability under humid streams at 25 °C (Figure 5.9a and c). However, temporal data of water vapour adsorption on them at 50 °C showed signs of the partial degradation of framework structures such as the anomalous peaks in adsorption and the decrease in desorption capacities lower than those of adsorption at same pressure points (Figure 5.9b and d).

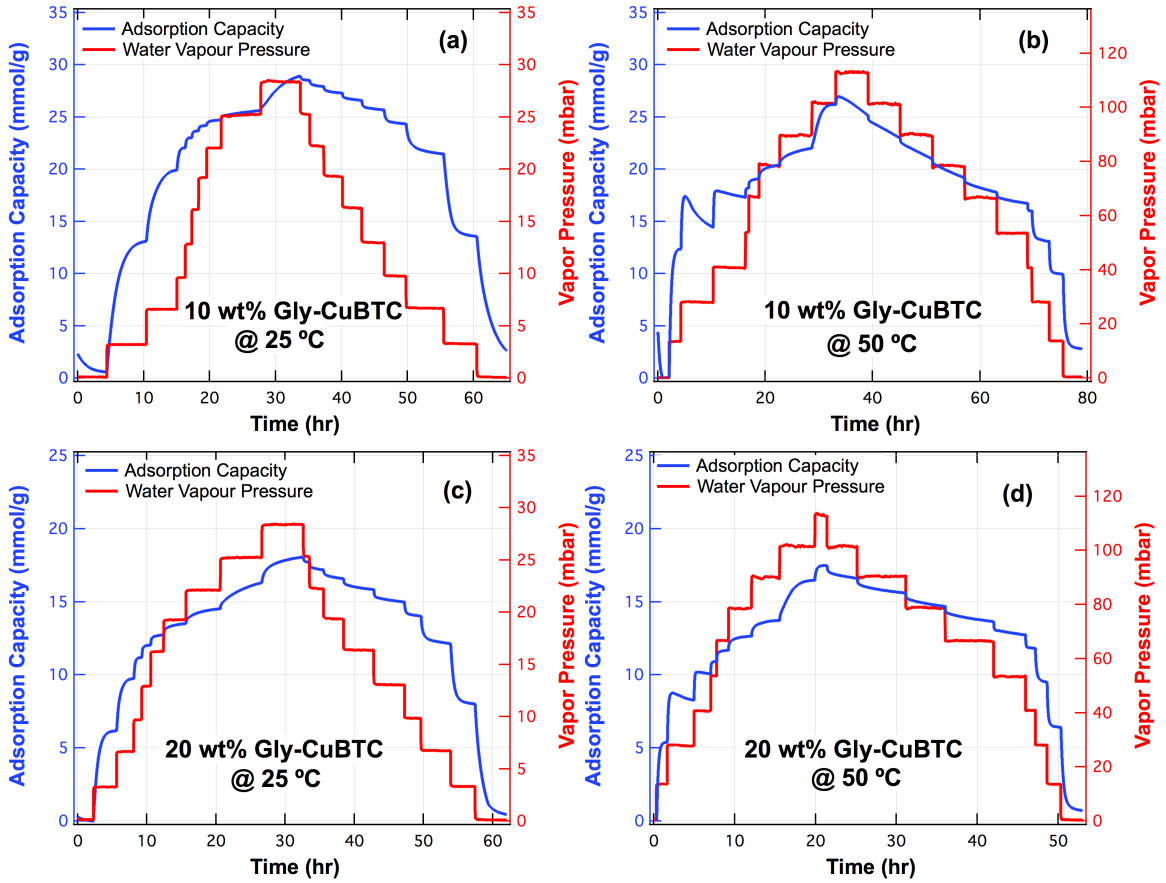

Figure 5.9. (a) and (b) Temporal water vapour adsorption on the 10 wt.% Gly-CuBTC MOF; (c) and (d) Temporal water vapour adsorption on the 20 wt.% Gly-CuBTC MOF.

The OMSs in the 10 wt.% and 20 wt.% Gly-CuBTC MOFs were not fully covered by molecular glycine, therefore, the unprotected OMSs are available to interact with water molecules during adsorption resulting in the displacement of BTC linkers from Cu centres [134] and hence the partial degradation of these materials. In contrast to CuBTC MOF (Figure 5.8b), complete structural decomposition was not observed in the experiments for the 10 wt.% and 20 wt.% Gly-CuBTC MOF samples because the protected copper centres (with glycine molecules) remained intact under humid streams. In summary, partial degradation of glycine modified CuBTC frameworks at 50 °C was inevitable if OMSs in the parent framework were not fully saturated by the dopant. Therefore, the results obtained from the dynamic water vapour adsorption on Gly-CuBTC MOFs suggest that all the OMSs in CuBTC MOF need to be protected by the molecular dopant in order to ensure the hydrothermal stability of materials in the presence of water or humidity at room or elevated temperatures.

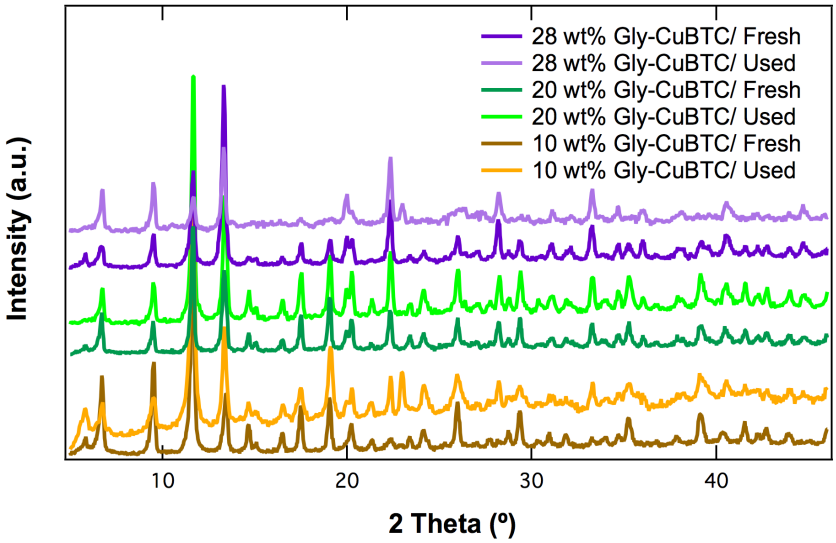

Figure 5.10. PXRD patterns of used Gly-CuBTC MOF samples for the water vapour adsorption at 50 °C in comparison to fresh ones.

PXRD analysis was carried out for fresh samples of Gly-CuBTC MOFs and used at 50 °C, as shown in Figure 5.10. It can be seen that all samples retained their intact crystalline structures after water vapour adsorption. However, as the amount of dopant glycine decreased (from 28 wt.% to 10 wt.%) the baseline of PXRD pattern start to have some disruption, indicating an amorphous diffraction as a result of partial structure decomposition. These results are in a good agreement with the dynamic water vapour adsorption/desorption data at 50 °C (Figure 5.9b and d).

5.4 *Conclusions*

This Chapter reports a simple and economical post-synthetic modification (PSM) method for the synthesis of glycine-doped CuBTC MOF, without using complex synthetic procedures and apparatus. The resulting glycine-doped CuBTC MOF, *i.e.* Gly-CuBTC MOF, was fully characterised by using PXRD, SEM, Raman spectroscopy, FTIR spectroscopy, TGA and N_2 adsorption. The molecular glycine was found to be able to saturate the open metal sites (OMSs) in the parent CuBTC framework leading to (*i*) diminished affinity of water vapour and (*ii*) enhanced interaction with CO_2 molecules.

Gly-CuBTC MOF was assessed using single component (*i.e.* CO_2, N_2 and water vapour) adsorption experiments. In comparison with the parent CuBTC MOF, the Gly-CuBTC MOF showed a diminished water vapour adsorption capacity (by *ca.* 57% at 50 °C and 90% RH) and an improved CO_2:N_2 selectivity (by *ca.* 15% at 50 °C, with 15 vol.% CO_2 composition). Furthermore, the developed Gly-CuBTC MOF was also stable under various humid conditions (up to 90% RH at 50 °C) demonstrating its suitability for practical applications.

These results present the development of a facile PSM method using an economical dopant (glycine), which could represent a cost-effective approach for preparing hydrothermal stable materials based on the available bulk MOFs for practical CO_2 capture from humid streams. Though only one parent MOF of CuBTC framework was investigated in this study, the method demonstrated here can be applied more generically to other MOFs with OMSs extending the fields of practical application of these materials, *e.g.* gas sorption and catalysis in the presence of water or humidity.

Chapter 6

Propagation of mass transfer zone in fixed bed columns: A case study of CO_2 capture using porous solid adsorbents

This Chapter presents an analysis of the effect of velocity variation along the fixed bed adsorption column on the absorbable gas equilibrium capacity and separation purity. A combined experimental and numerical study of CO_2/N_2 system using three different forms of adsorbents of amorphous powder (bulk activated carbon), crystalline powder (bulk copper benzene-1,3,5-tricarboxylate metal-organic framework, Cu-BTC MOF) and crystalline pellets (pelleted CuBTC MOF) was carried out to show the effect of the velocity variation on CO_2 breakthrough curves. Particularly, the variation of gas velocity due to adsorption was found to affect the breakthrough curves significantly, *i.e.* by more than 6% deviation for the CO_2/N_2 feed (0.2:0.8) unless a diluted feed of CO_2 concentration <1% is considered. This work shows that the deviation between the breakthrough time considering constant and variable velocity grows exponentially with the feed concentration of the adsorbable gas. Hence, it underestimates the calculated equilibrium adsorption capacity if a correction for the stoichiometric time is not considered.
Therefore, for a reliable evaluation of porous adsorbents for carbon capture based on the fixed bed adsorption analysis, one must consider the effect of velocity variation due to adsorption to make a fair judgment on predicting the performance of materials under flow conditions.

6.1 *Introduction*

Annually, worldwide carbon dioxide (CO_2) emissions, which are related with the energy sectors, increase at a rate *ca.* 2.1% [172]. This imposes a significant concern over the effort to combat the global warming. In order to achieve the goal of CO_2 abatement, various solutions have been proposed, such as the development of sustainable energy from renewable sources ones (*e.g.* biomass and solar) and carbon capture [173, 174]. CO_2 capture, especially for the post-capture technology, is a very promising option since it can be easily integrated with the current infrastructure of industries, providing the immediate solution to emissions control.

The current and most widely used method for CO_2 capture is the amine-based absorption, which suffers from intensive energy requirements for the solvent regeneration and equipment corrosion problems [40]. Adsorption-based separation processes using porous solids have been demonstrated as attractive alternatives due to their energy saving during regeneration compared to amine-based absorption processes. For example, in adsorption process, the heating of large amounts of water is not required during the regeneration step reducing the energy requirements [175]. Pressure swing adsorption (PSA) and temperature swing adsorption (TSA) have both been evaluated as feasible for large scale CO_2 capture [90]. In addition to the selection of the appropriate adsorption process, choosing the appropriate adsorbent with high CO_2 selectivity, adsorption capacity, good regenerability and stability under the process operating conditions, is another important factor for meeting the requirement of CO_2 separation [176].

The evaluation of the appropriateness of an adsorption process and the associated adsorbent is usually conducted experimentally complemented by mathematical modelling, to yield representative results for feedback to the design and optimisation of processes. Numerical simulations require careful analysis of the system, with careful attention to appropriate boundary conditions as well as simplifications. Models are useful tools to understand a process and explore wider operations windows than what is feasible to do experimentally, saving time and cost for process development and optimisation.

Upon the mathematical models' validation by sufficient experimental data, they are useful tools for the understanding the dynamic behaviour of fixed bed column as well as the optimisation of processes. They are commonly used to (*i*) explore the adsorption kinetics; (*ii*) understand the transport phenomena; (*iii*) estimate species distribution and temperature profiles along the fixed bed; and (*iv*) study the effect of process parameters (e.g. bed length, adsorption temperature, total gas flow rate and concentration of gases in the feed) on the performance of the bed, as shown in Table 1. They can be used to assess the temperature profile and breakthrough curves for a target gas in a mixture. Common assumptions, such as isothermal operation, negligible pressure drop/mass transfer effects and constant/variable velocity, are used to build the fixed bed model for simulating adsorption processes ensuring the adequate prediction of the process as well as the simplification of the mathematical analysis (Table 1). The choice of specific assumptions mainly depends on the computational effort needed to solve the problem and the accuracy of simulated results.

The propagation velocity is a parameter used to describe the propagation of mass transfer zone through the fixed bed column [177], which affects the prediction of breakthrough curves. Assumptions of both constant and variable velocity have been made in previous studies as shown in Table 1; however, there are no evident rationales to justify the selection of the assumptions. The propagation velocity is mainly a function of two parameters, *i.e.* the pressure drop across the column and the concentration change in the flow caused by the removal of an appreciable amount of adsorbable species from a concentrated feed [178]. In an early work, a fixed bed model with the consideration of velocity variations due to the pressure drop was developed and demonstrated as effective to improve the design of adsorption columns by 5–10% for diluted solutes [178]. Models assuming constant velocity has been used to describe CO_2 separation from mixtures (15–25% CO_2 in CO_2/N_2 mixtures), with <2–9.5% differences [179, 180] compared to the experimentally measured breakthrough curves. These deviations have been attributed to errors associated with the experimental procedure or model parameters estimation. From an objective point of view, the difference between the model and the measured data also likely arose from the model limitations such as

the variable velocity effect during the adsorption, which was neglected in the assumption of constant propagation velocity.

Despite the fact that model prediction errors of <10% may be acceptable for progressing the design, it may highly affect the operational CO_2 adsorption capacity of the process and the resulting purity of CO_2 that matters for industrial applications. The desired purity of CO_2 (x_{CO_2}) to be transported or sequestered needs to be more than 95% [27]. Theretofore, the variation of propagation velocity across the fixed bed column deserves a thorough investigation to understand the criteria of setting appropriate velocity assumptions for different scenarios.

In this study, the effect of propagation velocity on the breakthrough curves was studied both experimentally and numerically using a wide range of CO_2 composition in CO_2/N_2 mixture (0.5–80%). Fixed bed adsorption experiments were carried out using materials with different properties and working capacities, *i.e.* bulk activated carbon (AC), bulk CuBTC MOF (BTC = benzene-1,3,5-tricarboxylate) and pelleted CuBTC MOF, to show the effect of velocity variation caused by different adsorbents. Crystalline CuBTC MOFs were selected in this work because they are well-studied MOFs with good thermal stability (up to 310 °C) [181] and available commercially at scale [115]. CO_2 adsorption on the economical amorphous AC was used as the benchmark case to demonstrate the ability of using MOFs for practical CO_2 capture.

Table 6.1

Overview of selected modelling studies of carbon dioxide separation from gas mixtures using fixed bed arrangement.

Ref.	Assumptions	Comments
[46]	- bi-LDF approximation for diffusion in micro and macro pores -Variable velocity - Appreciation of mass, energy and momentum balances	- Layered Zeolite (0.8 mm)/carbon molecular sieve 3K (0.9 mm) - $CO_2/CH_4/N_2$ mixture (20% CO_2, 20% CH_4, 2.5 bar) - Effect of the ratio of adsorbent layers on the purification of methane from N_2 and CO_2 and continuous separation of CO_2 from N_2 was studied
[182]	- bi-LDF - Variable velocity - Appreciation of mass, energy and momentum balances	- AC (1.17 mm)/Zeolite (0.85 mm), staged column with 0.5 m AC bed and 0.5 m Zeolite bed - $CO_2/H_2/N_2/CH_4$/CO mixtures (7 bar) - Effect of the dual bed configuration on the process efficiency (*e.g.* purity) was studied
[183]	- Local equilibrium assumption - Isothermal condition - Negligible pressure drop - Variable velocity	- MOF-74, 177, NaX, CuBTTri, BeBTB, CoBDP - $CO_2/CH_4/H_2$ (20% CO_2, 0–60 bar) - Evaluation of MOFs and zeolite for gas adsorption in fixed bed - The effect of breakthrough time on the selectivity and working adsorption capacity was determined
[184]	- Linear driving force (LDF) - Non-adsorbable N_2 - Variable velocity	- Zeolite 13X pellets (1.03 mm) - CO_2/N_2 mixture (10% CO_2, 4–6.5 bar) - Breakthrough and heat effect of gas mixture were studied at various feed flow rates
[185]	- LDF - Variable velocity - Appreciation of mass, energy and momentum balances	- Zeolite 13X particles (1.6–2.6 mm) - CO_2/N_2 mixture (20–60% CO_2, 1 bar) - Empirical model combines linear and quadratic driving force was proposed - Heat transfer and mass transfer coefficients, breakthrough curves, temperature profile and mole fraction of CO_2 along bed were simulated

[186]	- LDF - Variable velocity - Appreciation of mass, energy and momentum balances	- CuBTC MOF pellets (13 mm) - $CO_2/CH_4/N_2$ (10 and 24% CO_2, 2–8 bar) - Effect of temperature on the equilibrium selectivity was studied - Mass transfer mechanism (molecular diffusion and external film resistance) was discussed. - Breakthrough curves for all gases with temperature profiles along the column were determined
[187]	- LDF - Variable velocity - Appreciation of mass, energy and momentum balances	- CuBTC MOF (1.5 mm) - $CO_2/H_2/CH_4/CO/N_2$ mixtures (18–28% CO_2, 2 bar) - 14 cycles of PSA adsorption and desorption were performed to study the performance of the adsorbent - Breakthrough curves for all gases with temperature profiles along the column were determined
[40]	- Isothermal condition - Local equilibrium assumption - Constant velocity	- Cr-MIL-101 - CO_2/N_2 (10% CO_2) - The effect of flue gas contamination (H_2O, NO and SO_2) on CO_2 adsorption capacity was studied - Flue gas contamination found to have minimal impact on CO_2 adsorption capacity
[188]	- Isothermal condition - LDF - Variable velocity - Negligible pressure drop	- Zr-based MOFs, Zeolite (0.85 mm) and 5A Calgon PCB (1.17 mm) - $CO_2/H_2/CH_4/CO/N_2$ mixtures (16% CO_2, 7 bar) - Layered bed of activated carbon and MOF was studied - Micropores/macropores ratio was compared to determine the dominating resistance
[179]	- Isothermal condition - Negligible pressure drop - Constant velocity - Non-adsorbable N_2 - Negligible effect of external mass transfer	- AC and modified-AC (d_p = 0.65 mm) - CO_2/N_2 mixture (15% CO_2, 1 bar) - Comparison of the breakthrough curves - Different kinetic models were compared and the effect of temperature and flow rate on the breakthrough profile was studied
[172]	- Isothermal condition - LDF - Constant velocity - Non-adsorbable N_2	- K based sorbent (0.25–0.4 mm) - $CO_2/N_2/H_2O$ mixtures (15% CO_2, 10% H_2O, 0–3 bar) - Several equilibrium models were compared - Influence of mass transfer steps on predicted breakthrough curves was discussed

6.2 *Experimental section*

6.2.1 Materials

Bulk activated carbon (DARCO®, *ca.* 150 μm) and glass beads (212–300 μm) were purchased from Sigma Aldrich. Bulk (1–2 μm) and pelleted (1 mm diameter and *ca.* 8 mm length) CuBTC MOFs were obtained from the MOF Technologies Ltd. All materials were used as received without further purification.

6.2.2 Characterisation

Several characterisation techniques were used to assess the properties of AC and CuBTC MOFs, such as powder X-ray diffraction (PXRD), scanning electron microscopy (SEM), surface area analysis and pure CO_2 and N_2 adsorption isotherms at 50 ºC using a gravimetric technique. Details of analyses apparatus and procedure can be found in Chapter 3.

6.2.3 Fixed bed adsorption apparatus and breakthrough measurements

The adsorption experiments and breakthrough curves were measured using the experimental rig shown in Figure 6.1a. The adsorption system was composed of a single fixed bed column, mass flow controllers and a micro gas chromatography (micro GC). In order to avoid the flow maldistribution caused by the bed settling, the fixed bed column was positioned vertically with the feed gas flowing downward through the bed [189]. The feed gas flow rates of CO_2, N_2 and helium (for dilution) were controlled by mass flow controllers (Alicat Scientific MC-series, ± 5% accuracy). The relative CO_2 feed composition was regulated by varying the flow rate of CO_2 and N_2. The flow rate of CO_2 was always kept at the lowest allowable value (5 cm^3/min) in order to avoid the fast saturation of adsorption bed by CO_2 and the collection of quality experimental data points.

The bed outlet stream was diluted with helium (He, 475 cm^3/min) before it was directed into the micro GC (Agilent Technologies 490 Micro GC) with a PoraPlot U (PPU) column and a thermal conductivity detector (TCD) for in-line analysis of outlet gases (micro GC analyses were performed every 1 min). Details of the calibration method of the Micro GC and calibration data of CO_2 and N_2 are given in Appendix A.7. The fixed bed column and the inlet piping were placed inside an

oven (Memmert) to ensure a global isothermal condition for the adsorption experiments. All experiments were carried out at a constant temperature of 50 °C (simulating the emission temperature of flue gases [1, 2]) and the packed materials were first activated overnight at 200 °C under vacuum. Then they were activated in *situ* at 100 °C under He (500 cm^3/min) for two hours prior to the adsorption measurements. The pressure drop across the fixed bed was measured using a mobile pressure meter (Comark C9557), as well as determined using the pressure reading from the mass flow controllers at inlet and outlet of the fixed bed column. Under the conditions used in this study, the pressure drop was found to be lower than 6×10^{-3} bar for all experiments. For each experiment in this work, fresh adsorbents were always used.

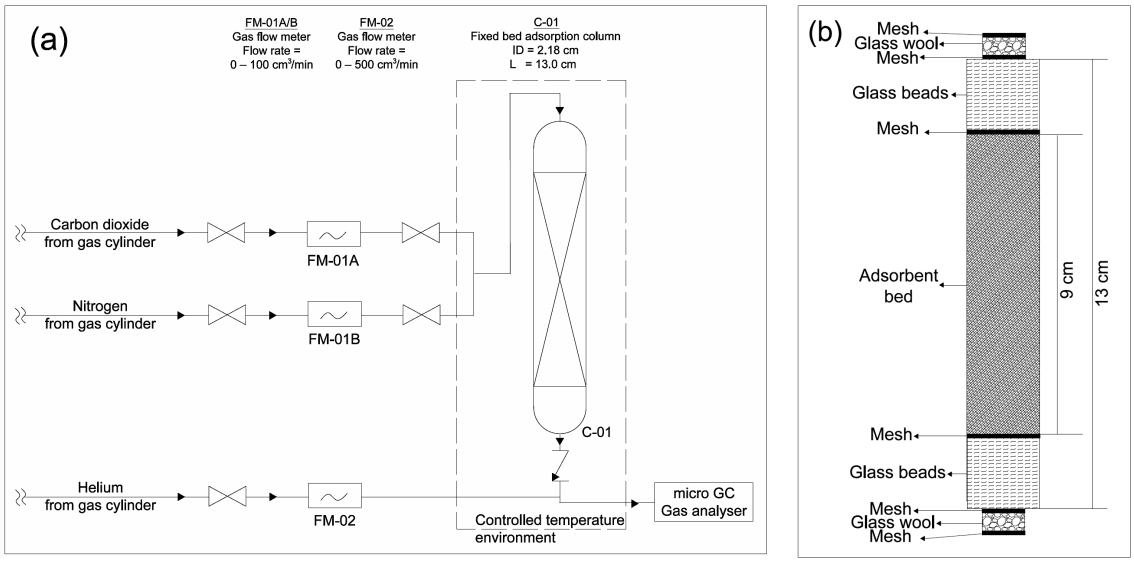

Figure 6.1. (a) Schematic diagram of the fixed bed adsorption system used in this work; (b) Details of the packed bed.

The adsorbent (13–15 g, no dilution) was packed in a stainless steel column (total length = 13 cm, internal diameter = 2.18 cm). The fixed bed was designed according to the empirical guidelines given below. In order to avoid the problems of channelling, radial dispersion and variation of fluid velocity across the bed, the ratio of bed diameter to particle diameter (*D*/*d*) needs to be greater than 20 [189, 190]. It was also suggested to increase the *D*/*d* ratio to a value of >100 to promote the intermixing of flow streams near the wall and in the central region [189]. In this work, the *D*/*d* ratios were estimated as *ca.* 145 for bulk AC and >10000 for bulk CuBTC MOF. For CuBTC MOF pellets, the ratio of *D/d* was about 22, where

higher ratios need bigger column and more sample. The properties of the fixed bed column are given in Table 6.2.

The configuration of the column is shown in Figure 6.1b, inert layers of glass beads were used to support the adsorbent bed in the column and they were separated from the adsorbent bed with fine meshes to prevent the mixing of glass beads with the adsorbent [189]. The inert regions could facilitate the flow distribution as well as act as a ballast to prevent the movement of adsorbents, and hence their attrition. The inert glass beads of (212–300 μm) sizes were used bigger than the size of adsorbent particles to avoid the high pressure drop [189]. Glass wool layers were placed at the inlet and outlet of the column to prevent the possible migration of the ballast through the inlet and outlet tubes. The bed void fraction was determined using the correlation reported by Walas [191], where the void fraction was given as a function of the particle to tube diameter depending on the morphology of particles.

Table 6.2
Properties of fixed bed column and input parameters.

Column length	13 cm
Bed length (*L*)	9 cm
Bed diameter (*D*)	2.18 cm
Temperature (*T*)	50 °C
Inlet pressure (P_0)	1–1.5 bar
Void fraction (ε)	0.31 for bulk AC and CuBTC MOF
	0.56 for CuBTC MOF pellets
Total flow rate (*F*)	10–100 cm^3/min

6.2.4 Theoretical aspects

A mathematical model that describes the dynamics of CO_2 adsorption in the fixed bed was developed based on the following assumptions; *(i)* ideal gas, *(ii)* isothermal condition across the bed, *(iii)* negligible N_2 adsorption compared to CO_2, and *(iv)* negligible radial and axial dispersion. The model was composed of a

series of equations (Eqs 6.1–5) [177] governing the physical phenomena of the adsorption process in the fixed bed.

Component mass balance:

$$\varepsilon \frac{\partial C_i}{\partial t} + \frac{\partial \left(uC_i\right)}{\partial z} + \left(1-\varepsilon\right)\rho_g \frac{\partial q_i}{\partial t} = 0 \tag{6.1}$$

Overall mass balance:

$$C\frac{\partial u}{\partial z} + \left(1-\varepsilon\right)\rho_g \sum_{i=1}^{n} \frac{\partial q_i}{\partial t} = 0 \tag{6.2}$$

Ergun equation for computing the pressure drop across the bed:

$$-\frac{\partial P}{\partial z} = 150\frac{\mu_g \left(1-\varepsilon\right)^2}{\varepsilon^3 d^2} + 1.75\frac{\left(1-\varepsilon\right)}{\varepsilon^3 d}\rho_g u^2 \tag{6.3}$$

The concentration of a specific component in the mixture (C_i) is given by:

$$C_i = \frac{y_i P}{RT} \tag{6.4}$$

The rate of adsorption can be described using different approximations: the local equilibrium (LQ) assumption (Eq 4) considers the negligible mass transfer resistance through the adsorbent particles, and the linear driving force (LDF) model (Eq 5) assumes that the adsorption rate is proportional to a linear gradient between the average amount adsorbed in the particle, and the amount adsorbed at the surface of the particle (in equilibrium with the bulk concentration).

$$\frac{\partial q_i}{\partial t} = \frac{\partial q_i^*}{\partial t} \tag{6.5}$$

$$\frac{\partial \overline{q}_i}{\partial t} = k_i\left(q_i^* - \overline{q}_i\right) \tag{6.6}$$

where k_i is the overall resistance to mass transfer, q_i^* is the adsorbed amount at equilibrium given by the adsorption isotherm $q_i^* = f\left(C,T\right)$, and $\overline{q}_i$ is the average adsorbed amount.

The boundary conditions for unused bed are: $t = 0$, $P = P_0$, $C_i(z, 0) = q_i(z, 0) = 0$. The model was coded in Matlab 8.3 (R2014a). Component and overall material balances were converted from the partial differential equation (PDE) into sets of ordinary differential equations (ODEs) by numericalising the derivative term with respect to the bed length. The resulting ODE system, which was subjected to initial boundary conditions of the breakthrough process, was integrated with respect to time using Matlab ODE15s solver. The integration was performed with dividing the bed into 40 equal length segments (z) with 1 s time step. A general flow sheet that represents the Matlab model solving steps is given in Appendix A.8.

An analytical solution developed by Bohart and Adams (denoted as B-A model, Eq 6.7) [192] was also used in this work to study the experimental data and to validate the model predictions. The B-A model assumes isothermal column with constant fluid velocity. Axial dispersion is neglected in the B-A model and LDF assumption is made to describe the adsorption rate.

$$\frac{C}{C_0} = \frac{\exp\left(k' C_0\left(t - \frac{L}{u}\right)\right)}{\exp\left(k' C_0\left(t - \frac{L}{u}\right)\right) + \exp\left(\frac{k' q_s L}{u}\left(\frac{1-\varepsilon}{\varepsilon}\right)\right) - 1} \tag{6.7}$$

The calculation of the breakthrough curve using B-A model (Eq 6.7) was subjected to two approximations proposed by Cooney [193], *i.e.* $t >> L/u$ and the omission of the term "1" from the denominator. Therefore, the simplified expression of B-A model was obtained as Eq 6.8, which can be linearised to present time (t) as a function of $[\ln(C_0/C-1)]/C_0$. In order to check that the experimental data conform to B-A model, plotting the experimental breakthrough curves in terms of time (t) *versus* $[\ln(C_0/C-1)]/C_0$ should yield a straight line [194]. The method of estimating k' can be achieved by fitting the experimental data directly to the linearised model.

$$\frac{C}{C_0} = \frac{1}{1 + \exp\left(k'\left(q_s(1-\varepsilon)\frac{L}{u} - C_0 t\right)\right)} \tag{6.8}$$

6.3 *Results and discussion*

6.3.1 Characterisation

Commercial AC, bulk CuBTC and pelleted CuBTC MOF were used in this work as the model adsorbents to study the effect of propagation velocity of mass transfer zone on breakthrough curves. All samples were characterised prior to CO_2 and N_2 adsorption measurements using PXRD, SEM, and BET analyses. Figure 6.2a and b show the PXRD patterns of bulk AC and bulk CuBTC MOF in powder and pellets forms, respectively. The two broad peaks in the PXRD pattern of AC at 2θ of (*ca.* 20–30º) and (*ca.* 40–50º) corresponding to (002) and (100) plane reflections, respectively, are related to the amorphous carbon structure [195, 196]. The PXRD patterns of CuBTC MOFs are comparable to the simulated one that reveal the pure crystalline phases of CuBTC MOF samples.

The surface areas of the three samples were calculated based on the measured nitrogen adsorption isotherms at –196 ºC. The surface areas of the three samples were found to decrease in the order of CuBTC powder > CuBTC pellets > AC, as shown in Table 6.3.

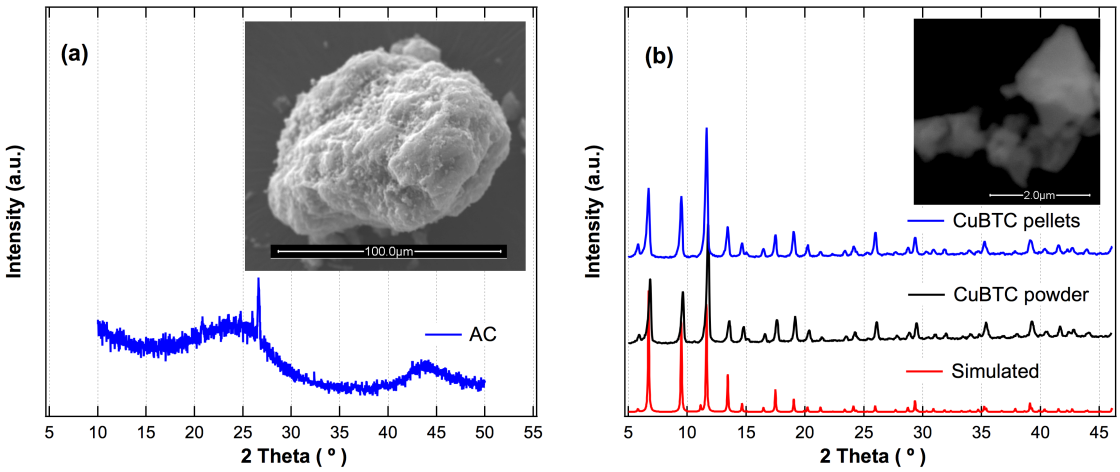

Figure 6.2. PXRD patterns of (a) AC and inset AC SEM image, (b) CuBTC MOFs powder and pellets and inset SEM image of CuBTC MOF powder, simulated pattern is adopted from [19].

Table 6.3
BET surface area of bulk AC, bulk CuBTC MOF and pelleted CuBTC MOF.

Material	Surface area, m^2/g
AC	1155 ± 44
CuBTC powder	1655 ± 79
CuBTC pellets	1452 ± 71

6.3.2 Equilibrium adsorption

The equilibrium adsorption isotherms of pure CO_2 and N_2 on the solid adsorbents (bulk AC, bulk CuBTC MOF and pelleted CuBTC) were measured using the gravimetric analysis, as shown in Figure 6.3. Langmuir model was employed to fit the measured isotherms, by which the corresponding kinetic parameters were determined using nonlinear regression for the subsequent theoretical calculations (Table 6.4). In a pressure range of 0–20 bar, all materials showed a higher adsorption capacity of CO_2 than that of N_2, which can be attributed to the high polarisability and quadruple moment of CO_2 (quadruple moment: CO_2 = 13.4 C m^2 versus N_2 = 4.72 C m^2) [170]. The uptake selectivity by the Ideal adsorbed solution theory (IAST) [109, 110] was predicted under conditions of 1 bar total pressure, 50 °C and 15% CO_2 composition. It was found that the IAST selectivity of materials followed the order of bulk CuBTC MOF (16.03) ≈ pelleted CuBTC MOF (16.01) > bulk AC (8.70).

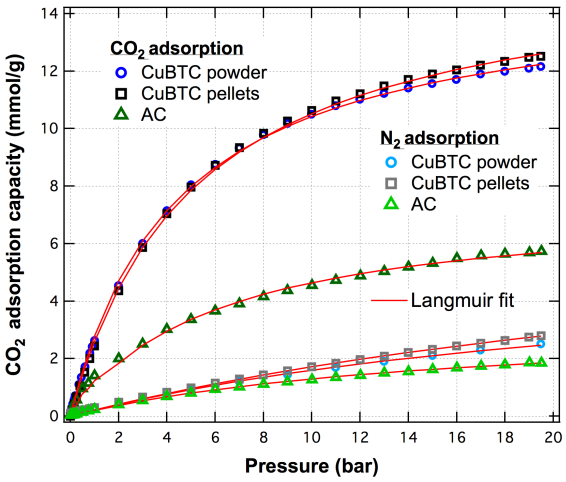

Figure 6.3. Single-component CO2 and N2 adsorption isotherms for bulk CuBTC MOF, pelleted CuBTC MOF and bulk AC at 50 ºC over a pressure range of 0–20 bar.

Table 6.4
Kinetic parameters of equilibrium adsorption of CO_2 at 50 °C.

	Bulk AC	Bulk CuBTC	Pelleted CuBTC
Henry's constant (bar^{-1})	0.164	0.185	0.190
Saturation capacity (mmol/g)	7.462	15.970	15.970

6.3.3 Breakthrough experiments

The breakthrough curves presented in this work were corrected by subtracting the dwell time from the measured breakthrough time to yield the exact time at which CO_2 reaches the adsorbent bed and the micro GC (blank correction). The dwell time was calculated as the dead volume of piping (before and after the packed adsorbent bed) divided by the total flow rate flowing inside. The repeatability of the breakthrough experiment was measured as < 6% for all experiments (An example is shown in Appendix A.9).

6.3.3.1 Model validation and parametric study

A study using two numerical models implemented in Matlab was carried out to investigate the effects on the breakthrough curves when using the constant and variable velocity assumptions. The system was assumed to behave as an ideal gas, and the gas viscosity was 16.13×10^{-6} Pa.s at 1 bar [197]. The total pressure of the column was 1 bar and the CO_2 feed concentration was 50%. The adsorption isotherm for CO_2 on activated carbon measured experimentally was fitted to a Langmuir isotherm, with parameters given in the Table 6.4. The rate constants for the B-A model were obtained from experimentally measured breakthrough curves by linearising Eq 6.8 as shown in Appendix A.10. The theoretical B-A model assumes constant fluid velocity through the bed [194], and it was found previously to be capable of predicting the breakthrough behaviour of solid adsorbents (*e.g.* polyethylenimine immobilised on mesoporous silica [198] for CO_2 separation for the purpose of scaling up.

Figure 6.4a shows that there is a significant difference between the breakthrough curves when velocity is considered constant or variable assuming local equilibrium. Figure 6.4a also shows that the time at which $C/C_0 = 0.5$ (t_{b50}) in the curves for constant velocity coincides with the B-A model (Appendix A.11). More

importantly, it shows that the breakthrough time for the variable velocity model is significantly smaller than for the constant velocity model, despite using the same adsorption isotherm model in both cases. This difference in t_b decreases with increasing flow rate, but the ratio of t_b between both models is always within 15–17%. Results suggest that the total amount adsorbed at infinite time with the variable velocity model is lower than with the constant velocity model.

The breakthrough curves assuming the local equilibrium approximation (Figure 6.4a) are significantly sharper than those obtained with the linear driving force approximation (Figure 6.4b). Nevertheless, in both cases a noticeable shift is observed when considering constant or variable velocity. Experimental data can be well represented assuming the linear driving force model and variable velocity.

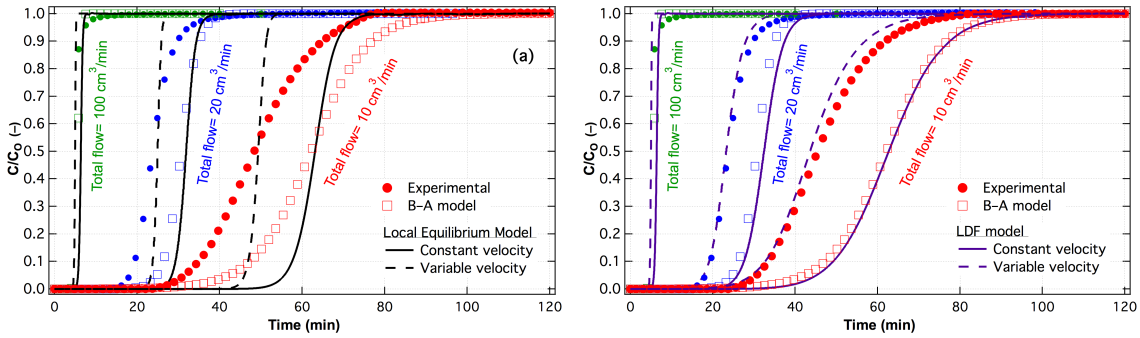

Figure 6.4. (a) Comparison of modelled breakthrough curves based on the local equilibrium model, considering constant (solid line) or variable (dashed line) velocity at different flow rates. Solid symbols represent experimental data and open symbols represent the B-A model; (b) Comparison of modelled breakthrough curves based on the linear driving force model, considering constant (solid line) or variable (dashed line) velocity at different flow rates. Solid symbols represent experimental data and open symbols represent the B-A mode.

The effect of adsorbable gas (CO_2) inlet concentration on the breakthrough curves was studied by changing the N_2 flow rate based on a constant CO_2 flow rate (5 cm^3/min). Results for experiments performed using three adsorbents of bulk AC, bulk CuBTC and pelleted CuBTC MOFs are presented in Figure 6.5. Decreasing the concentration of CO_2 in the feed reduced the deviation between the constant and variable velocity breakthrough curves, which is expected because having a lower concentration in the feed takes the system closer to the idealized constant velocity case that is valid only for trace adsorption. A parametric study in Figure 6.6 shows that the variable and constant velocity models converge at very low concentrations, supporting the above statements. It was found that the

discrepancy between the two models increased exponentially with the increasing CO_2 composition in the feed stream, as shown in Figure 6.6b.

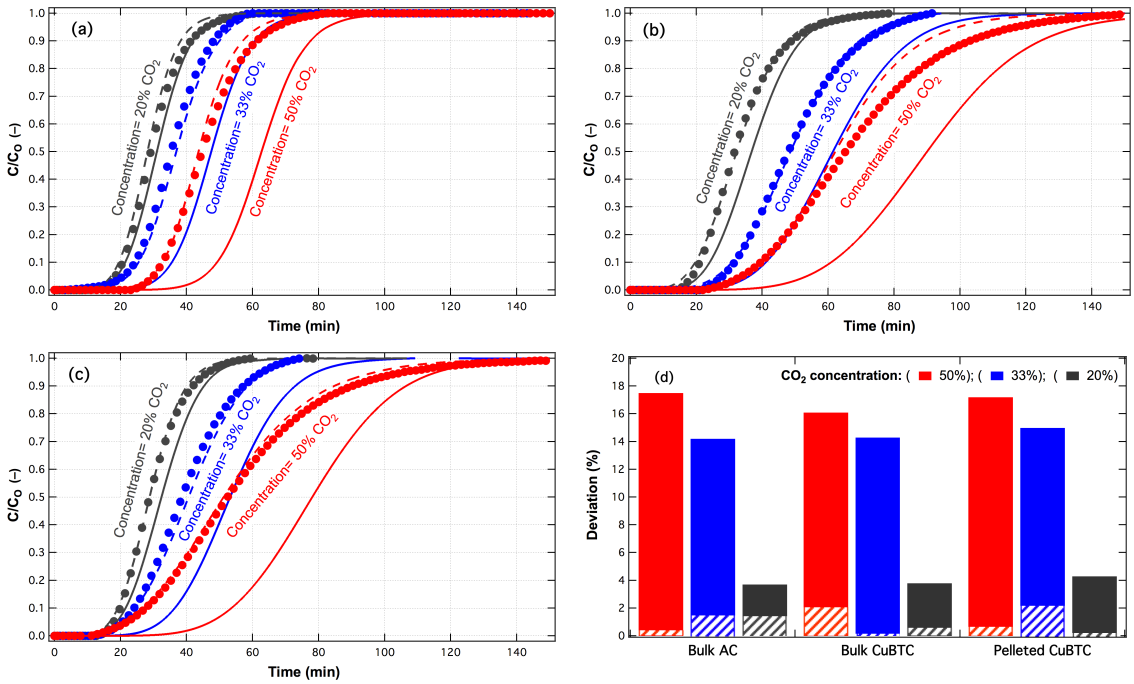

Figure 6.5. Breakthrough curves at different feed CO_2 concentrations (CO_2 = 5 cm^3/min) (a) bulk AC; (b) bulk CuBTC MOF; and (c) pelleted CuBTC MOF, Solid circles represent experimental data, solid lines are the model with constant velocity assumption, and dash line are the model with variable velocity assumption; (d) deviation of t_{b50} between the experimental data, constant and variable velocity models.

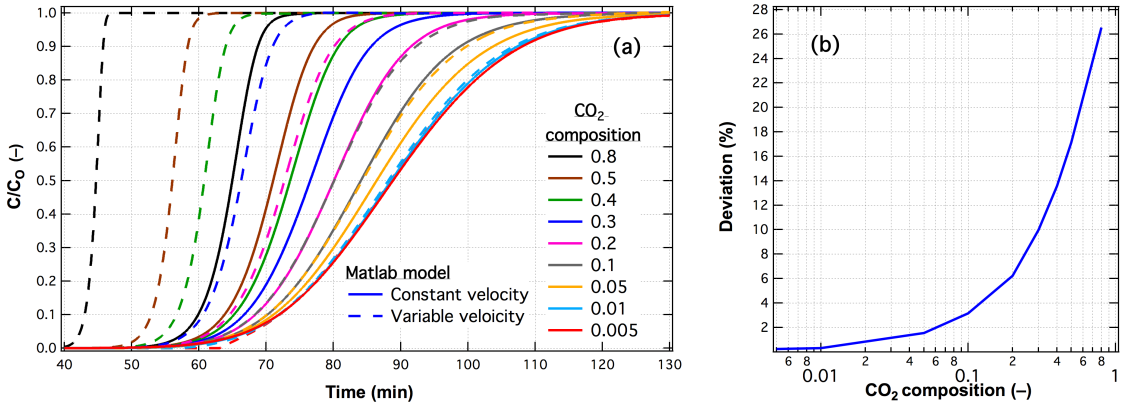

Figure 6.6. Parametric study of the effect of CO_2 feed concentration on the breakthrough curves considering constant and variable velocities (total flow = 10 cm^3/min, total inlet pressure = 1 bar, T = 50ºC). (a) Simulated breakthrough curves by the numerical models with different velocity assumptions, solid lines (—): Numerical model with constant velocity assumption, dash line (- -): Numerical model with variable velocity assumption. (b) Deviations of t_{b50} between simulated results of numerical modes with different velocity assumptions.

Experimental results for AC and pelleted CuBTC MOF, and bulk CuBTC MOF at low concentration were well described by the variable velocity LDF model. Nevertheless, the breakthrough curve of CO_2 on powder CuBTC MOF when the gas feed concentration was 50% showed some significant deviations from the model at long times. It is possible that heat effects due to the high heat of adsorption of CO_2 on CuBTC MOF played a more important role when the adsorbent is a powder. The measured adsorption isotherms for CO_2 on CuBTC MOF powder and pellets are practically the same (Figure 6.3). The t_b for CO_2 on CuBTC MOF powder is 23 min, whereas for CO_2 on CuBTC pellets is 14 min, suggesting that mass transfer resistances are more important in the pellet form, and probably allowing more time for heat transfer and enabling the system to be isothermal. As the CO_2 concentration decreases, heat effects decrease, as expected.

In order to develop a better understanding of how the feed concentration of the gaseous adsorbate influence the propagation velocity (*w*), a correlation was derived in this work based on the mass balance of a binary system and Langmuir model, as Eq 6.9 (the full detail of the derivation of Eq 6.9 can be found in Appendix A.12).

$$w = \left(\frac{\partial z}{\partial t}\right)_C = \frac{u_n}{1+(\frac{1-\varepsilon}{\varepsilon})\rho_g(1-y_i)\frac{K_i n_{s,i}}{(1+K_i C y_i)^2}} \tag{6.9}$$

Based on Eq 6.9, the propagation velocity is clearly an increasing function of the feed concentration of the adsorbate, as shown in Figure 6.7, which confirmed the results of the enhanced effect of the velocity variation on breakthrough curves with an increase in the CO_2 concentration (Figure 6.5d). Similar results were also reported by Ruthven [177], which showed an increase in *w* as a result of the adsorbate uptake at high concentrations based on linear adsorption model.

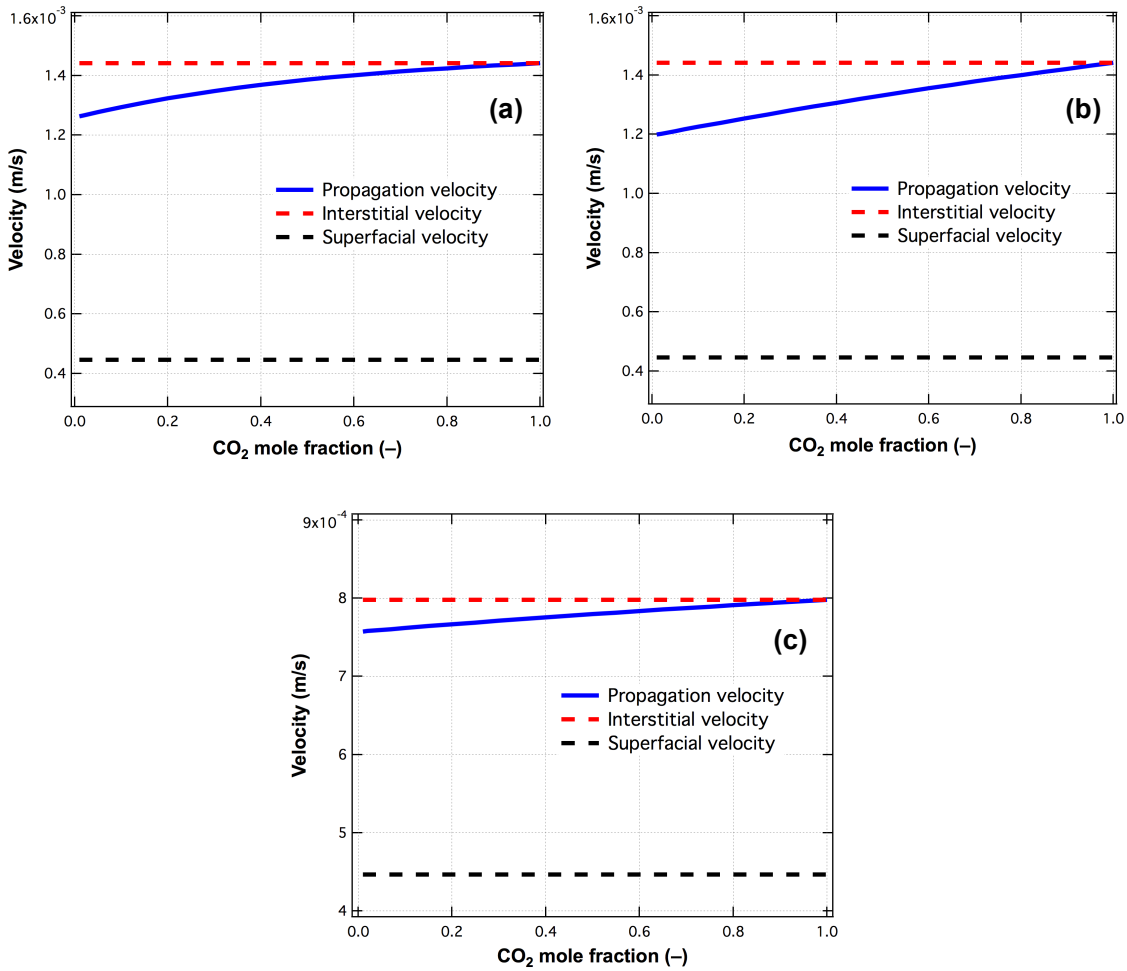

Figure 6.7. Predicted effect (by Eq 6.9) of the feed concentration of the adsorbable gas (CO_2) on the propagation of mass transfer zone (P = 1 bar, T = 50 ºC and F_{total} = 10 cm^3/min). (a) bulk AC; (b) bulk CuBTC; (c) pelleted CuBTC.

Figure 6.7 shows an increase in the propagation velocity (calculated based on Eq 6.9) as a result of the increase in feed CO_2 mole fraction until w reaches the value of interstitial velocity for the CO_2/N_2 mixture. This result suggests that the propagation velocity is equal to the interstitial velocity (u_n) where the effect of adsorption becomes negligible compared to the effect of flow through a bed of porous media.

6.3.3.2 Parametric study: calculation of CO_2 adsorption isotherms

In the fixed bed adsorption studies, the quantity of adsorbable gas on the solid adsorbent is usually determined from the breakthrough experiments by applying mass balance to the bed, as illustrated in Eq 6.10.

$$q_{CO2} = \frac{y_i F_0 C_0 t_b}{W} \tag{6.10}$$

where q_{CO2} is the quantity of CO_2 adsorbed per unit mass of adsorbents, y_i: is the CO_2 mole fraction in the feed, F_0, and C_0 are the initial total flow rate and concentration, W: is the mass of adsorbent and t_b is the stoichiometric time which is given by:

$$t_s = \int_0^t \left(1 - \frac{y_e}{y_i}\right) dt \tag{6.11}$$

However, Malek et al. [199] reported that due to the significant velocity difference between the inlet and exit of the column caused by adsorption or desorption of adsorbable gas for non trace systems, Eq 6.10 may considerably affect the calculated equilibrium adsorption data. Therefore, an expression of the stoichiometric time was proposed, which provided practically useful approximations of the effect of flow variation in single adsorbable gas systems (case studies: methane and ethane adsorption on activated carbon) as given in Eq 6.11 [199]. According to their results, the corrected stoichiometric time for velocity variation based on Eq 6.11 worked well for adsorbable feed composition of ≤20%.

$$t_s = \int_0^t \left(1 - \frac{y_e}{y_i}\frac{(1-y_i)}{(1-y_e)}\right) dt \tag{6.12}$$

The equilibrium adsorption capacity of CO_2 adsorption on AC, bulk and pelleted CuBTC has been calculated first based on the stoichiometric time given in Eq 6.11 as shown in Appendix A.13. It can be seen from Appendix A.13 that the velocity change affects the uncorrected equilibrium value calculated based on the breakthrough measurements for the three adsorbents, and that the error increases with increasing the feed adsorbable gas composition. This observation agrees well with the reported results of Malek et al. [199] for other gases. Therefore, the corrected stoichiometric time, Eq 6.12, was used to estimate the equilibrium data from the breakthrough measurements as shown in Figure 6.8. The corrected equilibrium data, based on breakthrough measurements, showed a good agreement with the equilibrium data measured gravimetrically at 20% CO_2 composition for the three adsorbents. At higher feed concentration of 50% and 80%, the corrected data (Eq 6.12) are still underestimating the gravimetric equilibrium, however, with improvements of 40% and 34% (compared to the calculations based on Eq 6.11).

Therefore, the results showed that the assessment of the adsorption capacity of porous materials using the breakthrough measurements might be arbitrary and underestimate the working adsorption performance of materials under real conditions if the process parameters such as the velocity variation across the bed during the adsorption process are not considered.

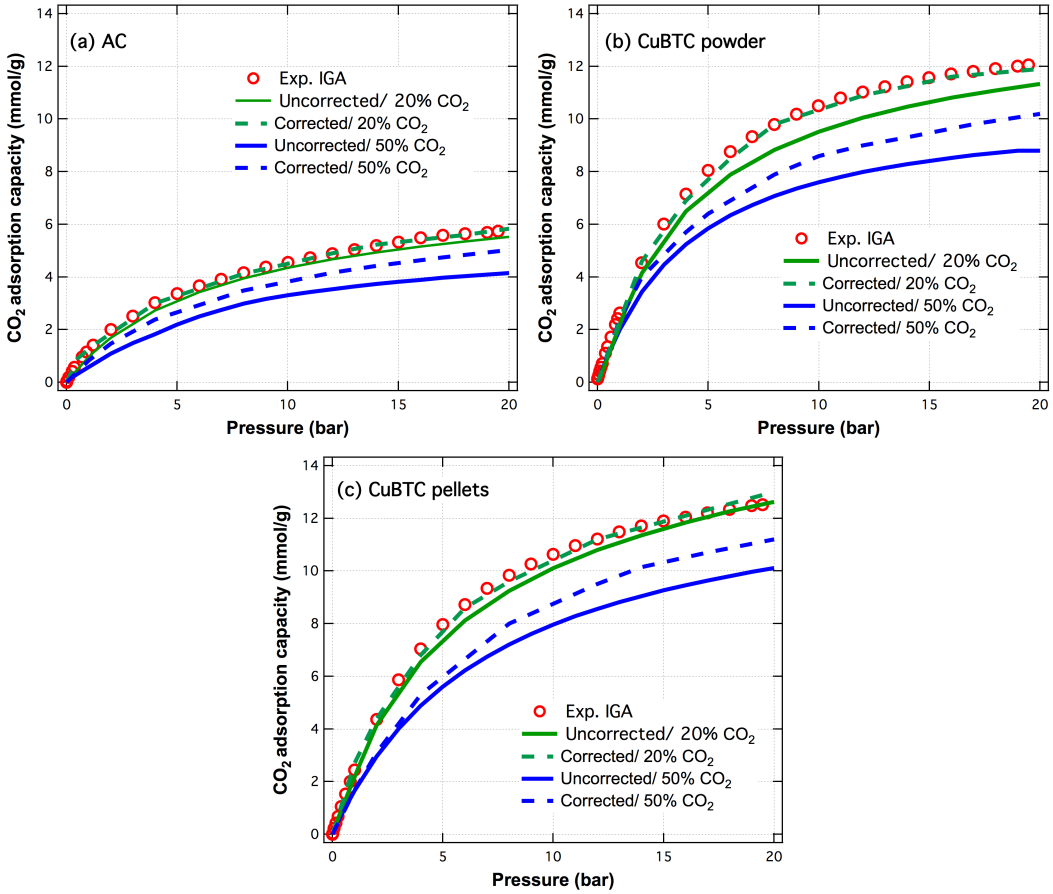

Figure 6.8. Deviation in CO_2 adsorption isotherms at 50 ºC for (a) Bulk AC, (b) Bulk CuBTC MOF, (c) Pelleted CuBTC MOF when corrections for variable velocity are applied in the estimation of the total amount adsorbed.

6.3.4 Screening of adsorbents: purity of adsorbed CO_2

The purity of separated CO_2 is an important factor that reflects the efficiency of adsorption processes. The purity of the separated CO_2 (x_{CO_2}), as defined by Eq 6.13, needs to be more than 95% for subsequent transportation and sequestration [27]. The value of x_{CO_2} can be estimated based on the adsorption isotherms and it should be considered in the screening of adsorbents for CO_2 capture:

$$x_{CO_2} = \frac{\Delta q_{CO_2}\rho_g\left(1-\varepsilon\right) + y_{CO_2}\dfrac{\varepsilon P_{feed}}{RT}}{\Delta q_{CO_2}\rho_g\left(1-\varepsilon\right) + \dfrac{\varepsilon P_{feed}}{RT}} > 0.95 \quad (6.13)$$

where Δq_{CO_2} is the working capacity (mol/kg), *i.e.* the difference of adsorption capacity between the highest and lowest working CO_2 partial pressures [176]; ρ_g is the particle density (kg/m^3); ε is the void fraction of the adsorption column; P_{feed} is the pressure of the feed (Pa); and T is the temperature of the feed (K).

In order to show the effect of velocity variation on the purity of CO_2 in the exhaust gas, the purity of CO_2 has been calculated based on the corrected and uncorrected equilibrium adsorption capacities as shown in Table 6.5. The purity of CO_2 has been estimated for the adsorbents used in this work based on a model flue gas, with of total pressure = 1 bar, temperature = 50 ºC and CO_2 composition = 15%. The minimum working capacity (Δq_{CO_2}) was calculated based on the CO_2 partial pressures 0 and 0.15 bar CO_2.

Based on corrected equilibrium data, both bulk CuBTC and pelleted CuBTC MOFs showed values of x_{CO_2} higher than 95%, indicating that they are suitable porous materials for CO_2 capture. However, when the correction of adsorption capacity due to the velocity variation effect was not considered, bulk CuBTC MOF showed the capability of separating CO_2 from flue gases with purity marginally higher than 95%, while, CuBTC pellets only have x_{CO_2} = 92.9%, not fulfilling the requirement on CO_2 purity. These results showed that the lack of consideration of velocity effect might lead to erroneous evaluation of the suitability of adsorbents for practical applications. Additionally, other factors need to be considered for their applications in practical CO_2 adsorption, such as the hydrothermal stability of CuBTC MOFs [181, 200].

Table 6.5

Minimum working capacity and purity of adsorbed CO_2 determined by the gravimetric analysis and fixed bed adsorption.

Adsorbent	Gravimetric analysis		Fixed bed adsorption	
	Δq_{CO_2} (mmol/g)	x_{CO_2} (%)	Δq_{CO_2} (mmol/g)	x_{CO_2} (%)
Bulk activated carbon	0.242	90.9	0.167	87.5
Bulk CuBTC MOF	0.496	96.7	0.337	95.4
Pelleted CuBTC MOF	0.479	95.1	0.329	92.9

6.4 *Conclusion*

The effect of the propagation velocity in fixed bed adsorption columns on the CO_2 breakthrough behaviour was investigated using a combined experimental and numerical approach. We showed that considering a variable velocity through the bed is necessary for correctly describing CO_2 capture in activated carbon, crystalline bulk CuBTC MOF and pelleted CuBTC MOF, unless a very diluted feed is considered (with CO_2 concentration <1%). It should be noted that the effect of a high pressure drop was not considered in this study, which can affect the propagation velocity (Zwiebel, 1969), because the experimentally measured pressure drop in our system was less than 6×10^{-3} bar.

This work shows that the shift between the breakthrough time considering constant and variable velocity grows exponentially with the adsorbate concentration in the feed. Malek et al. suggested that the correction for variable velocity should be implemented when the feed concentration is higher than 20% for light adsorbing gases (methane and ethane on activated carbon) to have errors smaller than 2% in the equilibrium amount adsorbed [199]. For gases that adsorb stronger, such as CO_2 on activated carbon, a feed concentration of 20% results in a shift of the breakthrough time of 6%, and a deviation in the equilibrium amount adsorbed of 6%. For CO_2 adsorption on bulk and pelleted CuBTC same deviations (*i.e*. 6%) in breakthrough curves and equilibrium amount adsorbed were observed.

In this work we show that the percentage shift in the breakthrough curves (or error in the estimation of the total amount adsorbed) is practically independent of the total flow rate or the adsorbent used, but strongly dependent on the feed concentration. Comparing to work reported in the literature [199], the error in the total amount adsorbed is dependent of the gas considered.

According to these findings, the common evaluation of porous adsorbents for carbon capture based on the equilibrium adsorption using gravimetric analysis should be complemented by the fixed bed adsorption analysis to make a fair judgment on predicting the performance of materials under flow conditions.

Nomenclature

C	mol/m^3	Total concentration
C_i	mol/m^3	Component concentration

C_0	mol/m^3	Initial concentration
D	m	Internal column diameter
d	m	Particle diameter
F	cm^3/min	Flow rate
K	m^3/mol	Henry's constant, Langmuir model parameter
k_i	1/s	Mass transfer coefficient / LDF equation
k'	1/s	Mass transfer coefficient / B-A model
L	m	Total bed length
n_s	mmol/g	Saturation capacity, Langmuir model parameter
P	bar	Total pressure
P_0	bar	Initial pressure
q_i	mmol/g	Average adsorbed amount
q^*	mmol/g	Equilibrium adsorbed amount
q_s	mmol/g	Saturation capacity per unit volume of bed / B-A model
R	Pa m^3/mol K	Gas constant
T	K	Temperature
t	min	Time
u	m/s	Superficial velocity = Flow/Area
y	–	Mole fraction
z	m	Length of one segment in the fixed bed

Greek letters

ε	–	Void fraction
μ_g	Pa s	Viscosity of gas
ρ	kg/m^3	Density of gas
ρ_g	kg/m^3	Grain density

Chapter 7

Assessment of MOF's quality: quantifying defects content in crystalline porous materials

This Chapter contains the content of a published peer-reviewed article in the Journal of Physical Chemistry Letters (7 (2016): 1490, DOI: 10.1021/acs.jpclett. 6b00297). In this Chapter, a quantitative method based on the grand canonical Monte Carlo (GCMC) simulation for the assessment of defects in metal-organic framework (MOF) is presented. Defects in the structure of MOFs generated during the synthesis and work-up can lead to large variations in experimentally measured adsorption isotherms, but are difficult to quantify.

A case study of CO_2 adsorption on CuBTC MOF (BTC = benzene-1,3,5-tricarboxylic acid) was used to show that different samples of CuBTC MOF reported in the literature have various proportions of blocked principal pores or blocked side pores, resulting in isotherms with different capacity and affinity towards CO_2. The presented approach is generic and applicable to other materials, showing that simulation results combined with experimentally measured gas adsorption isotherms can be used to quantitatively identify key defective features of the material.

7.1 *Introduction*

The increasingly growing numbers of applications that can benefit from novel porous materials demand a good understanding of their structures. Characterisation of microporous materials has evolved, but gas adsorption isotherms are still the most popular and valuable tool for evaluating and guiding their design. Crystalline and amorphous porous materials are often characterised using their surface area as calculated based nitrogen adsorption, but materials with the same surface area can have different performances, demanding further characterisation methods. Pore size distribution is widely accepted as a metric to characterise further amorphous materials [201, 202], but such metric is not necessarily descriptive of crystalline materials. PXRD is generally used to determine the structure of crystalline materials, but this does barely account for defects in the crystalline structure.

CuBTC MOF [19] is a good example of microporous crystalline materials where inconsistent experimentally measured CO_2 adsorption isotherms have been reported [47, 93, 98, 105, 106, 116-118]. CuBTC MOF is a well-known open metal sites (OMSs) MOF that is constructed by coordinatively linking unsaturated copper sites with benzene tricarboxylate (BTC) ligands rendering a microporous structure with tetrahedron-shaped side pockets, square-shaped principal pores and triangular windows [23, 24, 48]. OMSs are believed to be the preferable adsorption sites for gas adsorption on MOFs for polar molecules such as water, and non polar like methane under low pressures [23, 154-157] proved by *in situ* IR measurements (0.009 bar and temperature range of –123–27 ºC) for CuBTC MOF [155]. Recent development showed that the effect of OMSs on adsorption of MOFs could be realised by using the Quantum Mechanics combined with Grand Canonical Monte Carlo QM/GCMC approach [154, 203]. Here, the adsorption energy of OMSs in MOFs is computed using QM calculations then used as inputs (by adding additional sites to OMSs) into the subsequent GCMC simulations [154, 203]. In comparison to GCMC modelling, QM/GCMC modelling showed improvement in the capability of predicting the experimental isotherms (conditions: pressure range = 0–1 bar, temperature = 50–150 ºC) in the case of propylene adsorption on CuBTC MOF [154]. Further development of this approach was, the ability to use the calculated parameters that represent the open metal sites

interactions from QM of ethylene adsorption on CuBTC MOF to simulate ethylene adsorption on other MOFs *i.e.* PCN-16, NOTT-101 and MOF-505 [203]. Very good agreement with the experimental data was achieved in the case of PCN-16 and NOTT-101 MOFs. However, simulated isotherms on MOF-505 showed overestimation compared to the experimental data which was attributed to insufficient equilibration of the latter. Furthermore, it was found that the parameters of open metal sites in dimer units (in the case of CuBTC MOF) are not transferable to trimmer units (in the case of UMCM-150 MOF) which required separately determined parameters [203].

The discrepancy between the CO_2 adsorption capacities obtained in the experiments may arise from experimental errors during the measurement of adsorption isotherms or presence of some impurities that affects the single gas adsorption. For example, experimental measurement of gas adsorption on MOFs with OMSs also depends on the sample preparation, in which, Yazaydin *et al.* [49] showed that the presence of water molecules within the structure of CuBTC MOF could enhance the CO_2 adsorption capacity significantly. Another comprehensive study on the effect of the existence of different impurities in several MOFs including CuBTC MOF such as SO_2, NO_2, NO, CO, and O_2 on CO_2 adsorption was performed [204], which revealed that some impurities enhance the CO_2 uptake and others regress it. Furthermore, high temperature synthetic procedures can also lead to the formation of by-products, as discussed in Chapter 3, that may affect the adsorption isotherms.

In this Chapter, a metric that quantifies the defects in crystalline porous materials was proposed following ideas originally used for determining pore size distribution [201, 202]. By using the molecular simulation and gravimetric analysis, the identification of structural defects in CuBTC MOF and quantification of the defect were carried out. The presented method was found to be able to explain the inconsistencies in reported experimentally measured isotherms on CuBTC MOFs.

7.2 *Experimental section*

7.2.1 Synthesis of materials

CuBTC MOFs were prepared using the improved hydrothermal (HT) method (as described in Chapter 3) and microwave-assisted method (MW). MW synthesis was performed at 170 ºC for 10 min following a procedure reported by Seo *et al.* [69]. The synthesis was carried out using a microwave synthesis reactor (CEM Discover SP-D 10/35). Copper (II) nitrate trihydrate $Cu(NO_3)_2 \cdot 3H_2O$ and benzene-1,3,5-tricarboxylic acid (BTC) were used as the reactants with ethanol and water as solvents. Same work-up and activation procedure were used for both materials as described in Chapter 3.

7.2.2 Characterisation of materials

Powder X-ray diffraction (PXRD), scanning electron microscopy (SEM) analysis, differential scanning calorimetric (DSC) analysis, nitrogen adsorption/desorption isotherms at −196 °C and pure CO_2 and N_2 adsorption were performed following the experimental procedures given in Chapter 3 and 4.

7.3 *Computational methods*

Pure CO_2 adsorption isotherms of CuBTC MOF were simulated using the grand canonical Monte Carlo ensemble in Towhee [89], where the volume, temperature (25 ºC) and gas chemical potential are constant during the simulation (μvT). Isobaric-isothermal ensemble (NPT) was used to estimate the chemical potential and bulk property at each pressure increment from 1 to 20 bar. For each pressure point in an isotherm, 5×10^6 Monte Carlo steps were used for equilibration, and additional 10×10^6 steps were performed for collecting the data. Within these steps, CO_2 molecules undergo insertion, deletion, and translation/rotation trials.

In all simulations, CuBTC MOFs were modelled as 3D rigid structures with periodic cubic unit cells (26.343 Å × 26.343 Å × 26.343 Å). Lenard-Jones parameters of all atoms were taken from the adjusted OPLS-aa force field except those of copper were taken from UFF [48, 108]. The partial charges of the framework were obtained from the literature, Table 7.1 [48, 108]. Lenard-Jones cross interactions were calculated using the Lorentz-Berthelot mixing rule [205]. A cut-off radius of

13 Å was used for Lenard-Jones interactions. Ewald summation was used for computing the electrostatic interactions [205]. CO_2 molecules interactions were modelled using TraPPE-EH force field [206], in which a carbon dioxide molecule was modelled as a rigid molecule with three charged interaction sites. The C=O bond length is 1.16 Å and the O=C=O angle is 180°.

Table 7.1
Partial charges on an intact asymmetric unit cell of CuBTC MOF [48, 108].

Element	Charge	No. of atoms in one unit cell
Copper (Cu)	1.098	48
Oxygen (O)	−0.665	192
Carbon in carboxylic group (C1)	0.778	96
Carbon of benzene-C (connected to carboxylic group, C2)	−0.092	96
Carbon of benzene-H (C3)	−0.014	96
Hydrogen in benzene (H)	0.109	96

GCMC simulations yield values of the absolute adsorption capacity (*i.e.* the total amount of adsorbed gas molecules) rather than the excess adsorption capacity. Therefore, the simulated absolute adsorption capacity was converted to the excess adsorption capacity using Eq 7.1.

$$N_{\text{ex}} = N_{\text{abs}} - \rho_{\text{g, bulk}} \cdot V_{\text{s, free}} \tag{7.1}$$

where N_{ex} and N_{abs} are the excess and absolute CO_2 adsorption capacity (mmol/g), respectively. $\rho_{g,bulk}$ is the density of bulk CO_2 determined by the NPT ensemble calculations. $V_{s,free}$ is the free pore volume (0.85 cm^3/g, adapted from reference [137]) of CuBTC MOF.

7.4 *Results and discussion*

7.4.1 Characterisation of CuBTC MOFs

Figure 7.1 shows a collection of CO_2 adsorption isotherms of CuBTC MOFs at 25 °C. It can be seen that there is an inconsistency in the measured CO_2 adsorption

isotherms on CuBTC MOF as well as the variation in the amount adsorbed at 20 bar in a range of 8 to 18 mmol/g.

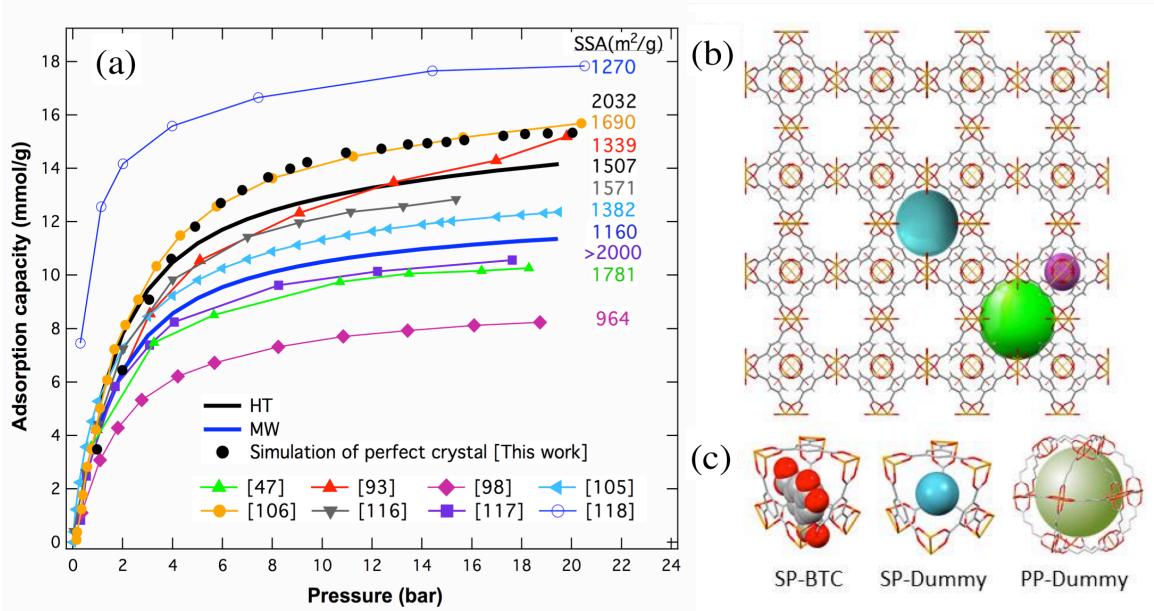

Figure 7.1. (a) Experimentally measurements of pure CO_2 adsorption isotherms on CuBTC MOF at 25 °C reported in the literature [47, 93, 98, 105, 106, 116-118] and measured in this work; (b) CuBTC MOF structure showing the primary pores (11 Å and ~13 Å) and side pockets (~5 Å); (c) side pocket (SP) and primary pores (PP) defects used in this work.

Several factors may be led to differences in the reported adsorption isotherms [47, 93, 98, 105, 106, 116-118], from the preparation method that affects the quality of the structures to the pre-treatment of the samples before the isotherm measurement [207]. Defective pore structures of MOFs can be produced during the material's preparation and work-up, which are difficult to quantify using characterisation techniques such as PXRD, SEM, DSC and N_2 adsorption, leading to the immense disparity in gas adsorption isotherms for the "same" material under the "same" conditions. For example, CuBTC MOFs were synthesised using both hydrothermal (HT) and microwave-assist (MW) methods and significant differences were found in the measured pure CO_2 adsorption isotherms in the resulting materials despite the similarities of the PXRD pattern of the two CuBTC MOFs (Figure 7.2). The difference in the surface area measured using N_2 adsorption at –196 °C suggests that the MW method results in a material which restricts the access of adsorbed molecules to the pore network, as the surface area is significantly smaller than in the materials obtained using the HT method (1167±18 *vs.* 1507±26 m^2/g, respectively), but does not provide any insight into

the nature of the defects that lower the specific surface area (SSA). Molecular simulations can provide valuable insight in this case. An isotherm calculated using GCMC simulations with a perfect CuBTC MOF structure shows a lower CO_2 uptake than experimental measurements at low pressures, and a higher uptake at high pressures (Figure 7.2a).

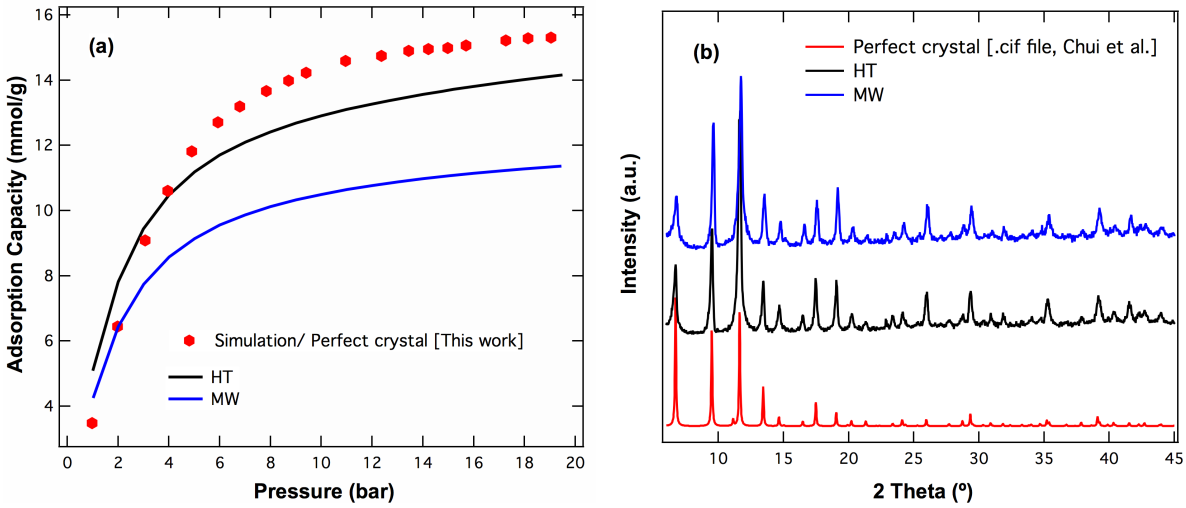

Figure 7.2. (a) Measured and simulated adsorption isotherms of CO_2 adsorption on CuBTC MOF at 25 °C (b) PXRD pattern of the HT and MW samples synthesised in this work. Simulated pattern has been adapted from Chui *et al.* [19].

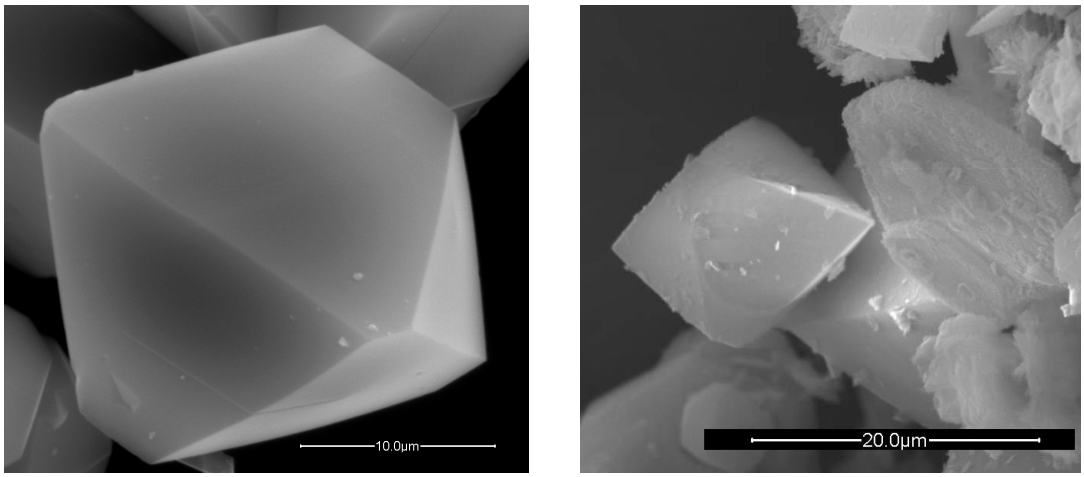

Figure 7.3. SEM images of the (a) hydrothermal sample and (b) microwave sample.

A reduction in accessible pore network regions is often observed in porous materials [208] and isotherms are simply scaled by a constant factor that represents the ratio of the accessible volume to the total volume of an idealised

material. Nevertheless, in this case, such simple scaling procedure would not result in a good agreement between the calculated and measured isotherms. Although rotation of linkers in MOFs can be responsible for discrepancies between calculated and experimentally measured isotherms [209], changes in the orientation are strongly limited by the coordination with three different metal centres in the case of benzene tricarboxylate based structures.

7.4.2 Effect of open metal sites on molecular simulations

Molecular simulations based on classical force fields without considering the free electrons of unsaturated metals do not have the capability to capture the interactions between the adsorbed molecules and open metal sites (OMSs). It may lead to the underestimation of CO_2 adsorption capacity on CuBTC MOF across the low pressure range.

a) P = 1bar, T= 25 °C. b) P = 0.01bar, T= –25 °C. c) P = 0.003bar, T= –25 °C.

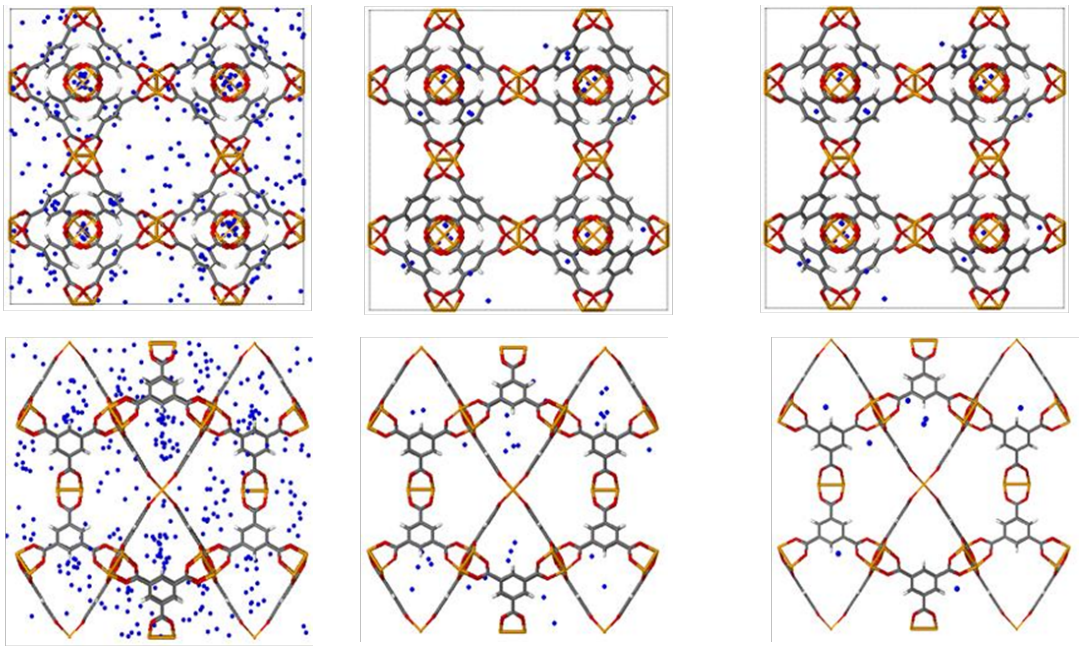

Figure 7.4. Snapshots of modelled CuBTC MOF with adsorbed CO_2 at different pressures and temperatures. CuBTC MOF is shown in line style: Cu, yellow; O, red; C, grey; and H, white. Carbon atoms in CO_2 molecules are represented by the blue spheres.

In this study, GCMC simulations were performed at various pressures and temperatures to identify the favourable adsorption sites of CO_2 on CuBTC MOF. At 1 bar and 25 °C (Figure 7.4), simulated results are comparable to ones reported in

literature, *i.e.* side pockets (SPs) as the initial favourable adsorption sites [48, 108, 121, 156]. The simulated adsorption isotherms that correspond to those conditions are also found lower than ones measured in this study by experiments (Figure 7.2a) within the range of low pressures (< 2 bar for MW sample and < 4 bar for HT sample). Such underestimation of adsorption isotherms by molecular simulations was also reported by Yazaydin *et al.* [49] and Karra and Walton [93].

Therefore, additional simulation work in this study was carried out at low CO_2 pressures of 0.003 and 0.01 bar and low temperature of –25 °C (above the CO_2 condensation temperatures at the studied low pressures) in order to evaluate the change of preferable adsorption sites at low CO_2 loadings. However, similar results were obtained from these simulations as seen in Figure 7.4b and c, *i.e.* SPs in CuBTC MOF as the initial favourable adsorption sites, indicating that in the region of low CO_2 pressures adsorption on CuBTC MOF in GCMC simulations is the SPs.

Snurr and co-workers [156] calculated the simulated heat of adsorption and broke them down into their contributions of Lennard-Jones and electrostatic interactions. The simulated heat of adsorption of CO_2 on CuBTC MOF was found to be 25.4 kJ/mol, in which Lennard-Jones interactions contributed with 21.6 kJ/mol. Their calculated value agreed well with the calculated heat of adsorption of experimental isotherm for HT sample reported in Chapter 3 as well as other reported heat of adsorptions in the literature, which clearly indicate physical adsorption, Table 7.2. These results were also confirmed by Ding and Yazaydin [204] where they used DFT calculation for predicting the binding energies of CO_2 on CuBTC MOF, which was found as 21.3 kJ/mol indicating physical adsorption. Another DFT calculations were carried out by Supronowicz *et al.* [157] in which the calculated binding energies of CO_2 on CuBTC MOF was comparable to that calculated by Ding and Yazaydin [204]. Their DFT simulated heat of adsorption indicated physical adsorption similar to most of the reported values, but they found that CO_2 binding with the OMSs of CuBTC framework is stronger than that with the organic linkers.

Since the current work focuses on the pressure region of 1–20 bar, which is commonly used for determining experimental CO_2 adsorption isotherms using either gravimetric or volumetric method, SSAs and the accessible pore volumes of

microporous materials have more profound influence than OMSs on their adsorption capacities over the full pressure range. Therefore, in this work, the effect of OMSs on adsorption isotherms over the full pressure range was considered as insignificant. This assumption on the effect of OMSs on adsorption isotherms is also justified by comparing the available heat of adsorption in the literature (Table 7.2).

Table 7.2
Heat of adsorption of CO_2 on CuBTC MOFs.

Methods of determination	Heat of adsorption (kJ/mol)	Loading (mmol/g)	References
Isosteric heat of adsorption calculated using Clausius-Clayperon equation based on the experimentally measured adsorption isotherms	27	0.1–11.0	This work/ Chapter 3
	25–30	1.0-17.0	Simmons *et al.* [106]
	28	N/A	Cavinati *et al.* [117]
	25	0.04–10.2	Wang *et al.* [98]
	29	0.5–6.0	Ge *et al.* [105]
	29	0.01–10.0	Moellmer *et al.* [118]
Differential heat of adsorption measured by the differential thermal analysis (DTA)	30	N/A	Liang *et al.* [116]
Isosteric heat of adsorption calculated using Monte Carlo simulations based on Canonical (NVT) ensemble	25	N/A	Dickey *et al*. [156]
	22	N/A	Farrusseng *et al.* [210]
Isosteric heat of adsorption measured by the pulse-response experiments in a TAP reactor (temporal analysis of products)	15	N/A	Farrusseng *et al.* [210]

7.4.3 Scenarios of defective CuBTC framework

As discussed above, notwithstanding the similarity of the characterisation (PXRD and SEM) of CuBTC MOFs, there is a big difference in the gravimetrically measured adsorption data at 25 °C as well as in the simulated isotherms (note that OMSs have no significant effect on adsorption at the studied pressure range). Even when one can revise the simulations to match an experimentally measured isotherm by adjusting Lenard-Jones parameters [84] or making the assumption of

the existence of amorphous phases or non-accessible regions in GCMC simulations [208], none of these, individually, can be used to explain the collection of CO_2 adsorption isotherms on CuBTC MOFs that have been reported in the literature. Therefore, the simulated sample can be treated like a real material as a collection of structures containing different defects, and use molecular simulations to determine the adsorption isotherms in the model imperfect structures. The resulting collection of isotherms can be used to assess the quality of experimentally measured adsorption isotherms and the distribution of structural defects required to accurately represent an experimentally measured isotherm can be used as a metric for evaluating the quality of real materials.

Similar approaches have been extensively used in the characterisation of amorphous materials, including activated carbons, porous silica and controlled pore glasses to obtain the pore size distribution, assuming that the materials consist of a collection of idealised pores with a given geometry [211]. Extensions to consider energetic heterogeneity and different pore shapes within a given sample have also been proposed [212]. Herein, a kernel of isotherms for a rigid CuBTC MOF using GCMC simulations has been constructed including defects such as side pocket (SP) and principal pore (PP) blockages (Figure 7.1c), as well as copper vacancies.

7.4.3.1 Side pockets (SPs) blockages

Two scenarios of SP blockages in CuBTC MOF were considered in this study. BTC ligands and solvent molecules can be trapped within the SPs of CuBTC MOF during the synthesis procedure, especially for the fast framework self-assembly under microwave heating. The diameter of a BTC molecule (~7.2 Å) is larger than the connecting windows (~3.5 Å) between the primary pores (PPs) and SPs, and also, the pore opening of SPs of (~5 Å) make the removal of the confined BTC molecules from SPs with a routine work-up sequence impossible. Furthermore, pure BTC ligands are stable up to ~310 °C (Figure 7.5), making it also impossible to remove them from framework at high temperatures without causing the structure's thermal decomposition, and this will create a defect denoted as SP-BTC.

Defective CuBTC MOFs with SP blockage by BTC molecules were modelled by adding one BTC molecule in each SP of original CuBTC MOF structural model. The Lennard-Jones parameters from Table 7.1 were used for the CuBTC MOF structure. The partial charges of a free BTC molecule trapped in the SP were calculated using charge equilibration method (QEq) [213], Table 7.3.

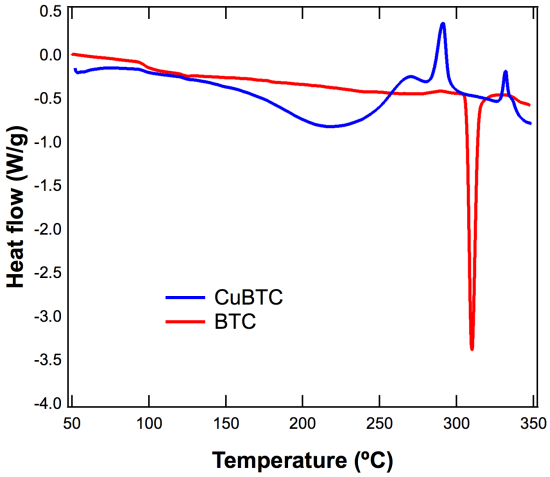

Figure 7.5. DSC curves of CuBTC MOF (blue) and benzene-1,3,5 tricarboxylic acid (red).

Table 7.3
Partial charges on a BTC molecule.

Element	Charge	No. of atoms in one BTC
Oxygen in carboxylic group (O1)	−0.409	3
Carbon in carboxylic group (C1)	0.636	3
Carbon of benzene-C (connected to carboxylic	0.035	3
Carbon of benzene-H (C3)	−0.115	3
Hydrogen in carboxylic group (H1)	0.286	3
Oxygen in carboxylic group (connected to hydrogen,	−0.609	3
Hydrogen in benzene (H2)	0.176	3

Models with SPs blocked by dummy atoms were also created to represent the scenarios of blocked SPs with the agglomeration of other molecules (*e.g.* reactants, solvents and impurities) that were failed to be removed by activation or the crystal collapse, which represented by dummy atoms and denoted as SP-Dummy. Such dummy atoms are modelled as hard spheres (5 Å diameter) without interaction with CO_2 molecules. The defective structures with SP blockages were

then used for GCMC simulation of pure CO_2 adsorption using the method described above in section 7.3.1. The results of SP blockages scenarios are shown in Figure 7.6.

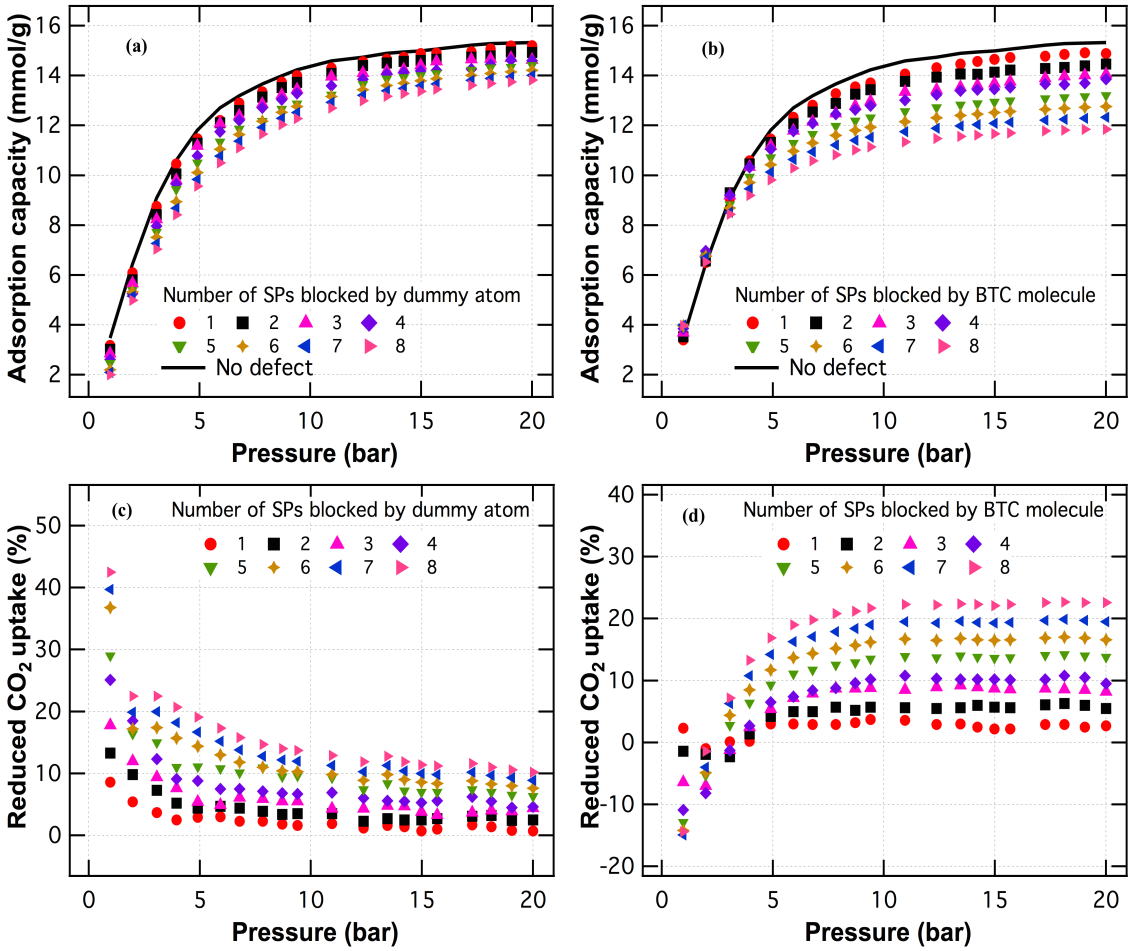

Figure 7.6. Simulated effects of the SP blockage with (a) Dummy atoms and (b) BTC ligands on CO_2 adsorption isotherms of defective CuBTC MOF. (c) and (d) Reduction in CO_2 uptakes of defective CuBTC MOF as function of numbers of blocked SPs.

It was found that the nature of the blockage has an important effect on the adsorption isotherms. SP-Dummy blockages reduce the accessible volume leading to an excluded volume effects. The reduction in the amount adsorbed is more pronounced at low pressures where it can be up to 40% less than in a perfect crystal, and converges at high pressures to a reduction in the amount adsorbed of 10% when all SP are blocked with dummy atoms, Figure 7.6b and d. The larger effect observed at low pressures is because SPs are the preferential adsorption sites in CuBTC MOF for CO_2 adsorption due to their strong electrostatic fields [48, 108] and the dummy atoms in the SPs block the most favourable adsorption sites at low pressures.

SP-BTC blockages only reduce the CO_2 uptake of CuBTC MOFs at high pressures, reaching a reduction in capacity of 20% when all the SP are blocked due to their larger size compared to the solvent molecules used in SP-Dummy. Nevertheless, adsorption increases slightly at low pressures due to the favourable interactions between the carboxylate groups and CO_2. At the lowest pressure simulated in this work, a 15% increase in adsorption is observed when all SP are blocked with BTC molecules. The increase in the amount adsorbed at low pressures is proportional to the number of BTC molecules blocking the SPs. This trend is reversed at high pressures, where the available pore volume dictates the adsorption capacity, Figure 7.6a and c. Figure 7.7 presents the positions of CO_2 molecules in each case of SP blocked, which clearly shows the aggregation of CO_2 molecules near the carboxylate groups of trapped BTC molecule and the excluded volume of dummy atom.

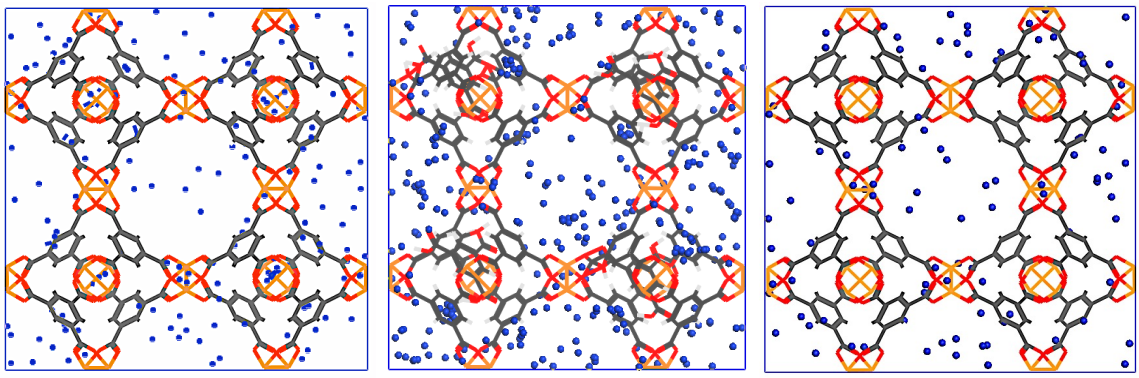

Figure 7.7. Positions of CO_2 centre of mass adsorbed molecules compiled from 20 snapshots obtained once the system reached equilibrium, for a perfect CuBTC MOFs and two defective structures, one containing 100% SP blocked with BTC molecules, and the other containing 100% of SP blocked with dummy atoms, at 1 bar and 25 °C.

Blockage of all SPs cannot explain experimentally measured CO_2 adsorption isotherms where the amount adsorbed is less than 80% of that predicted for an ideal sample, as is the case of our MW sample and other reported in the literature [47, 98, 117]. Therefore, a case of blocking the principal pores (PPs) by precursors or by-products that cannot be removed during the sample work-up and activation was also considered.

7.4.3.2 Primary pores (PPs) blockages

The same method of using dummy atoms was employed to block the available primary pores (PPs) in CuBTC MOF models representing the defective MOF structures with inaccessible PPs. Principal pores' blockages that would result from defects during the synthesis due to retained solvent molecules or crystal collapse rather than the work-up, are denoted as PP-Dummy. In this scenario, a single trapped BTC molecule in PPs was not considered, since the openings of PPs in CuBTC MOF are large enough (~11 Å and ~13.5 Å) to allow the removal of a single BTC molecule through the washing process. Dummy atoms with 11 Å diameter were added in the original CuBTC MOF structural model (one dummy per each PP). The defective models with PP blockage were then used for GCMC simulation of pure CO_2 adsorption using the method described above in section 7.3.1. In this case, two unit cells were used to yield wide distribution of adsorption isotherms between the lowest and highest adsorption isotherms of the blocked PP structures, Figure 7.8.

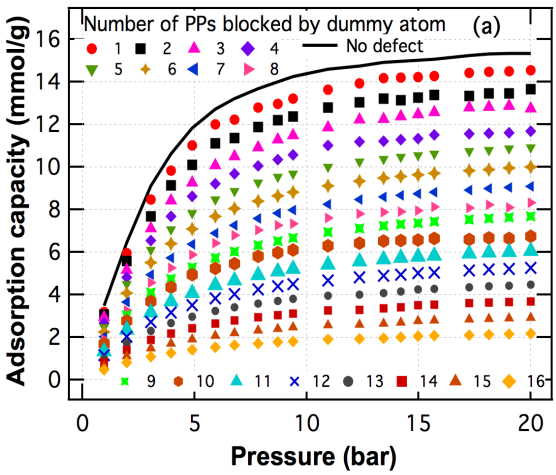

Figure 7.8. Simulated effects of the PPs blockage on CO_2 adsorption isotherms of defective CuBTC MOFs.

It can be seen from Figure 7.8 that, when all PPs are blocked, the amount adsorbed at high pressures is only 14% of the amount adsorbed in the perfect crystal. It should be noted that diffusion limitations due to pore blockages have not been considered, but it is expected that this would only affect the systems where all PP are blocked, as it is the only case where access to the SP is hindered.

7.4.3.3 Missing of copper atoms from CuBTC MOF structure

Another type of defect that may exist in MOFs is the absence of some metal centres from the framework of MOFs, which may be generated during the materials synthesis. For CuBTC MOF, the percentage of copper vacancy defects can be up to 0.57% and they mainly affect their neighbouring carbon and oxygen atoms [214], according to Eq 7.2. In order to reflect such structural imperfection, two copper atoms were removed from the original CuBTC MOF structural model assuming that the BTC ligands did not deprotonate during the synthesis. Removal of two copper atoms from a unit cell leads to a *ca.* 4% of copper vacancy, which is much higher than that estimated by experimental work [214].

$$\%\ \text{of defects} = {}^{N_{\text{missing}}}\!\!\diagup\!\!_{N_{\text{total}}} \times 100 \tag{7.2}$$

where N_{missing} is the number of missing copper atoms and N_{total} is the total number of copper atoms in a perfect unit cell of CuBTC MOF.

Table 7.4
Partial charges on one unit cell of defective CuBTC MOF with two copper vacancies.

Element	Charge	No. of atoms in one defective unit cell with two missing copper atoms
In framework		
Copper (Cu)	1.098	46
Oxygen (O1)	−0.665	184
Carbon in carboxylic group (C1)	0.778	92
Carbon of benzene-C (connected to carboxylic group, C2)	−0.092	96
Carbon of benzene-H (C3)	−0.014	96
Hydrogen (H1)	0.109	96
Near copper vacancies/in uncoordinated BTC ligands		
Oxygen in carboxylic group (connected to hydrogen, O2)	−0.609 (−0.593)*	4
C in carboxylic group (C4)	0.729 (0.679)*	4
H in carboxylic group (H2)	0.286 (0.290)*	4
Oxygen in carboxylic group (O3)	−0.409 (−0.376)*	4

*Value in the brackets is calculated by QEq method, other is adjusted and used in the simulation.

The partial charges of the newly added hydrogen atoms and the neighbouring carboxylate groups were calculated using QEq method. The calculated partial charges were then adjusted (using the charges of the removed copper atoms) in order to make the charges of the full framework zero for applying Ewald summation, where the adjustment made them comparable to those of free BTC except that of carbon. Details of redistributed partial charges in a defective CuBTC MOF model with copper vacancies are given in Table 7.4.

Rigid structure defective CuBTC MOF model was assumed in simulation work. The defective models with copper vacancies were then used for GCMC simulation of pure CO_2 adsorption using the method described in section 7.3.1.

It has been found that the influence of copper vacancies on CO_2 adsorption on CuBTC MOF is negligible, Figure 7.9, which is expected to some extent considering that simulations reported in the literature indicated that the most favourable adsorption site for CO_2 are the SP and not near the copper centres [48, 108]. Nevertheless, this is a controversial point as the accurate simulation of open metal sites is not trivial as discussed above.

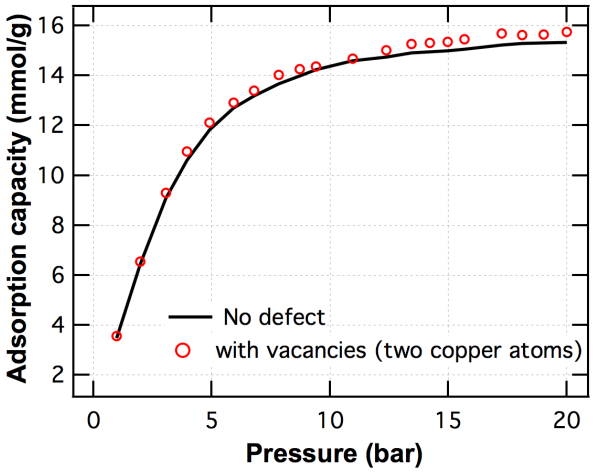

Figure 7.9. Simulated effects of the missing metal sites on CO_2 adsorption isotherms of defective CuBTC MOFs.

7.4.4 Surface area of defective CuBTC framework

The GCMC simulation of N_2 adsorption (at –196 °C, pressure range of 0.001 mar to 1 bar) on the original and defective CuBTC MOF models were also performed to estimate the relevant specific surface areas (SSAs) and accessible surface areas.

CuBTC MOF models described in section 7.4.3 were used in this simulation campaign without further modification. Lennard-Jones parameters for N_2 were taken from TraPPE-EH [206] force field with a probe molecule (diameter = 3.681 Å) [215].

The SSAs were calculated using N_2 adsorption isotherms computed by GCMC simulations and the Brunauer–Emmett–Teller (BET) method, as described in literature [207, 215]. The accessible surface area, which is the theoretical upper limit of the crystal's surface area of a MOF model, has been calculated using a Fortran program developed by Duren *et al.* [215]. The calculated SSAs and accessible surface areas of various CuBTC MOF models are presented in Figure 7.10. The high pressure capacity (20 bar) correlates with the accessible and specific surface areas as seen in Figure 7.11. Both Figure 7.10 and 7.11 show that the decrease in the adsorption capacity of CO_2 is proportional to the size of trapped molecule in SPs or PPs.

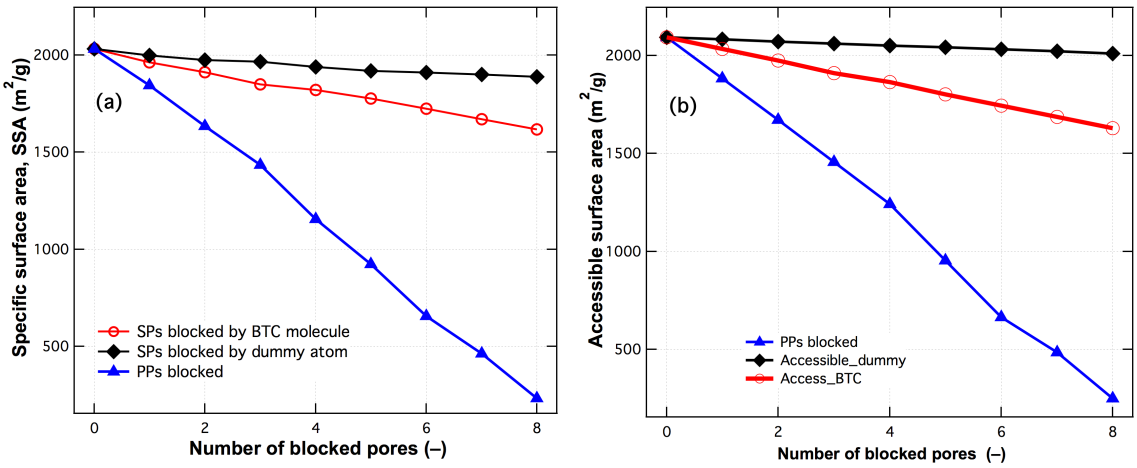

Figure 7.10. (a) Calculated SSAs based on GCMC simulation of N_2 adsorption on one unit cell of different CuBTC MOF models; (b) Calculated accessible surface areas based on different CuBTC MOF models.

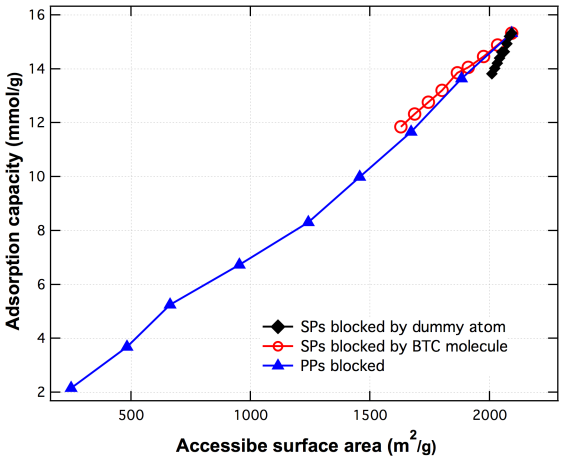

Figure 7.11. Adsorption capacity of pure CO_2 at 20 bar on CuBTC MOFs as function of their accessible surface areas at 20 bar.

7.4.5 Assessment of structural qualities of the experimental samples based on defective CuBTC frameworks

It can be seen from the above defective scenarios that pores blockages are the primary causes of the variation in the reported SSAs and CO_2 adsorption isotherms for CuBTC MOF and the potential effect of copper vacancies in the adsorption isotherm can be neglected.

Using the collection of adsorption isotherms generated, a metric to assess the structural quality of real materials has been proposed borrowing some ideas from the characterisation of amorphous porous materials [202, 216]. The new amount adsorbed measured experimentally $N_{new.}(P,T)$ at temperature (T) and pressure (P) is the weighted sum of all calculated adsorption isotherms with perfect and defective CuBTC MOF structures $N_{sim.i}(P,T)$, and the weight f_i represents the fraction of the material that can be represented by the simulation box containing i defects (either SPs or PPs blockages):

$$N_{new.}\left(P,T\right)=\sum_{i=0}^{n} f_i N_{\mathrm{sim.},i}\left(P,T\right) \tag{7.3}$$

The values of f_i for a given experimentally measured isotherm can be obtained by minimising the error in Eq 7.3 for the full isotherm. The error (weighted sum of squared residuals) between the new calculated experimental isotherm and the actually measured one has been minimised using Excel Solver (χ^2 (f), Eq 7.4).

$$\chi^2(f) = \sum_{i=1}^{n} \frac{\left(N_{\text{exp.}}(P,T) - f_i N_{\text{sim.},i}(P,T)\right)^2}{N_{\text{exp.}}(P,T)} \tag{7.4}$$

It must be noted that the quality of this assessment depends on the accuracy of the simulation, and on having linearly independent isotherms in the collection. It is evident that isotherms with SP-BTC blockages are linearly independent because the isotherms cross over. Nevertheless, the isotherms calculated using dummy atoms for blocking SPs or PPs are linearly dependent, and the same quality of fit can be obtained using different combinations of them. Therefore only isotherms of the materials with the largest number of pores blocked with dummy were used in Eq 7.3. Once the error is minimised, the distribution of possible structural defects can be established indicating the structural quality of the MOF used experimentally as shown in Figure 7.12 and Table 7.5.

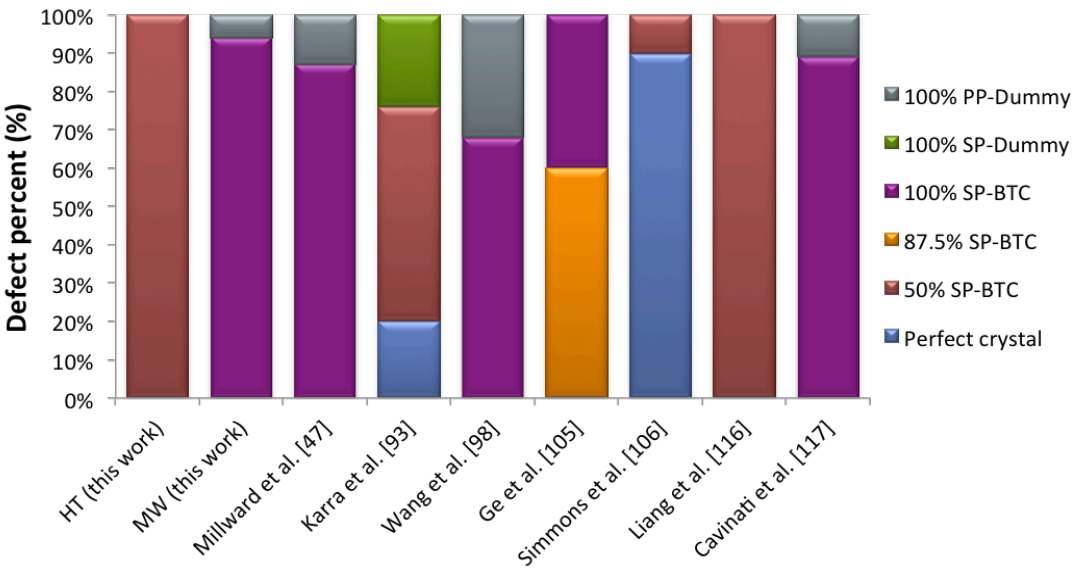

Figure 7.12. Sample quality assessment for selected materials obtained using 11 calculated isotherms: one for a perfect crystal, one with 100% of PP blocked with dummy molecules, one with 100% of SP blocked with dummy molecules, and eight containing different proportions of SP blocked with BTC molecules.

Table 7.5

Distribution of pore blockages for CuBTC MOFs synthesised in this study and reported in literatures.

Materials	Synthesis Method (Temp)	Isotherm measured by[a]	Microstructural characteristics of materials						
			No defects	% of SPs blocked with BTC molecules				100% SPs blocked with dummy	100% PPs blocked
				50	75	87.5	100		
HT	HT (100 °C)	Grav.		100%					
MW	MW (170 °C)	Grav.					94%		6%
Millward *et al.*[47]	HT (85 °C)	Grav.					87%		13%
Karra *et al.* [93]	HT (130 °C)	Grav.	20%	56%				24%	
Wang *et* al. [98]	HT (150 °C)	Vol.					68%		32%
Ge *et al*. [105]	HT (100 °C)	Grav.				60%	40%		
Simmons *et al.* [106]	HT (110 °C)	Vol.	90%	10%					
Liang *et al*. [116]	HT (140 °C)	Grav.		23%	77%				
Cavinati *et al.*[117]	HT (110 °C)	Grav.					89%		11%

[a]Grav.: Gravimetric method; Vol.: Volumetric method.

According to the above defect distribution assessment, SPs blocked by BTC ligands are the main structural defects in the two MOF samples prepared in this study, with 50% of the SPs blocked in the material prepared by HT, and nearly all SPs are blocked with BTC molecules for the material synthesised using the MW method. This can explain the difference in SSAs of the two samples and is consistent with the hypothesis of trapping BTCs in SPs due to the fast crystallisation under microwave heating. The pore blockage by solvents was insignificant for the MOFs prepared in-house due to the meticulous work-up and activation procedure used in this study, but can be significant in other samples reported in the literature. The CuBTC MOF with the highest quality is the one prepared by Simmons *et al.* [106] with 94% of framework corresponding to a perfect crystal and only a small fraction of SPs blocked.

7.5 *Conclusions*

In this Chapter, the result of the defect assessment presents a new generic method that is capable of providing the molecular insight into the structural quality of MOFs based on molecular modelling. It has been shown that molecular simulations can be used to generate collections of hypothetical and well-

characterised MOF models and relevant adsorption isotherms, which can be used to assess the quality of experimentally prepared materials in-house.

It has been focused on the pore blockages originated from materials synthesis and preparation as the main structural defects for the reduced SSAs and the resulting lowered CO_2 uptakes, but the same concepts can be applied for any type of defects. Evidently, the accuracy of the results obtained using Eq 7.3 depend on the quality of the calculated isotherms in different structures, and the use of different force fields can lead to variations in the assessment of the individual sample's quality, but despite the uncertainty in the simulated isotherms, applying the approach presented in this Chapter can aid in the reconciliation of differences in experimentally measured isotherms on independently prepared samples.

Based on GCMC simulations of CO_2 at 25 ºC and N_2 at –196 ºC on perfect and defective structures of CuBTC MOFs, it was found that the main cause of inconsistent CO_2 adsorption isotherms and SSAs is the blocked pores, either with solvent or reactant molecules that depend on synthesis and work-up procedure. Missing copper atoms from the core structure of CuBTC MOF was found to have a negligible effect on adsorption isotherms results, in the case of no effect of OMSs was taken into account.

Though only a case study of CuBTC MOF was considered, the method demonstrated in this study is generic and can be applied to other porous materials helping to assess the structural quality of materials based on their experimentally measured isotherms.

Chapter 8

Summary and recommendations for future work

The necessity of CO_2 capture for combating the global warming and climate change is a growing consensus from multiple studies. Though various CO_2 capture technologies have been proposed so far, the adsorption process is believed to be able to tackle the CO_2 capture in an efficient and cost-effective way. Metal organic frameworks (MOFs) have been considered as new alternative adsorbents with interesting properties for gases and liquids separation applications, especially for CO_2 capture, *i.e.* the large surface area and tunable porous structure and surface chemistry. Moving forward from the conceptual step towards the application step, serious studies for evaluating the suitability of MOFs for CO_2 capture need to be performed not only on lab-scale, but also on process scale under realistic conditions. A combination of computational study with experimental investigation is advantageous since it reduces the effort needed for experimentation and serves as a valuable tool to obtain the crucial in-depth information that is either difficult or impossible to be collected from experiments. Throughout this work, experiments, as well as molecular and process simulation studies were used to evaluate CuBTC MOF as an adsorbent for developing a better understanding of its suitability for CO_2 capture application (mainly from flue gas emissions) as shown in Figure 8.1.

To evaluate a specific MOF for an application, it is necessary to ensure its availability and quality for the accurate assessment of its property and performance. Though CuBTC MOF is a well-studied MOF in the literature, the majority of the available synthesis protocols suffers from either the long reaction time or the by-product formation, and hence the low product yield as discussed in **Chapter 3**. By tailoring the operating conditions (in terms of reaction temperature and time), the synthesis of high purity CuBTC MOF with the yield of 89.4% and

reduction in reaction time by > 92% was achieved in this study by using batch process.

Exploration of new methods such as microwave, ultrasonic or electrochemical techniques for synthesis of CuBTC MOF can be considered for future studies with careful evaluation of the required synthesis cost, product yield and the opportunity of its applicability at large scale. Further investigation is needed to understand the equilibrium dynamics between the crystallised MOFs and the MOFs that remain in the solution for optimising the synthesis of MOFs under hydrothermal conditions.

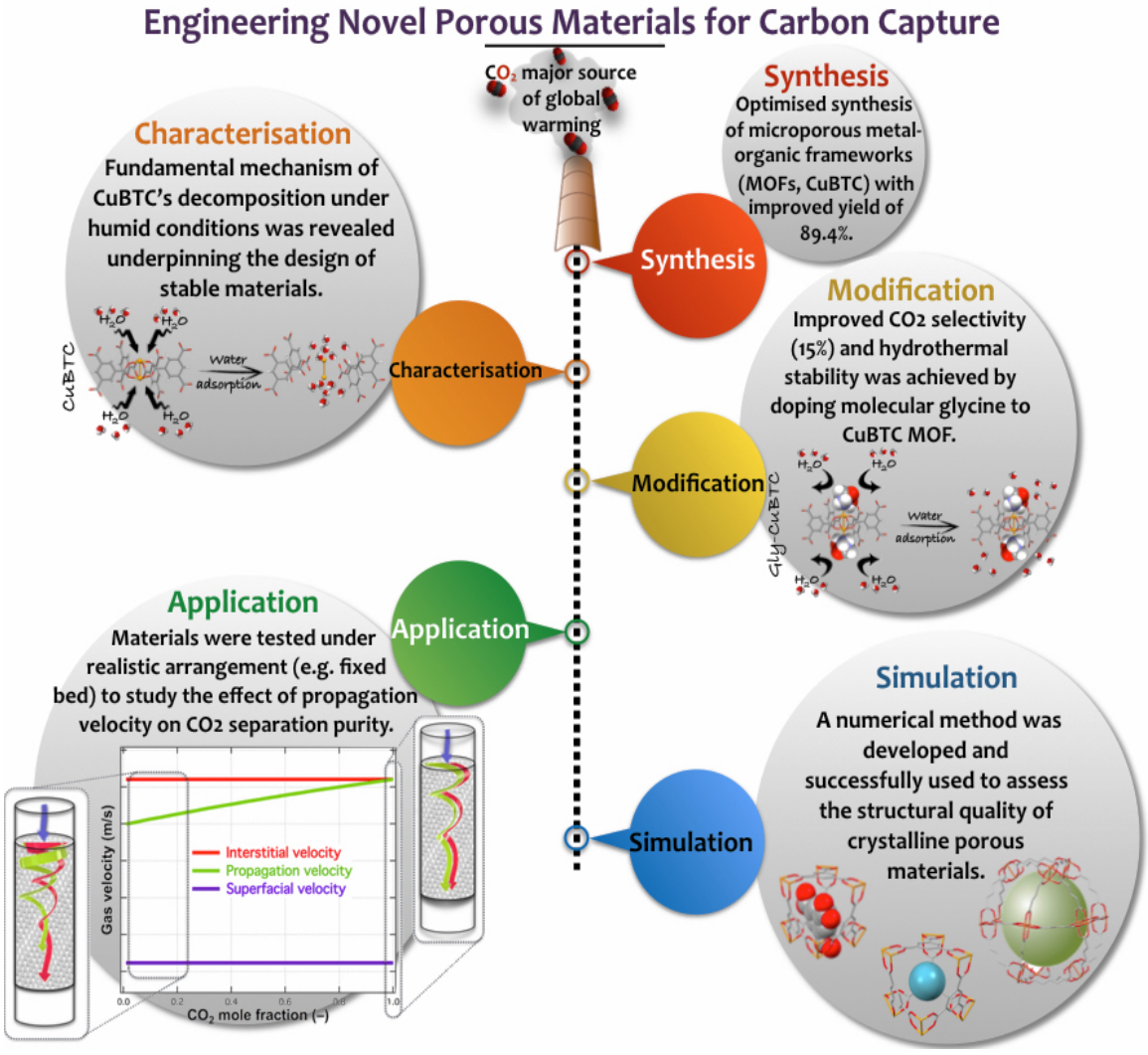

Figure 8.1. Summary of the overall project of this PhD research for evaluating microporous CuBTC MOF for CO_2 capture.

Considering the hydrothermal stability issue of an adsorbent in its storage and application, water vapour adsorption on CuBTC MOF and the post-adsorption characterisation were performed and presented in **Chapter 4**. CuBTC MOF was found unstable hydrothermally at room temperature as well as at high temperatures (50 ºC). Comprehensive characterisation was carried out and revealed the mechanism of how the water molecules destroy the rigid structure of CuBTC MOF. A study was also carried out to investigate the effect of the pre-treatment of materials and process conditions on the lifetime of the material at humid conditions. Research results suggested that further investigation into the effect of the exposure time to water vapour and the degree of hydration of CuBTC material prior to the measurement on the structure stability might be useful to design the process based on CuBTC MOFs for handling humid streams. It may, for example, be used to develop the standard procedure of testing MOFs with open metal sites (OMSs) for water vapour adsorption and suggest the recommendation on the suitable conditions that can be used in the application of MOFs.

Considering the hydrothermal stability issue of CuBTC MOF under humid conditions, a method of insulating the OMSs in CuBTC MOF from water vapour adsorption was worthy of being developed. A facile method of preventing water molecules absorption and aggregation on the unsaturated copper centres by a functional molecular dopant (Glycine) was discussed in **Chapter 5**. The glycine-modified CuBTC (Gly-CuBTC) MOFs was prepared successfully using the developed post-synthetic method and showed satisfactory hydrothermal stability under humid conditions. In addition, the CO_2 adsorption capacity and selectivity of CO_2/N_2 were found to depend on the doping amount of molecular glycine in the CuBTC MOF. This work developed a simple, economical yet generic modification method that could be applicable to improve the hydrothermal stability of other MOFs with OMSs. Moreover, the cyclic water vapour adsorption investigation can be considered for a future research to determine the stability envelope of Gly-CuBTC MOFs under variable humid conditions. A mixture of CO_2, N_2 and water vapour can also be tested to show the effect of competitive adsorption of the three compounds on the adsorption capacity, selectivity and hydrothermal stability of Gly-CuBTC MOFs.

The evaluation of the solid adsorbents for CO_2 capture using equilibrium adsorption needs to be complemented by the fixed bed adsorption, since the latter is the common configuration for designing industrial scale processes, as discussed in **Chapter 6**. The effect of the propagation velocity of mass transfer zone on the breakthrough curves of CO_2 adsorption (on bulk activated carbon, bulk and pelleted CuBTC MOFs) was studied in details using a combined experimental and numerical approach. The CO_2 concentration was found to have a significant effect on the propagation velocity across the adsorption column, and hence the derived adsorption isotherm and the purity of concentrated feed containing CO_2. The comparison of isotherms from the equilibrium adsorption and the fixed bed breakthrough measurements revealed the difference between the equilibrium adsorption capacity and that under practical conditions, showing the necessity of including the breakthrough measurements in assessing porous materials for adsorption process design.

Based on GCMC molecular simulation, **Chapter 7** presented a method that is capable of quantifying the defective characteristics of porous crystalline materials. This work was motivated by the observed variation in CO_2 adsorption capacity of CuBTC MOFs found in the literature as well as prepared in this work (using different methods). The discrepancy in the adsorption data of CuBTC MOFs suggested that that structural defects originated from different synthesis and work-up practices of sample preparation might be the main reason. For porous crystalline materials such as MOFs, different defective structural models can be constructed, and hence the associated adsorption isotherms can be achieved by GCMC molecular simulation. With a full collection of isotherms of various defective scenarios, a metric was developed to quantify the fraction of the defective structures in the model CuBTC MOF by comparing the simulated isothermals against the experimentally measured ones. This study demonstrated the possibility of using molecular simulation to gain insight into the structural details of materials. Though only CuBTC MOF was employed in this work as the model material, the method developed is generic and could be applicable to other porous crystalline materials. Therefore, further evaluation of the developed method is recommended to assess its applicability to other porous crystalline materials used in gas adsorption and separation.

Generally, for the application of MOFs for CO_2 capture, the evaluation of materials using the life cycle assessment (LCA) method is highly suggested since the manufacture of MOFs does have a significant carbon footprint, as well as environmental impact (based on available information of laboratory scale and industrial scale synthesis of MOFs). For example, for CO_2 capture using MOFs, the appropriate LCA will help to quantify the amount of CO_2 released during the synthesis, work-up, regeneration or disposal of MOFs in comparison to the amount of CO_2 captured by the MOFs, showing the trade-off of CO_2 release and capture. The LCA analysis of MOFs will add another dimension to the research on MOFs and provided the fair evaluation of materials and the related application as a whole.

In summary, MOFs have been considered as the promising alternative materials for gas adsorption and separation. The research and methods presented in this thesis will contribute to the development and evaluation of MOFs for their application in practical settings in the future.

References

[1] R. Sabouni, H. Kazemian, S. Rohani, Carbon dioxide capturing technologies: a review focusing on metal organic framework materials (MOFs), Environmental Science and Pollution Research 21 (2014) 5427.

[2] A.-H. Lu, G.-P. Hao, Porous materials for carbon dioxide capture, Annual Reports Section" A"(Inorganic Chemistry) 109 (2013) 484.

[3] M.K. Mondal, H.K. Balsora, P. Varshney, Progress and trends in CO_2 capture/separation technologies: A review, Energy 46 (2012) 431.

[4] James Hansen, Makiko Sato, Pushker Kharecha, David Beerling, Robert Berner, Valerie Masson-Delmotte, Mark Pagani, Maureen Raymo, Dana L. Royer, J.C. Zachos, Target atmospheric CO_2 - Where should humanity aim?, The Open Atmospheric Science Journal 2 (2008) 217.

[5] J. Wilcox, Carbon Capture, Springer New York 2012.

[6] C.-H. Yu, C.S. Tan, A review of CO_2 capture by absorption and adsorption, Aerosol and Air Quality Research 12 (2012) 745.

[7] R. Willis, Paris 2015: Getting a global agreement on climate change, Green Alliance, London, 2014.

[8] IPCC, 2014: Climate Change 2014: Synthesis Report. Contribution of Working Groups I, II and III to the Fifth Assessment Report of the Intergovernmental Panel on Climate Change [Core Writing Team, R.K. Pachauri and L.A. Meyer (eds.)]. IPCC, Geneva, Switzerland, 1-151.

[9] Global CCS Ins tute (2015), The global status of CCS: 2014, Global CCS Institute, Melbourne, Australia.

[10] K.M. Yu, I. Curcic, J. Gabriel, S.C. Tsang, Recent advances in CO_2 capture and utilization, ChemSusChem 1 (2008) 893.

[11] J.-R. Li, Y. Ma, M.C. McCarthy, J. Sculley, J. Yu, H.-K. Jeong, P.B. Balbuena, H.-C. Zhou, Carbon dioxide capture-related gas adsorption and separation in metal-organic frameworks, Coordination Chemistry Reviews 255 (2011) 1791.

[12] D. Aaron, C. Tsouris, Separation of CO_2 from flue gas: A review, Separation Science and Technology 40 (2005) 321.

[13] M. Songolzadeh, M. Soleimani, M. Takht Ravanchi, R. Songolzadeh, Carbon dioxide separation from flue gases: A technological review emphasizing reduction in greenhouse gas emissions, The Scientific World Journal 2014 (2014) 1.
[14] H. Yang, Z. Xu, M. Fan, R. Gupta, R.B. Slimane, A.E. Bland, I. Wright, Progress in carbon dioxide separation and capture: A review, Journal of Environmental Sciences 20 (2008) 14.
[15] Z. Bao, L. Yu, Q. Ren, X. Lu, S. Deng, Adsorption of CO_2 and CH_4 on a magnesium-based metal organic framework, Journal of colloid and interface science 353 (2011) 549.
[16] D. Bonenfant, M. Kharoune, P. Niquette, M. Mimeault, R. Hausler, Advances in principal factors influencing carbon dioxide adsorption on zeolites, Science and Technology of Advanced Materials 9 (2016) 013007.
[17] M. Pera-Titus, Porous inorganic membranes for CO_2 capture: Present and prospects, Chemical Reviews 114 (2014) 1413.
[18] Y. Peng, Y. Li, Y. Ban, H. Jin, W. Jiao, X. Liu, W. Yang, Metal-organic framework anosheets as building blocks for molecular sieving membranes, Science 346 (2014) 1356.
[19] S.S. Chui, S.M.-F. Lo, J.P.H. Charmant, A.G. Orpen, I.D. Williams, A chemically functionalizable nanoporous material $[Cu_3(TMA)_2(H2O)_3]_n$, Science 283 (1999) 1148.
[20] Y. Yang, P. Shukla, S. Wang, V. Rudolph, X.-M. Chen, Z. Zhu, Significant improvement of surface area and CO_2 adsorption of Cu–BTC via solvent exchange activation, Rsc Advances 3 (2013) 17065.
[21] Y.-R. Lee, J. Kim, W.-S. Ahn, Synthesis of metal-organic frameworks: A mini review, Korean Journal of Chemical Engineering 30 (2013) 1667.
[22] J. Liu, P.K. Thallapally, B.P. McGrail, D.R. Brown, J. Liu, Progress in adsorption-based CO_2 capture by metal-organic frameworks, Chemical Society reviews 41 (2012) 2308.
[23] J. Getzschmann, I. Senkovska, D. Wallacher, M. Tovar, D. Fairen-Jimenez, T. Düren, J.M. van Baten, R. Krishna, S. Kaskel, Methane storage mechanism in the metal-organic framework $Cu_3(btc)_2$: An in situ neutron diffraction study, Microporous and Mesoporous Materials 136 (2010) 50.

[24] V.V. Guerrero, Y. Yoo, M.C. McCarthy, H.-K. Jeong, HKUST-1 membranes on porous supports using secondary growth, Journal of Materials Chemistry 20 (2010) 3938.
[25] O. Farha, J. Hupp, Rational design, synthesis, purification, and activation of metal-organic framework materials, Accounts of Chemical Research 43 (2010) 1166.
[26] Y. Belmabkhout, V. Guillerm, M. Eddaoudi, Low concentration CO_2 capture using physical adsorbents: Are metal–organic frameworks becoming the new benchmark materials?, Chemical Engineering Journal 296 (2016) 386.
[27] D. Farrusseng, Metal-organic frameworks: Applications from catalysis to gas storage, Wiley2011.
[28] A. Samanta, A. Zhao, G.K.H. Shimizu, P. Sarkar, R. Gupta, Post-combustion CO_2 capture using solid sorbents: A review, Industrial & Engineering Chemistry Research 51 (2012) 1438.
[29] R.C. Bansal, M. Goyal, Activated carbon adsorption, CRC Press 2005.
[30] A. Somy, M.R. Mehrnia, H.D. Amrei, A. Ghanizadeh, M. Safari, Adsorption of carbon dioxide using impregnated activated carbon promoted by Zinc, International Journal of Greenhouse Gas Control 3 (2009) 249-254.
[31] M.S. Shafeeyan, W.M.A.W. Daud, A. Houshmand, A. Arami-Niya, Ammonia modification of activated carbon to enhance carbon dioxide adsorption: Effect of pre-oxidation, Applied Surface Science 257 (2011) 3936.
[32] C.-H. Yu, C.-H. Huang, C.-S. Tan, A review of CO_2 capture by absorption and adsorption, Aerosol and Air Quality Research 12 (2012) 745.
[33] N.A. Rashidi, S. Yusupa, L.H. Loong, Kinetic studies on carbon dioxide capture using activated carbon, Chemical Engineering Transactions 35 (2013) 361.
[34] R. Xu, W. Pang, J. Yu, Q. Huo, J. Chen, Chemistry of zeolites and related porous materials: Synthesis and structure, Wiley2009.
[35] R. Chatti, A.K. Bansiwal, J.A. Thote, V. Kumar, P. Jadhav, S.K. Lokhande, R.B. Biniwale, N.K. Labhsetwar, S.S. Rayalu, Amine loaded zeolites for carbon dioxide capture: Amine loading and adsorption studies, Microporous and Mesoporous Materials 121 (2009) 84.
[36] F. Su, S.-C. Kuo, C. Lu, W. Zeng, Adsorption of CO_2 on amine-functionalized Y-type zeolites, Energy & Fuels 24 (2010) 1441.

[37] J.R. Long, O.M. Yaghi, The pervasive chemistry of metal-organic frameworks, Chemical Society reviews 38 (2009) 1213.
[38] H.C. Zhou, J.R. Long, O.M. Yaghi, Introduction to metal-organic frameworks, Chemical Reviews 112 (2012) 673.
[39] O.K. Farha, I. Eryazici, N.C. Jeong, B.G. Hauser, C.E. Wilmer, A.A. Sarjeant, R.Q. Snurr, S.T. Nguyen, A.O. Yazaydin, J.T. Hupp, Metal-organic framework materials with ultrahigh surface areas: is the sky the limit?, Journal of the American Chemical Society 134 (2012) 15016.
[40] Q. Liu, L. Ning, S. Zheng, M. Tao, Y. Shi, Y. He, Adsorption of carbon dioxide by MIL-101(Cr): Regeneration conditions and influence of flue gas contaminants, Scientific Reports 3 (2013) 2916.
[41] D.J. Tranchemontagne, J.R. Hunt, O.M. Yaghi, Room temperature synthesis of metal-organic frameworks: MOF-5, MOF-74, MOF-177, MOF-199, and IRMOF-0, Tetrahedron 64 (2008) 8553.
[42] Zhenxia Zhao, Z. Li, a.Y.S. Lin, Adsorption and diffusion of carbon dioxide on metal-organic framework (MOF-5), Industrial & Engineering Chemistry Research 48 (2009) 10015.
[43] H.-Y. Cho, D.-A. Yang, J. Kim, S.-Y. Jeong, W.-S. Ahn, CO_2 adsorption and catalytic application of Co-MOF-74 synthesized by microwave heating, Catalysis Today 185 (2012) 35.
[44] D.-A. Yang, H.-Y. Cho, J. Kim, S.-T. Yang, W.-S. Ahn, CO_2 capture and conversion using Mg-MOF-74 prepared by a sonochemical method, Energy & Environmental Science 5 (2012) 6465.
[45] D.W. Jung, D.A. Yang, J. Kim, J. Kim, W.S. Ahn, Facile synthesis of MOF-177 by a sonochemical method using 1-methyl-2-pyrrolidinone as a solvent, Dalton Transactions 39 (2010) 2883.
[46] S. Cavenati, C.A. Grande, A.E. Rodrigues, Separation of mixtures by layered pressure swing adsorption for upgrade of natural gas, Chemical Engineering Science 61 (2006) 3893.
[47] A.R. Millward, O.M. Yaghi, Metal-organic frameworks with exceptionally high capacity for storage of carbon dioxide at room temperature, Journal of the American Chemical Society 127 (2005) 17998.

[48] Q. Yang, C. Zhong, Molecular simulation of carbon dioxide/methane/hydrogen mixture adsorption in metal-organic frameworks, The Journal of Physical Chemistry B 110 (2006) 17776.
[49] A.O. Yazaydın, A.I. Benin, S.A. Faheem, P. Jakubczak, J.J. Low, R.R. Willis, R.Q. Snurr, Enhanced CO_2 adsorption in metal-organic frameworks via occupation of open-metal sites by coordinated water molecules, Chemistry of Materials 21 (2009) 1425.
[50] S. Ye, X. Jiang, L.-W. Ruan, B. Liu, Y.-M. Wang, J.-F. Zhu, L.-G. Qiu, Post-combustion CO_2 capture with the HKUST-1 and MIL-101(Cr) metal–organic frameworks: Adsorption, separation and regeneration investigations, Microporous and Mesoporous Materials 179 (2013) 191.
[51] S. Surble, F. Millange, Christian Serre, Tina Duren, Michel Latroche, S. Bourrelly, Philip L. Llewellyn, a.G.r. Ferey|, Synthesis of MIL-102, a chromium carboxylate metal-organic framework, with gas sorption analysis, Journal of the American Chemical Society 128 (2006) 14889.
[52] O.M. Yaghi, M. O'Keeffe, N.W. Ockwig, H.K. Chae, M. Eddaoudi, J. Kim, Reticular synthesis and the design of new materials, Nature 423 (2003) 705.
[53] M. Eddaoudi, J. Kim, N. Rosi, D. Vodak, J. Wachter, M. ÕKeeffe, O.M. Yaghi, Systematic design of pore size and functionality in isoreticular MOFs and their application in methane storage, Science 295 (2002).
[54] Y. He, B. Chen, Metal–Organic Frameworks: Frameworks Containing Open Sites, Encyclopedia of Inorganic and Bioinorganic Chemistry (2014).
[55] M. Alhamami, H. Doan, C.-H. Cheng, A Review on breathing behaviors of metal-organic-frameworks (MOFs) for gas ddsorption, Materials 7 (2014) 3198.
[56] R. Poloni, K. Lee, R.F. Berger, B. Smit, J.B. Neaton, Understanding trends in CO_2 adsorption in metal–organic frameworks with open-metal sites, The Journal of Physical Chemistry Letters 5 (2014) 861.
[57] A. Schneemann, V. Bon, I. Schwedler, I. Senkovska, S. Kaskel, R.A. Fischer, Flexible metal-organic frameworks, Chemical Society reviews 43 (2014) 6062.
[58] K.E. Maly, Assembly of nanoporous organic materials from molecular building blocks, Journal of Materials Chemistry 19 (2009) 1781.
[59] J.E. Mondloch, O. Karagiaridi, O.K. Farha, J.T. Hupp, Activation of metal–organic framework materials, CrystEngComm 15 (2013) 9258.

[60] T. Devic, C. Serre, N. Audebrand, J. Marrot, a.G. Ferey, MIL-103, A 3-D Lanthanide-Based Metal Organic Framework with Large One-Dimensional Tunnels and A High Surface Area, Journal of the American Chemical Society 127 (2005) 12788.
[61] I.J. Kang, N.A. Khan, E. Haque, S.H. Jhung, Chemical and thermal stability of isotypic metal-organic frameworks: Effect of metal ions, Chemistry 17 (2011) 6437.
[62] A.U. Czaja, N. Trukhan, U. Muller, Industrial applications of metal-organic frameworks, Chemical Society reviews 38 (2009) 1284.
[63] D. Nunes, L. Santos, P. Duarte, A. Pimentel, J.V. Pinto, P. Barquinha, P.A. Carvalho, E. Fortunato, R. Martins, Room temperature synthesis of Cu_2O nanospheres: Optical properties and thermal behavior, Microsc Microanal 21 (2015) 108.
[64] E. Biemmi, S. Christian, N. Stock, T. Bein, High-throughput screening of synthesis parameters in the formation of the metal-organic frameworks MOF-5 and HKUST-1, Microporous and Mesoporous Materials 117 (2009) 111.
[65] K. Schlichte, T. Kratzke, S. Kaskel, Improved synthesis, thermal stability and catalytic properties of the metal-organic framework compound $Cu_3(BTC)_2$, Microporous and Mesoporous Materials 73 (2004) 81.
[66] W. Kleist, M. Maciejewski, A. Baiker, MOF-5 based mixed-linker metal–organic frameworks: Synthesis, thermal stability and catalytic application, Thermochimica Acta 499 (2010) 71.
[67] J. Li, S. Cheng, Q. Zhao, P. Long, J. Dong, Synthesis and hydrogen-storage behavior of metal–organic framework MOF-5, International Journal of Hydrogen Energy 34 (2009) 1377.
[68] S.H. Jhung, J.H. Lee, J.W. Yoon, C. Serre, G. Férey, J.S. Chang, Microwave synthesis of chromium terephthalate MIL-101 and its Bbenzene sorption ability, Advanced Materials 19 (2007) 121.
[69] Y.-K. Seo, G. Hundal, I.T. Jang, Y.K. Hwang, C.-H. Jun, J.-S. Chang, Microwave synthesis of hybrid inorganic–organic materials including porous Cu3(BTC)2 from Cu(II)-trimesate mixture, Microporous and Mesoporous Materials 119 (2009) 331.
[70] Z.-Q. Li, L.-G. Qiu, W. Wang, T. Xu, Y. Wu, X. Jiang, Fabrication of nanosheets of a fluorescent metal–organic framework $[Zn(BDC)(H2O)]_n$

(BDC=1,4-benzenedicarboxylate): Ultrasonic synthesis and sensing of ethylamine, Inorganic Chemistry Communications 11 (2008) 1375.
[71] Z.-Q. Li, L.-G. Qiu, T. Xu, Y. Wu, W. Wang, Z.-Y. Wu, X. Jiang, Ultrasonic synthesis of the microporous metal–organic framework $Cu_3(BTC)_2$ at ambient temperature and pressure: An efficient and environmentally friendly method, Materials Letters 63 (2009) 78.
[72] R. Sabouni, H. Kazemian, S. Rohani, A novel combined manufacturing technique for rapid production of IRMOF-1 using ultrasound and microwave energies, Chemical Engineering Journal 165 (2010) 966.
[73] W.J. Son, J. Kim, J. Kim, W.S. Ahn, Sonochemical synthesis of MOF-5, Chemical Communications (2008) 6336.
[74] M. Hartmann, S. Kunz, D. Himsl, O. Tangermann, Adsorptive separation of isobutene and isobutane on Cu3(BTC)2, Langmuir 24 (2008) 8634.
[75] R. Senthil Kumar, S. Senthil Kumar, M. Anbu Kulandainathan, Efficient electrosynthesis of highly active $Cu_3(BTC)_2$-MOF and its catalytic application to chemical reduction, Microporous and Mesoporous Materials 168 (2013) 57.
[76] M. Klimakow, P. Klobes, K. Rademann, F. Emmerling, Characterization of mechanochemically synthesized MOFs, Microporous and Mesoporous Materials 154 (2012) 113.
[77] M. Klimakow, P. Klobes, A.F. Thünemann, K. Rademann, F. Emmerling, Mechanochemical synthesis of metal−organic frameworks: A fast and facile approach toward quantitative yields and high specific surface areas, Chemistry of Materials 22 (2010) 5216.
[78] H. Yang, S. Orefuwa, A. Goudy, Study of mechanochemical synthesis in the formation of the metal–organic framework $Cu_3(BTC)_2$ for hydrogen storage, Microporous and Mesoporous Materials 143 (2011) 37.
[79] Z. Li, Z. Jia, Y. Luan, T. Mu, Ionic liquids for synthesis of inorganic nanomaterials, Current Opinion in Solid State and Materials Science 12 (2008) 1.
[80] K. Peikert, F. Hoffmann, M. Fröba, Amino substituted $Cu_3(btc)_2$: A new metal–organic framework with a versatile functionality, Chemical Communications 48 (2012) 11196.
[81] K. Peikert, F. Hoffmann, M. Fröba, Fluorine magic: one new organofluorine linker leads to three new metal–organic frameworks, CrystEngComm 17 (2014) 353.

[82] A. Demessence, D.M. D'Alessandro, M.L. Foo, J.R. Long, Strong CO_2 binding in a water-stable, triazolate-bridged metal-organic framework functionalized with ethylenediamine, Journal of the American Chemical Society 131 (2009) 8784.
[83] Q.-x. Luo, X.-d. Song, M. Ji, S.-E. Park, C. Hao, Y.-q. Li, Molecular size- and shape-selective Knoevenagel condensation over microporous $Cu_3(BTC)_2$ immobilized amino-functionalized basic ionic liquid catalyst, Applied Catalysis A: General 478 (2014) 81.
[84] H. Amrouche, S. Aguado, J. Pérez-Pellitero, C.l. Chizallet, F. Siperstein, D. Farrusseng, N. Bats, C. Nieto-Draghi, Experimental and computational study of functionality impact on sodalite–zeolitic imidazolate frameworks for CO_2 separation, The Journal of Physical Chemistry C 115 (2011) 16425.
[85] R. Vaidhyanathan, S.S. Iremonger, G.K. Shimizu, P.G. Boyd, S. Alavi, T.K. Woo, Direct observation and quantification of CO_2 binding within an amine-functionalized nanoporous solid, Science 330 (2010) 650.
[86] Y. Zhu, Y.M. Wang, S.Y. Zhao, P. Liu, C. Wei, Y.L. Wu, C.K. Xia, J.M. Xie, Three N-H functionalized metal-organic frameworks with selective CO_2 uptake, dye capture, and catalysis, Inorganic chemistry 53 (2014) 7692.
[87] A.R. Leach, Molecular modelling: Principles and applications, Pearson Education 2001.
[88] L.R. MacGillivray, Metal-organic frameworks: Design and application, John Wiley & Sons 2010.
[89] M.G. Martin, MCCCS Towhee: a tool for Monte Carlo molecular simulation, Molecular Simulation 39 (2013) 1212.
[90] M.S. Shafeeyan, W.M.A.W. Daud, A. Shamiri, A review of mathematical modeling of fixed-bed columnsfor carbon dioxide adsorption, Chemical Engineering Research and Design 92 (2014) 961.
[91] U. Jecht, 2004, Flue gas analysis in industry, 2nd ed, USA, TESTO, 16.
[92] C. Lu, H. Bai, B. Wu, F. Su, J.F. Hwang, Comparative study of CO_2 capture by carbon nanotubes, activated carbons, and zeolites, Energy & Fuels 22 (2008) 3050.
[93] J.R. Karra, K.S. Walton, Molecular simulations and experimental studies of CO_2, CO, and N_2 adsorption in metal-organic frameworks, The Journal of Physical Chemistry C 114 (2010) 15735.

[94] M. Schlesinger, S. Schulze, M. Hietschold, M. Mehring, Evaluation of synthetic methods for microporous metal–organic frameworks exemplified by the competitive formation of $[Cu_2(btc)_3(H2O)_3]$ and $[Cu_2(btc)(OH)(H_2O)]$, Microporous and Mesoporous Materials 132 (2010) 121.
[95] S. Brunauer, P.H. Emmett, E. Teller, Adsorption of gases in multimolecular layers, Journal of the American Chemical Society 60 (1938) 309.
[96] I. Langmuir, The constitution and fundamental properties of solids and liquids. Part I. Solids, Journal of the American Chemical Society 38 (1916) 2221.
[97] I. Langmuir, The adsorption of gases on plane surfaces of glass, mica and platinum, Journal of the American Chemical Society 40 (1918) 1361.
[98] Q.M. Wang, D. Shen, M. Bulow, M.L. Lau, Shuguang Deng, F. Fitch, N.O. Lemcoff, J. Semanscin, Metallo-organic molecular sieve for gas separation and purification, Microporous Mesoporous Materials 55 (2002) 217.
[99] L. Alaerts, E. Seguin, H. Poelman, F. Thibault-Starzyk, P.A. Jacobs, D.E. De Vos, Probing the Lewis acidity and catalytic activity of the metal-organic framework [Cu3(btc)2] (BTC=benzene-1,3,5-tricarboxylate), Chemistry 12 (2006) 7353.
[100] J. Liu, J.T. Culp, S. Natesakhawat, B.C. Bockrath, B. Zande, S.G. Sankar, G. Garberoglio, J.K. Johnson, Experimental and theoretical studies of gas adsorption in $Cu_3(BTC)_2$: An effective activation procedure, The Journal of Physical Chemistry C 11 (2007) 9305.
[101] Y. Wu, A. Kobayashi, G.J. Halder, V.K. Peterson, K.W. Chapman, N. Lock, P.D. Southon, C.J. Kepert, Negative thermal expansion in the metal-organic framework material Cu3(1,3,5-benzenetricarboxylate)2, Angewandte Chemie International Edition 47 (2008) 8929.
[102] K.-S. Lin, A.K. Adhikari, C.-N. Ku, C.-L. Chiang, H. Kuo, Synthesis and characterization of porous HKUST-1 metal organic frameworks for hydrogen storage, International Journal of Hydrogen Energy 37 (2012) 13865.
[103] T.E. Bell, J.M. González-Carballo, R.P. Tooze, L. Torrente-Murciano, Single-step synthesis of nanostructured γ-alumina with solvent reusability to maximise yield and morphological purity, Journal of Materials Chemistry A 3 (2015) 6196.
[104] L. Torrente-Murciano, A. Gilbank, B. Puertolas, T. Garcia, B. Solsona, D. Chadwick, Shape-dependency activity of nanostructured CeO_2 in the total oxidation of polycyclic aromatic hydrocarbons, Applied Catalysis B: Environmental 132-133 (2013) 116.

[105] L. Ge, L. Wang, V. Rudolph, Z. Zhu, Hierarchically structured metal–organic framework/vertically-aligned carbon nanotubes hybrids for CO_2 capture, RSC Advances 3 (2013) 25360.
[106] J.M. Simmons, H. Wu, W. Zhou, T. Yildirim, Carbon capture in metal–organic frameworks-a comparative study, Energy & Environmental Science 4 (2011) 2177.
[107] M. Sánchez, J. Rams, A. Ureña, Oxidation mechanisms of copper and nickel coated carbon fibers, Oxidation of Metals 69 (2008) 327.
[108] Q. Yang, C. Xue, C. Zhong, J.F. Chen, Molecular simulation of separation of CO_2 from flue gases in Cu‐BTC metal‐organic framework, AIChE journal 53 (2007) 2832.
[109] A.L. Myers, J.M. Prausnitz, Thermodynamics of mixed-gas adsorption, AIChE Journal 11 (1965) 121.
[110] J.A. O'Brien, A.L. Myers, Rapid calculations of multicomponent adsorption equilibria from pure isotherm data, Industrial & Engineering Chemistry Process Design and Development 24 (1985) 1188.
[111] J.A. Schwarz, C.I. Contescu, Surfaces of nanoparticles and porous materials, CRC Press 1999.
[112] R. Anthony, Encyclopedia of chemical processing and design, Volume 69 (Supplement 1), CRC Press 2001.
[113] Q. Chen, Z. Chang, W.C. Song, H. Song, H.B. Song, T.L. Hu, X.H. Bu, A controllable gate effect in cobalt (II) organic frameworks by reversible structure transformations, Angewandte Chemie International Edition 52 (2013) 11550.
[114] J.J. Low, A.I. Benin, P. Jakubczak, J.F. Abrahamian, S.A. Faheem, R.R. Willis, Virtual high throughput screening confirmed experimentally: porous coordination polymer hydration, Journal of the American Chemical Society 131 (2009) 15834.
[115] D. Crawford, J. Casaban, R. Haydon, N. Giri, T. McNally, S.L. James, Synthesis by extrusion: continuous, large-scale preparation of MOFs using little or no solvent, Chemical Science 6 (2015) 1645.
[116] Z. Liang, M. Marshall, A.L. Chaffee, CO_2 adsorption-based separation by metal organic framework (Cu-BTC) versus zeolite (13X), Energy & Fuels 23 (2009) 2785.

[117] S. Cavenati, C.A. Grande, A.E. Rodrigues, Metal organic framework adsorbent for biogas upgrading, Industrial & Engineering Chemistry Research 47 (2008) 6333.
[118] J. Moellmer, A. Moeller, F. Dreisbach, R. Glaeser, R. Staudt, High pressure adsorption of hydrogen, nitrogen, carbon dioxide and methane on the metal–organic framework HKUST-1, Microporous and Mesoporous Materials 138 (2011) 140.
[119] N.C. Burtch, H. Jasuja, K.S. Walton, Water stability and adsorption in metal-organic frameworks, Chemical Reviews 114 (2014) 10575.
[120] Y. Li, R.T. Yang, Hydrogen storage in metal-organic and covalent-organic frameworks by spillover, AIChE Journal 54 (2008) 269.
[121] J.M. Castillo, T.J.H. Vlugt, S. Calero, Understanding water adsorption in Cu-BTC metal-organic frameworks, The Journal of Physical Chemistry C 112 (2008) 15934.
[122] P. Küsgens, M. Rose, I. Senkovska, H. Fröde, A. Henschel, S. Siegle, S. Kaskel, Characterization of metal-organic frameworks by water adsorption, Microporous and Mesoporous Materials 120 (2009) 325.
[123] J. Liu, Y. Wang, A.I. Benin, P. Jakubczak, R.R. Willis, M.D. LeVan, CO_2/H_2O adsorption equilibrium and rates on metal-organic frameworks: HKUST-1 and Ni/DOBDC, Langmuir 26 (2010) 14301.
[124] K.A. Cychosz, A.J. Matzger, Water stability of microporous coordination polymers and the adsorption of pharmaceuticals from water, Langmuir 26 (2010) 17198.
[125] E.N.F. Gul, B. Jee, A. Poppl, M. Hartmann, D. Himsl, M. Bertmer, Effects of varying water adsorption on a Cu3(BTC)2 metal-organic framework (MOF) as studied by 1H and 13C solid-state NMR spectroscopy, Physical Chemistry Chemical Physics 13 (2011) 7783.
[126] E. Soubeyrand-Lenoir, C. Vagner, J.W. Yoon, P. Bazin, F. Ragon, Y.K. Hwang, C. Serre, J.S. Chang, P.L. Llewellyn, How water fosters a remarkable 5-fold increase in low-pressure CO_2 uptake within mesoporous MIL-100(Fe), Journal of the American Chemical Society 134 (2012) 10174.
[127] A. Rezk, R. Al-Dadah, S. Mahmoud, A. Elsayed, Characterisation of metal organic frameworks for adsorption cooling, International Journal of Heat and Mass Transfer 55 (2012) 7366.

[128] P.M. Schoenecker, C.G. Carson, H. Jasuja, C.J.J. Flemming, K.S. Walton, Effect of water adsorption on retention of structure and surface area of metal–organic frameworks, Industrial & Engineering Chemistry Research 51 (2012) 6513.
[129] F. Gul-E-Noor, D. Michel, H. Krautscheid, J. Haase, M. Bertmer, Time dependent water uptake in $Cu_3(btc)_2$ MOF: Identification of different water adsorption states by 1H MAS NMR, Microporous and Mesoporous Materials 180 (2013) 8.
[130] L. Huang, T. Bandosz, K.L. Joshi, A.C. van Duin, K.E. Gubbins, Reactive adsorption of ammonia and ammonia/water on CuBTC metal-organic framework: a ReaxFF molecular dynamics simulation, The Journal of Chemical Physics 138 (2013) 034102.
[131] J. Toda, M. Fischer, M. Jorge, J.R.B. Gomes, Water adsorption on a copper formate paddlewheel model of CuBTC: A comparative MP2 and DFT study, Chemical Physics Letters 587 (2013) 7.
[132] J. Zang, S. Nair, D.S. Sholl, Prediction of water adsorption in copper-based metal–organic frameworks using force fields derived from dispersion-corrected DFT calculations, The Journal of Physical Chemistry C 117 (2013) 7519.
[133] J.B. DeCoste, G.W. Peterson, B.J. Schindler, K.L. Killops, M.A. Browe, J.J. Mahle, The effect of water adsorption on the structure of the carboxylate containing metal–organic frameworks Cu-BTC, Mg-MOF-74, and UiO-66, Journal of Materials Chemistry A 1 (2013) 11922.
[134] X. Peng, L.-C. Lin, W. Sun, B. Smit, Water adsorption in metal-organic frameworks with open-metal sites, AIChE Journal 61 (2015) 677.
[135] Z. Zhao, S. Wang, Y. Yang, X. Li, J. Li, Z. Li, Competitive adsorption and selectivity of benzene and water vapor on the microporous metal organic frameworks (HKUST-1), Chemical Engineering Journal 259 (2015) 79.
[136] S. Calero, P. Gómez-Álvarez, Insights into the adsorption of water and small alcohols on the open-metal sites of Cu–BTC via molecular simulation, The Journal of Physical Chemistry C 119 (2015) 467.
[137] J.J. Gutiérrez-Sevillano, S. Calero, R. Krishna, Selective adsorption of water from mixtures with 1-alcohols by exploitation of molecular packing effects in CuBTC, The Journal of Physical Chemistry C 119 (2015) 3658.

[138] P.Z. Moghadam, P. Ghosh, R.Q. Snurr, Understanding the effects of preadsorbed perfluoroalkanes on the adsorption of water and ammonia in MOFs, The Journal of Physical Chemistry C 119 (2015) 3163.
[139] M. Razali, J.F. Kim, M. Attfield, P.M. Budd, E. Drioli, Y.M. Lee, G. Szekely, Sustainable wastewater treatment and recycling in membrane manufacturing, Green Chemistry 17 (2015) 5196.
[140] Y.-S. Bae, K.L. Mulfort, H. Frost, P. Ryan, S. Punnathanam, L.J. Broadbelt, J.T. Hupp, R.Q. Snurr, Separation of CO_2 from CH_4 using mixed-ligand metal−organic frameworks, Langmuir 24 (2008) 8592.
[141] A.K. Singh, Advanced x-ray techniques in research and industry, IOS Press, Netherlands, 2005.
[142] S.L. Mayo, B.D. Olafson, W.A. Goddard, The Journal of Physical Chemistry 94 (1990) 8897.
[143] A.K. Rappe, C.J. Casewit, K.S. Colwell, W.A. Goddard, W.M. Skiff, UFF, a full periodic table force field for molecular mechanics and molecular dynamics simulations, Journal of the American Chemical Society 114 (1992) 10024.
[144] M.W. Mahoney, W.L. Jorgensen, The Journal of Chemical Physics 112 (2000) 8910.
[145] M. Shoaee, M.W. Anderson, M.P. Attfield, Crystal growth of the nanoporous metal–organic framework HKUST-1 revealed by in situ atomic force microscopy, Angewandte Chemie International Edition 47 (2008) 8525.
[146] S. Henninger, F. Schmidt, H.-M. Henning, Water adsorption characteristics of novel materials for heat transformation applications, Applied thermal engineering 30 (2010) 1692.
[147] B.M. Klepser, B.M. Bartlett, Anchoring a molecular iron catalyst to solar-responsive WO3 improves the rate and selectivity of photoelectrochemical water oxidation, Journal of the American Chemical Society 136 (2014) 1694.
[148] G.K. Kole, J.J. Vittal, Solid-state reactivity and structural transformations involving coordination polymers, Chemical Society reviews 42 (2013) 1755.
[149] X. Sun, H. Li, Y. Li, F. Xu, J. Xiao, Q. Xia, Y. Li, Z. Li, A novel mechanochemical method for reconstructing the moisture-degraded HKUST-1, Chemical Communications 51 (2015) 10835.
[150] C. Prestipino, L. Regli, J.G. Vitillo, F. Bonino, A. Damin, C. Lamberti, A. Zecchina, P.L. Solari, K.O. Kongshaug, S. Bordiga, Local structure of framework

Cu(II) in HKUST-1 metallorganic framework: Spectroscopic characterization upon activation and interaction with adsorbates, Chemistry of Materials 18 (2006) 1337.
[151] L.T. Nguyen, T.T. Nguyen, K.D. Nguyen, N.T. Phan, Metal–organic framework MOF-199 as an efficient heterogeneous catalyst for the aza-Michael reaction, Applied Catalysis A: General 425 (2012) 44.
[152] E.A. Müller, K.E. Gubbins, Molecular simulation study of hydrophilic and hydrophobic behavior of activated carbon surfaces, Carbon 36 (1998) 1433.
[153] S. Houston, Application note, moisture in natural gas, in: SpectraSensors (Ed.) Industry: Natural gas application SpectraSensors Houston, USA, pp. 1.
[154] M. Fischer, J.R.B. Gomes, M. Jorge, Computational approaches to study adsorption in MOFs with unsaturated metal sites, Mol. Sim. 40 (2014) 537.
[155] S. Bordiga, L. Regli, F. Bonino, E. Groppo, C. Lamberti, B. Xiao, P.S. Wheatley, R.E. Morris, A. Zecchina, Adsorption properties of HKUST-1 toward hydrogen and other small molecules monitored by IR, Physical Chemistry Chemical Physics 9 (2007) 2676.
[156] A.N. Dickey, A.Ö. Yazaydın, R.R. Willis, R.Q. Snurr, Screening CO_2/N_2 selectivity in metal-organic frameworks using Monte Carlo simulations and ideal adsorbed solution theory, The Canadian Journal of Chemical Engineering 90 (2012) 825.
[157] B. Supronowicz, A. Mavrandonakis, T. Heine, Interaction of small gases with the unsaturated metal centers of the HKUST-1 metal organic framework, The Journal of Physical Chemistry C 117 (2013) 14570.
[158] J. Canivet, A. Fateeva, Y. Guo, B. Coasne, D. Farrusseng, Water adsorption in MOFs: Fundamentals and applications, Chemical Society reviews 43 (2014) 5594.
[159] Y. Cai, Y. Zhang, Y. Huang, S.R. Marder, K.S. Walton, Impact of alkyl-functionalized BTC on properties of copper-based metal–organic frameworks, Crystal Growth & Design 12 (2012) 3709.
[160] Y. Cai, A.R. Kulkarni, Y.-G. Huang, D.S. Sholl, K.S. Walton, Control of metal–organic framework crystal topology by ligand functionalization: functionalized HKUST-1 derivatives, Crystal Growth & Design 14 (2014) 6122.
[161] N. Ko, J. Hong, L. You, H.J. Park, J.K. Yang, J. Kim, Chemical property change in a metal-organic framework by fluoro functionality, Bulletin of the Korean Chemical Society 36 (2015) 327.

[162] J.B. Decoste, G.W. Peterson, M.W. Smith, C.A. Stone, C.R. Willis, Enhanced stability of Cu-BTC MOF via perfluorohexane plasma-enhanced chemical vapor deposition, Journal of the American Chemical Society 134 (2012) 1486.
[163] W. Zhang, Y. Hu, J. Ge, H.L. Jiang, S.H. Yu, A facile and general coating approach to moisture/water-resistant metal-organic frameworks with intact porosity, Journal of the American Chemical Society 136 (2014) 16978.
[164] Y.K. Hwang, D.Y. Hong, J.S. Chang, S.H. Jhung, Y.K. Seo, J. Kim, A. Vimont, M. Daturi, C. Serre, G. Ferey, Amine grafting on coordinatively unsaturated metal centers of MOFs: Consequences for catalysis and metal encapsulation, Angewandte Chemie International Edition 47 (2008) 4144.
[165] Y. Cao, F. Song, Y. Zhao, Q. Zhong, Capture of carbon dioxide from flue gas on TEPA-grafted metal-organic framework Mg2(dobdc), Journal of Environmental Sciences 25 (2013) 2081.
[166] N.R. Dhumal, M.P. Singh, J.A. Anderson, J. Kiefer, H.J. Kim, Molecular interactions of a Cu-based metal–organic framework with a confined imidazolium-based ionic liquid: A combined density functional theory and experimental vibrational spectroscopy study, The Journal of Physical Chemistry C 120 (2016) 3295.
[167] S. Kumar, A.K. Rai, V.B. Singh, S.B. Rai, Vibrational spectrum of glycine molecule, Spectrochimica Acta Part A: Molecular and Biomolecular Spectroscopy 61 (2005) 2741.
[168] J.A. O'Brlen, A.L. Myers, Rapid calculations of multicomponent adsorption equilibria from pure isotherm data, Industrial & Engineering Chemistry Process Design and Development 24 (1985) 1188.
[169] G. Brecht, R.B. Corey, The crystal structure of glycine, Journal of the American Chemical Society 61 (1939) 1087.
[170] C. Graham, J. Pierrus, R.E. Raab, Measurement of the electric quadrupole moments of CO_2, CO and N_2, Molecular Physics 67 (1989) 939.
[171] T. Düren, R.Q. Snurr, Assessment of isoreticular metal-organic frameworks for adsorption separations: a molecular simulation study of methane/n-butane mixtures, The Journal of Physical Chemistry B 108 (2004) 15703.

[172] L. Zhang, Y. Yin, L. Li, F. Wang, Q. Song, N. Zhao, F. Xiao, W. Wei, Numerical simulation of CO_2 adsorption on K-based sorbent, Energy & Fuels 30 (2016) 4283.
[173] K.S. Lackner, A guide to CO_2 sequestration, Science 300 (2003) 1677.
[174] M. Grimston, V. Karakoussis, R. Fouquet, R. Van der Vorst, P. Pearson, M. Leach, The European and global potential of carbon dioxide sequestration in tackling climate change, Climate policy 1 (2001) 155.
[175] J.A. Gibson, E. Mangano, E. Shiko, A.G. Greenaway, A.V. Gromov, M.M. Lozinska, D. Friedrich, E.E. Campbell, P.A. Wright, S. Brandani, Adsorption materials and processes for carbon capture from gas-fired power plants: AMPGas, Industrial & Engineering Chemistry Research 55 (2016) 3840.
[176] G.D. Pirngruber, L. Hamon, S. Bourrelly, P.L. Llewellyn, E. Lenoir, V. Guillerm, C. Serre, T. Devic, A method for screening the potential of MOFs as CO_2 adsorbents in pressure swing adsorption processes, ChemSusChem 5 (2012) 762.
[177] D.M. Ruthven, Principles of adsorption and adsorption processes, John Wiley & Sons1984.
[178] I. Zwiebel, Fixed bed adsorption with variable gas velocity due to pressure drop, Industrial & Engineering Chemistry Fundamentals 8 (1969) 903.
[179] M.S. Shafeeyan, W.M.A.W. Daud, A. Shamiri, N. Aghamohammadi, Modeling of carbon dioxide adsorption onto ammonia-modified activated carbon: Kinetic analysis and breakthrough behavior, Energy & Fuels 29 (2015) 6565.
[180] R. Sabouni, H. Kazemian, S. Rohani, Mathematical modeling and experimental breakthrough curves of carbon dioxide adsorption on metal organic framework CPM-5, Environmental science & technology 47 (2013) 9372.
[181] N. Al-Janabi, P. Hill, L. Torrente-Murciano, A. Garforth, P. Gorgojo, F. Siperstein, X. Fan, Mapping the Cu-BTC metal–organic framework (HKUST-1) stability envelope in the presence of water vapour for CO_2 adsorption from flue gases, Chemical Engineering Journal 281 (2015) 669.
[182] A.M. Ribeiro, C.A. Grande, F.V.S. Lopes, J.M. Loureiro, A.E. Rodrigues, A parametric study of layered bed PSA for hydrogen purification, Chemical Engineering Science 63 (2008) 5258.

[183] R. Krishna, J.R. Long, Screening metal–organic frameworks by analysis of transient breakthrough of gas mixtures in a fixed bed adsorber, The Journal of Physical Chemistry C 115 (2011) 12941.
[184] V.P. Mulgundmath, R.A. Jones, F.H. Tezel, J. Thibault, Fixed bed adsorption for the removal of carbon dioxide from nitrogen: Breakthrough behaviour and modelling for heat and mass transfer, Separation and Purification Technology 85 (2012) 17.
[185] W. Won, S. Lee, K.-S. Lee, Modeling and parameter estimation for a fixed-bed adsorption process for CO_2 capture using zeolite 13X, Separation and purification technology 85 (2012) 120.
[186] S. Najafi Nobar, S. Farooq, Experimental and modeling study of adsorption and diffusion of gases in Cu-BTC, Chemical Engineering Science 84 (2012) 801.
[187] B. Silva, I. Solomon, A.M. Ribeiro, U.-H. Lee, Y.K. Hwang, J.-S. Chang, J.M. Loureiro, A.E. Rodrigues, H2 purification by pressure swing adsorption using CuBTC, Separation and Purification Technology 118 (2013) 744.
[188] A.-M. Banu, D. Friedrich, S. Brandani, T. Düren, A Multiscale study of MOFs as adsorbents in H2 PSA purification, Industrial & Engineering Chemistry Research 52 (2013) 9946.
[189] W.J. Thomas, B.D. Crittenden, Adsorption technology and design, Butterworth-Heinemann1998.
[190] J. Delgado, A critical review of dispersion in packed beds, Heat and mass transfer 42 (2006) 279.
[191] S. Walas, Chemical process equipment-selection and design, 1990.
[192] G.S. Bohart, E.Q. Adams, Some aspects of the behaviours of charcoal with repect chlorine Journal of the American Chemical Society 42 (1920) 523.
[193] D.O. Cooney, Adsorption design for wastewater treatment, CRC Press1998.
[194] K. Chu, M. Hashim, Copper biosorption on immobilized seaweed biomass: column breakthrough characteristics, Journal of Environmental Sciences 19 (2007) 928.
[195] Z. Lou, H. Huang, M. Li, T. Shang, C. Chen, Controlled synthesis of carbon nanoparticles in a supercritical carbon disulfide system, Materials 7 (2013) 97.
[196] L. Wang, X. Li, J. Ma, Q. Wu, X. Duan, Non-activated, N, S-co-doped biochar derived from banana with superior capacitive properties, Sustainable Energy 2 (2014) 39.

[197] A. Fenghour, W.A. Wakeham, V. Vesovic, The viscosity of carbon dioxide, Journal of Physical and Chemical Reference Data 27 (1998) 31.
[198] E.R. Monazam, J. Spenik, L.J. Shadle, Fluid bed adsorption of carbon dioxide on immobilized polyethylenimine (PEI): Kinetic analysis and breakthrough behavior, Chemical Engineering Journal 223 (2013) 795.
[199] A. Malek, S. Farooq, M.N. Rathor, K. Hidajat, Effect of velocity variation due to adsorption-desorption on equilibrium data from breakthrough experiments, Chemical Encjineering Science 50 (1995) 737.
[200] N. Al-Janabi, A. Alfutimie, F. Siperstein, X. Fan, Underlying mechanism of the hydrothermal instability of HKUST-1 metal-organic framework, Frontiers of Chemical Science and Engineering 10 (2016) 103.
[201] A. Gonciaruk, K. Althumayri, W.J. Harrison, P.M. Budd, F.R. Siperstein, PIM-1/graphene composite: a combined experimental and molecular simulation study, Microporous and Mesoporous Materials 209 (2015) 126.
[202] A. Gonciaruk, F.R. Siperstein, In silico designed microporous carbons, Carbon 88 (2015) 185.
[203] C. Campbell, C.A. Ferreiro-Rangel, M. Fischer, J.R. Gomes, M. Jorge, A transferable model for adsorption in MOFs with unsaturated metal sites, The Journal of Physical Chemistry C 121 (2016) 441.
[204] L. Ding, A.Ö. Yazaydin, How well do metal–organic frameworks tolerate flue gas impurities?, The Journal of Physical Chemistry C 116 (2012) 22987.
[205] D. Frenkel, B. Smit, Understanding molecular simulation, Academic Press, San Diego, 1996.
[206] J.J. Potoff, a.J.I. Siepmann, Vapor–liquid equilibria of mixtures containing alkanes, carbon dioxide, and nitrogen, AIChE Journal 47 (2001) 1676.
[207] K.S. Walton, R.Q. Snurr, Applicability of the BET method for determining surface areas of microporous metal-organic frameworks, Journal of the American Chemical Society 129 (2007) 8552.
[208] C.D. Wood, B. Tan, A. Trewin, H. Niu, D. Bradshaw, M.J. Rosseinsky, Y.Z. Khimyak, N.L. Campbell, R. Kirk, E. Stöckel, A.I. Cooper, Hydrogen storage in microporous hypercrosslinked organic polymer networks, Chemistry of Materials 19 (2007) 2034.

[209] A.-M. Banu, Molecular simulation studies of metal organic frameworks focusing on hydrogen purification (PhD thesis), Institute for Materials and Processes, The University of Edinburgh, Edinburgh Research Archive, 2014.
[210] D. Farrusseng, C. Daniel, C. Gaudillere, U. Ravon, Y. Schuurman, C. Mirodatos, D. Dubbeldam, H. Frost, R.Q. Snurr, Heats of adsorption for seven gases in three metal-organic frameworks: systematic comparison of experiment and simulation, Langmuir 25 (2009) 7383.
[211] M. Thommes, K.A. Cychosz, Physical adsorption characterization of nanoporous materials: progress and challenges, Adsorption 20 (2014) 233.
[212] E.A. Ustinov, D.D. Do, Application of density functional theory to analysis of energetic heterogeneity and pore size distribution of activated carbons, Langmuir 20 (2004) 3791.
[213] A.K. Rappe, W.A.G. III, Charge equilibration for molecular dynamics simulations, The Journal of Physical Chemistry 95 (1991) 3358.
[214] L. Shen, S.W. Yang, S. Xiang, T. Liu, B. Zhao, M.F. Ng, J. Goettlicher, J. Yi, S. Li, L. Wang, J. Ding, B. Chen, S.H. Wei, Y.P. Feng, Origin of long-range ferromagnetic ordering in metal-organic frameworks with antiferromagnetic dimeric-Cu(II) building units, Journal of the American Chemical Society 134 (2012) 17286.
[215] T. Düren, F. Millange, G. Ferey, K.S. Walton, R.Q. Snurr, Calculating geometric surface areas as a characterization tool for metal-organic frameworks, The Journal of Physical Chemistry C 111 (2007) 15350.
[216] P. Kowalczyk, A.P. Terzyk, P.A. Gauden, R. Leboda, E. Szmechtig-Gauden, G. Rychlicki, Z. Ryu, H. Rong, Estimation of the pore-size distribution function from the nitrogen adsorption isotherm. Comparison of density functional theory and the method of Do and co-workers, Carbon 41 (2003) 1113.

Appendix A

A.1 BET surface area calculations

The nitrogen adsorption isotherm at –196 ºC was carried out in order to evaluate the specific surface area of samples. The surface area is an important parameter for monitoring the activity of adsorbents. The multipoint method of Brunauer, Emmett, and Teller (BET) is used for the determination of the specific surface area. BET is basically followed the monolayer Langmuir's model but it was derived as a multilayer adsorption isotherm in which, the same producing forces of adsorption are chiefly responsible for the binding energy of a multilayer formation, which may take place even before the full coverage of the monolayer. The final result of their model relates the volume of gas-adsorbed v_m with the pressure *P,* and it is given by:

$$\frac{P}{v(P^\circ - P)} = \frac{1}{v_m c} + \frac{c-1}{v_m c}\frac{P}{P^\circ} \tag{A.1}$$

where v_m represents the amount of adsorbent in a complete monolayer coverage (m^3/mol), and c is a constant related to the difference in the heat of adsorption of the first layer adsorbate and that of the other layers.

Eq (A.1) is a convenient form to calculate the two constants v_m and *c*. The plot of $P/v(P^o - P)$ *versus* P/P^o shows a linear relation over the relative pressure range of ($0.05 < P/P^o < 0.35$), in which the intercept is ($1/v_m c$) and the slope is ($c - 1$)/($1/v_m c$).

The BET surface area of the sample can be then obtained from Eq (A.2).

$$S_{BET.total} = \frac{v_m \cdot \mathrm{N} \cdot S}{v} \tag{A.2}$$

where N is Avogadro's number = 6.022×10^{23} (1/mol), S is the adsorption cross section = 0.162×10^{-18} (m^2), for N_2, v the molar volume of adsorbed gas = 0.022414 (m^3/mol) for N_2.

A.2 Yield Calculations

$$\text{Yield}\% = \frac{\text{Actual produced mass}}{\text{Theoretical mass}} \tag{A.3}$$

$3\ Cu(NO_3)_2.3H_2O + 2\ C_6H_3(CO_2H)_3 \rightarrow Cu_3(BTC)_2 + 6\ HNO_3$

Reactants used: 3.6 mmol of cupric nitrate tri hydrate, and 1.99 mmol of BTC.

Limiting reactant:

$$\frac{3 \text{ mmol of cupric nitrate tri hydrate}}{x} = \frac{2 \text{ mmol of BTC}}{1.99} \tag{A.4}$$

$x = 2.985\ mmol$ (cupric nitrate required for the reaction with 1.99 mmol of BTC), while 3.6 mmol is used in the reaction. *i.e.* BTC is the limiting reactant which will be used to calculate the yield.

$$\frac{2 \text{ mole of BTC}}{1.99} = \frac{1 \text{ mole of CuBTC produced}}{y}$$

(A.5)

y= 1 mmol of CuBTC will be produced for each 1.99 mmol of BTC reacted.

Theoretical mass of CuBTC produced = 1 mmol x 604.87 (mg/mmol)

= 604.87mg ~ 0.605 g

0.605 g (theoretical mass) to be used in Eq A.3 with the actual activated mass measured after the experiment.

A.3 Comparison of the crystallinity of the synthesised CuBTC samples to commercial sample

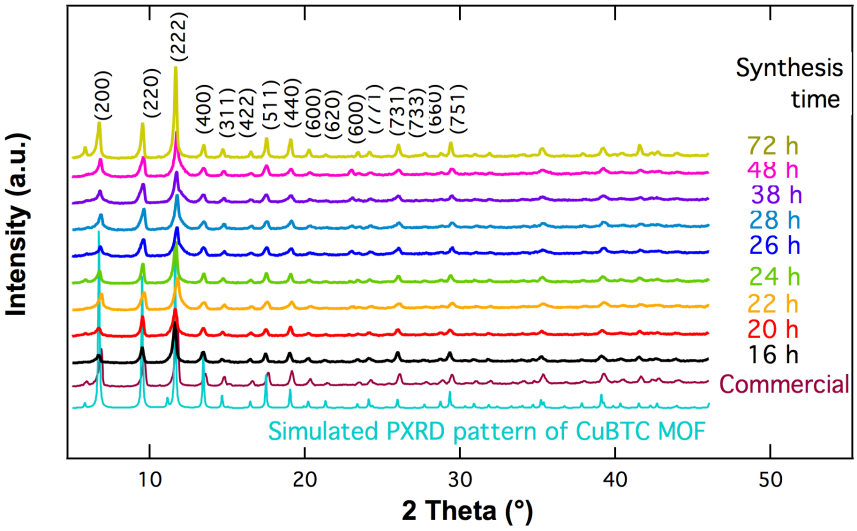

Figure A.1. Comparison of powder X-ray diffraction patterns of synthesised samples of CuBTC MOF t a commercial sample purchased from MOF Technologies company.

A.4 Repeatability test of measuring CO_2 adsorption: An example of CO_2 adsorption on CuBTC MOF

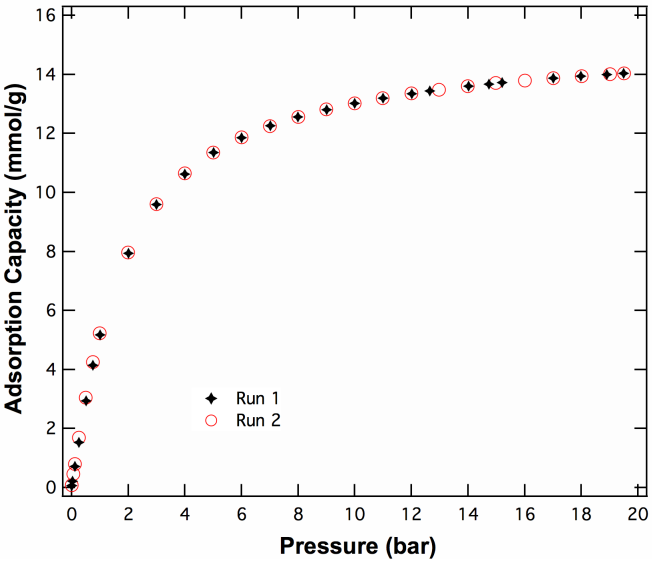

Figure A.1. Experimental CO_2 adsorption isotherm on CuBTC MOF at 25 ºC.

A.5 Water vapour adsorption isotherms and heat of adsorption on CuBTC MOF

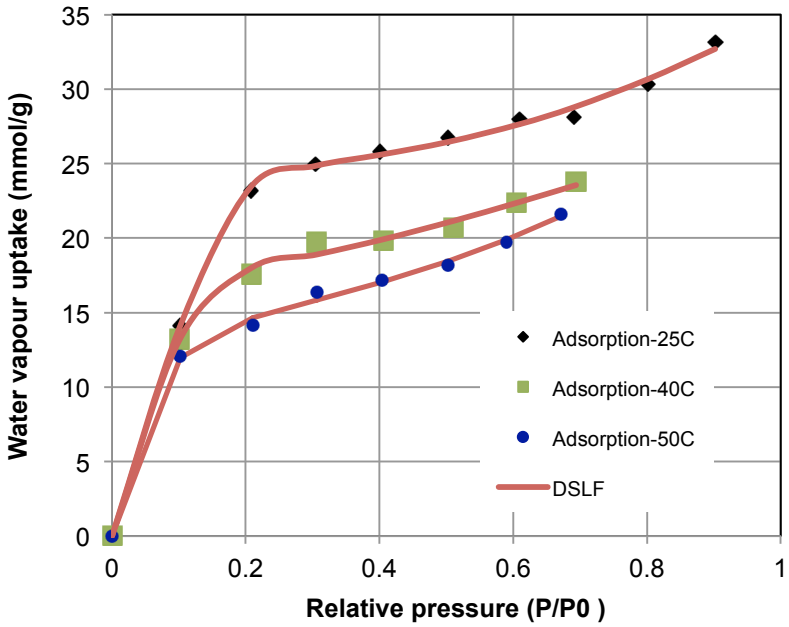

Figure A.2. Experimental water vapour adsorption isotherm on CuBTC MOF at 25 ºC, 40 ºC, and 50 ºC in comparison to DSLF theoretical model.

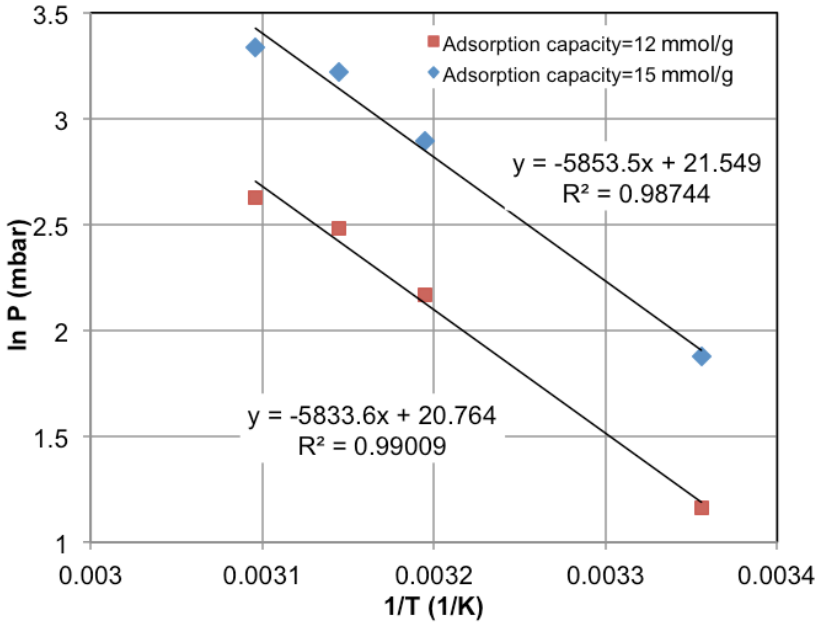

Figure A.3. Determination of heat of adsorption of water vapour adsorption onto CuBTC MOF at adsorption capacity of 12 and 15 mmol/g.

A.6 Determination of weight percent of glycine in Gly-CuBTC MOFs

Basis of 1 g of CuBTC MOF

wt.% of copper in CuBTC = 31.5 %

Mass of copper in CuBTC = 1 × 0.135 = 0.135 g

$$\frac{0.315\ g}{63.546\frac{g}{mol}} = 4.957\times10^{-3}\ mol\ of\ copper\ in\ CuBTC \times Avogadro's\ number$$

$$= 2.984\times10^{21}\ atom\ of\ copper\ in\ CuBTC$$

Assume to saturate all OMSs in CuBTC MOF, one needs 1 molecule of glycine for 1 atom of copper.

Therefore, to fully saturate OMSs, total molecules of glycine needed = 2.984×10^{21} molecule.

$$\frac{2.984\times10^{21}}{6.022\times10^{23}} = 4.955\times10^{-3}\ mol\ of\ glycine \times 75.06\ g/mol$$

= 0.372 g

Therefore, 0.372 g of glycine is needed to saturate all copper atoms in 1 g of CuBTC MOF. Hence, the weight percent of glycine in the molecular glycine saturated Gly-CuBTC MOF can be calculated as:

$$\frac{0.372\ g\ of\ glycine}{0.372\ g\ of\ glycine + 1\ g\ of\ CuBTC} = 27.1\ wt\ \% + ca.1\%\ added\ as\ excess = 28\%$$

A.7 Micro GC calibration

A micro GC (Agilent Technologies 490 Micro GC) with a Pora PLOT U (PPU) column and a thermal conductivity detector (TCD) for in-line analysis of outlet gases was used. The Porous Layer Open Tubular (PLOT) column is an open column coated with a layer of porous solid materials on the inside column wall. The method of separation in micro GC is physical in which the mobile phase *i.e.* gas is adsorbed on a solid stationary phase (PLOT column). The properties of column and conditions of micro GC instrument are given in Table A.1.

Table A.1
Agilent 490 micro GC conditions.

Column	10 m PPU heated injector
Column temperature	80 ºC
Carrier gas	Helium, 150 kPa
Pressure mode	Static
Injector temperature	110 ºC
Injection time	40 ms
Detector sensitivity	Auto
Sample line temperature	110 ºC
Sample time	10 s
Stabilising time	5 s

At the outlet of the column, after separating the gases in the column into individual compounds, the carrier gas together with the separated gases will elute into a thermal conductivity detector (TCD). At this stage, the gases are measured based on their difference in thermal conductivity with respect to the carrier gas and quantified by measuring their peak area. For the purpose of calibration, mass flow controller (Alicat scientific MC-series, ± 5% accuracy) of 20 cm^3/min total flow was used.

Preliminary analyses of pure gases (CO_2 and N_2) were performed to determine the retention time of each gas using helium gas as the carrier gas, where both gases are eluted with less than 60 s. Table A.2 and Figure A.3 show the calibration data and the calibration curve, respectively, for CO_2 gas, in which, its retention time is 44.7 s. The calibration data and the calibration curve, respectively, for N_2 gas, are

shown in Table A.3 and Figure A.4, in which, its retention time is 26.8 s. For each calibration point, two separate runs were performed then the average area was used. Figure A.3 and A.4 show excellent calibration curves for CO_2 and N_2, where for linear regression of both gases, the R-squared is perfect.

Table A.2
Micro GC calibration data of CO_2.

He (cm^3/min)	CO_2 (cm^3/min)	Total (cm^3/min)	$\%CO_2$	Average area of CO_2
475.0	0.1	475.1	0.0	41091.5
475.0	0.3	475.3	0.1	95976.5
475.0	0.5	475.5	0.1	171543.0
400.0	1.0	401.0	0.2	393766.0
475.0	2.5	477.5	0.5	818261.0
475.0	5.0	480.0	1.0	1601627.5
475.0	10.0	485.0	2.1	3149864.5
475.0	20.0	495.0	4.0	6206705.0

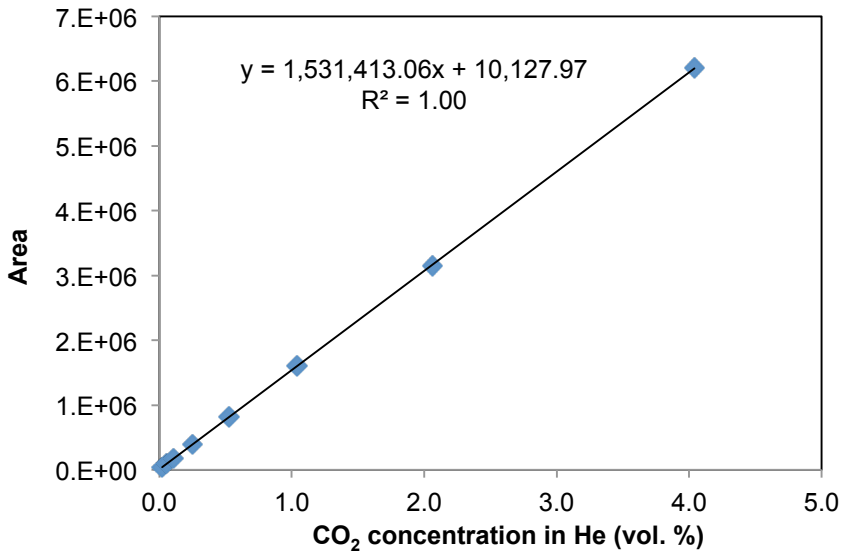

Figure A.4. Micro GC calibration data of CO_2.

Table A.3

Micro GC calibration data of N_2.

He (cm^3/min)	N_2 (cm^3/min)	Total (cm^3/min)	$\%N_2$	Average area of N_2
475.0	0.1	0.1	475.1	41091.5
475.0	0.3	0.3	475.3	95976.5
475.0	0.5	0.5	475.5	171543.0
400.0	1.0	1.0	401.0	393766.0
475.0	2.5	40.0	477.5	818261.0
475.0	5.0	40.0	480.0	1601627.5
475.0	10.0	40.0	485.0	3149864.5
475.0	20.0	40.0	495.0	6206705.0

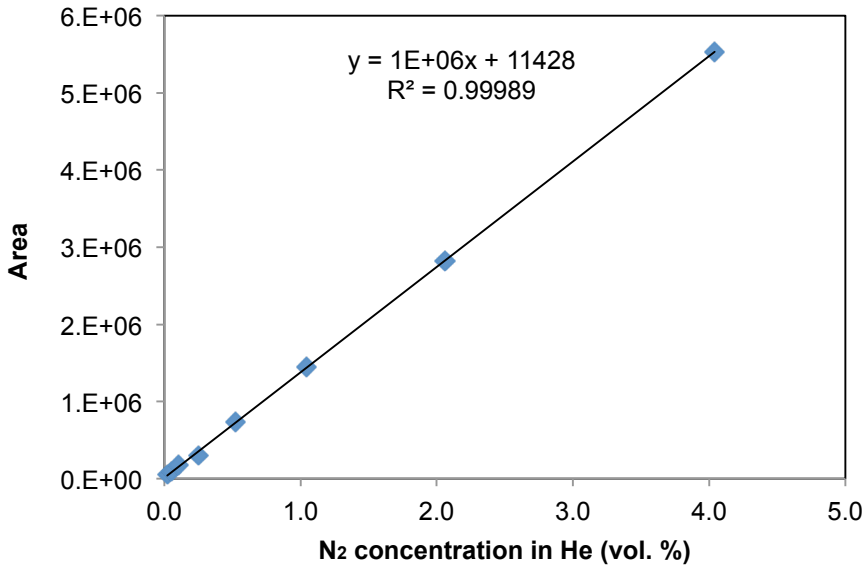

Figure A.5. Micro GC calibration data of N_2.

A.8 Matlab model solution flow chart

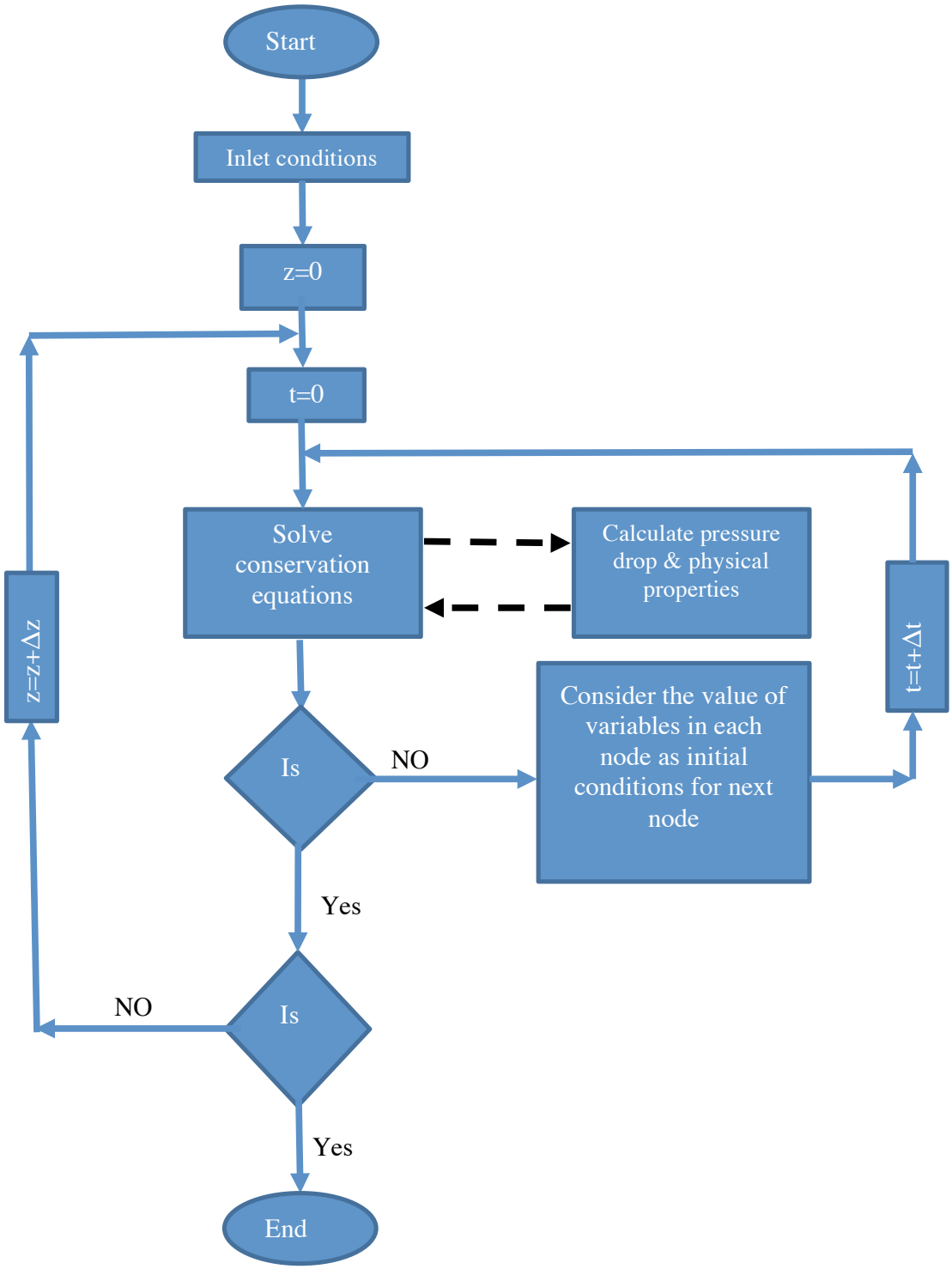

A.9 Repeatability test of measuring breakthrough curves for CO_2 adsorption: An example of CO_2 adsorption on bulk AC

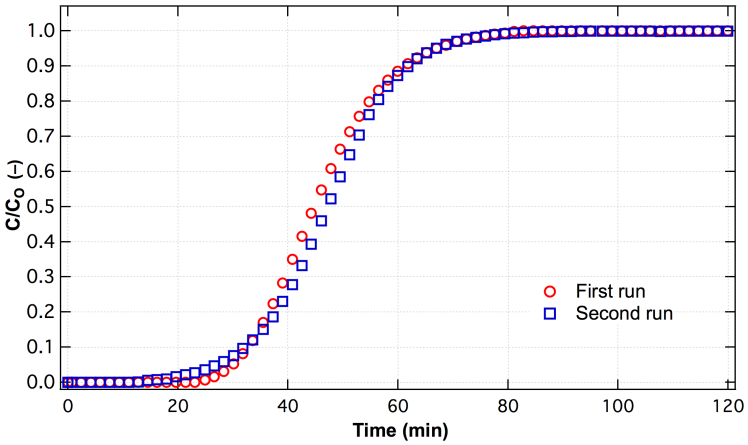

Figure A.6. Repeatability test of measuring breakthrough curves for CO_2 adsorption onto bulk AC from CO_2:N_2 mixture (50:50) at 10 cm^3/min and T = 50 °C.

A.10 Linear fit of experimental breakthrough curve: An example of CO_2 adsorption on bulk AC

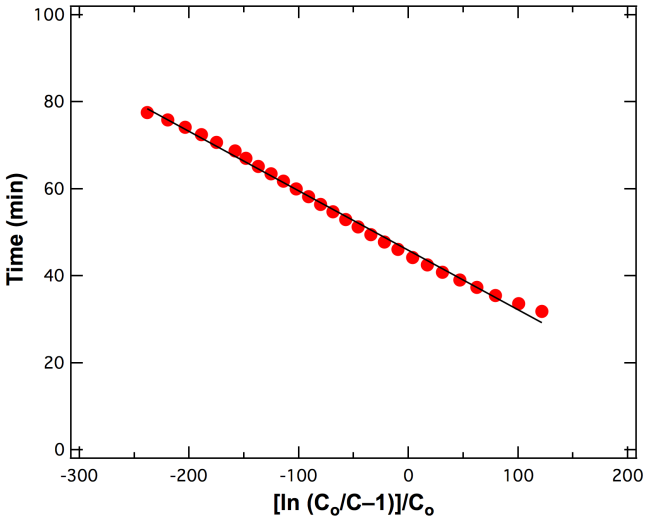

Figure A.7. Linear fit of experimental breakthrough curve of CO_2 adsorption onto bulk AC from CO_2:N_2 mixture (50:50) at 10 cm^3/min and T = 50 °C.

A.11 Comparison of t_{b50} values from experimental and simulated Matlab model breakthrough curves

Table A.4

Comparison of t_{b50} values from experiments and model simulation.

Flow rate		t_{b50}	Matlab model	t_{b50}
10 cm^3/min	Experimental	48.4	Variable velocity	49.3
	B-A model	62.4	Constant velocity	63.1
20 cm^3/min	Experimental	24.1	Variable velocity	25.0
	B-A model	31.1	Constant velocity	31.9
100 cm^3/min	Experimental	5.0	Variable velocity	5.0
	B-A model	6.0	Constant velocity	6.4

A.12 Propagation velocity equation derivation

Component mass balance,

$$-\varepsilon D_L \frac{\partial^2 C_i}{\partial z^2} + \varepsilon \frac{\partial C_i}{\partial t} + \frac{\partial \left(uC_i\right)}{\partial z} + \left(1-\varepsilon\right)\rho_g \frac{\partial q_i}{\partial t} = 0 \tag{A.6}$$

Assuming that the axial dispersion is negligible, yields:

$$\varepsilon \frac{\partial C_i}{\partial t} + \frac{\partial \left(uC_i\right)}{\partial z} + \left(1-\varepsilon\right)\rho_g \frac{\partial q_i}{\partial t} = 0 \tag{A.7}$$

where *u* is the superficial velocity of the gas.

Overall material balance at constant column pressure,

$$C\frac{\partial u}{\partial z} + \left(1-\varepsilon\right)\rho_g \sum_{i=1}^{n} \frac{\partial q_i}{\partial t} = 0 \tag{A.8}$$

where *C* is the total concentration ($C = y_i C_i$). Combining Eq A.7 and A.8 gives:

$$\varepsilon \frac{\partial C_i}{\partial t} + u\frac{\partial C_i}{\partial z} - y_i\left(1-\varepsilon\right)\rho_g \sum_{i=1}^{n} \frac{\partial q_i}{\partial t} + \left(1-\varepsilon\right)\rho_g \frac{\partial q_i}{\partial t} = 0 \tag{A.9}$$

$$\left(\frac{\partial q_i}{\partial t}\right)_z = \frac{\partial q_i^*}{\partial C_i}\left(\frac{\partial C_i}{\partial t}\right)_z \tag{A.10}$$

where $q^* = f(C)$

$$\frac{\partial q_1}{\partial t} = C\frac{\partial q_1^*}{\partial C_1}\frac{\partial y_1}{\partial t}, \quad \frac{\partial q_2}{\partial t} = -C\frac{\partial q_2^*}{\partial C_2}\frac{\partial y_1}{\partial t} \tag{A.11}$$

Eq (A.11) becomes (for component 1):

$$u\frac{\partial y_1}{\partial z} + \frac{\partial y_1}{\partial t}\{\varepsilon + (1-\varepsilon)\rho_g[(1-y_1)\frac{\partial q_1^*}{\partial C_1} + y_1\frac{\partial q_2^*}{\partial C_2}]\} = 0 \tag{A.12}$$

Eq (A.12) can be solved in terms of propagation velocity *w*, as follows:

$$w(C) = (\frac{\partial z}{\partial t})_C = -\frac{(\partial C/\partial t)_z}{(\partial C/\partial z)_t} = \frac{u}{\varepsilon + (1-\varepsilon)\rho_g[(1-y_1)\frac{\partial q_1^*}{\partial C_1} + y_1\frac{\partial q_2^*}{\partial C_2}]} \tag{A.13}$$

Assuming that component 2 (nitrogen) is not absorbable gas, then $(\partial q_2^*/\partial C_2)$. Hence, the propagation velocity (*w*) will only vary with composition of the absorbable gas, Eq A.14.

$$w(C) = \frac{u}{\varepsilon + (1-\varepsilon)\rho_g(1-y_1)\frac{\partial q_1^*}{\partial C_1}} \tag{A.14}$$

In case of using Langmuir model adsorption isotherm, then substituting for $(\partial q^*/\partial C)$ gives:

$$w = \frac{u}{\varepsilon + (1-\varepsilon)\rho_g(1-y_1)\frac{K_1 n_{s,1}}{(1+K_1 C y_1)^2}} \tag{A.15}$$

$$w = \frac{u_n}{1 + (\frac{1-\varepsilon}{\varepsilon})\rho_g(1-y_i)\frac{K_i n_{s,i}}{(1+K_i C y_i)^2}} \tag{A.16}$$

where u_n is the interstitial velocity of the gas.

A.13 Error in total amount adsorbed when considering constant velocity

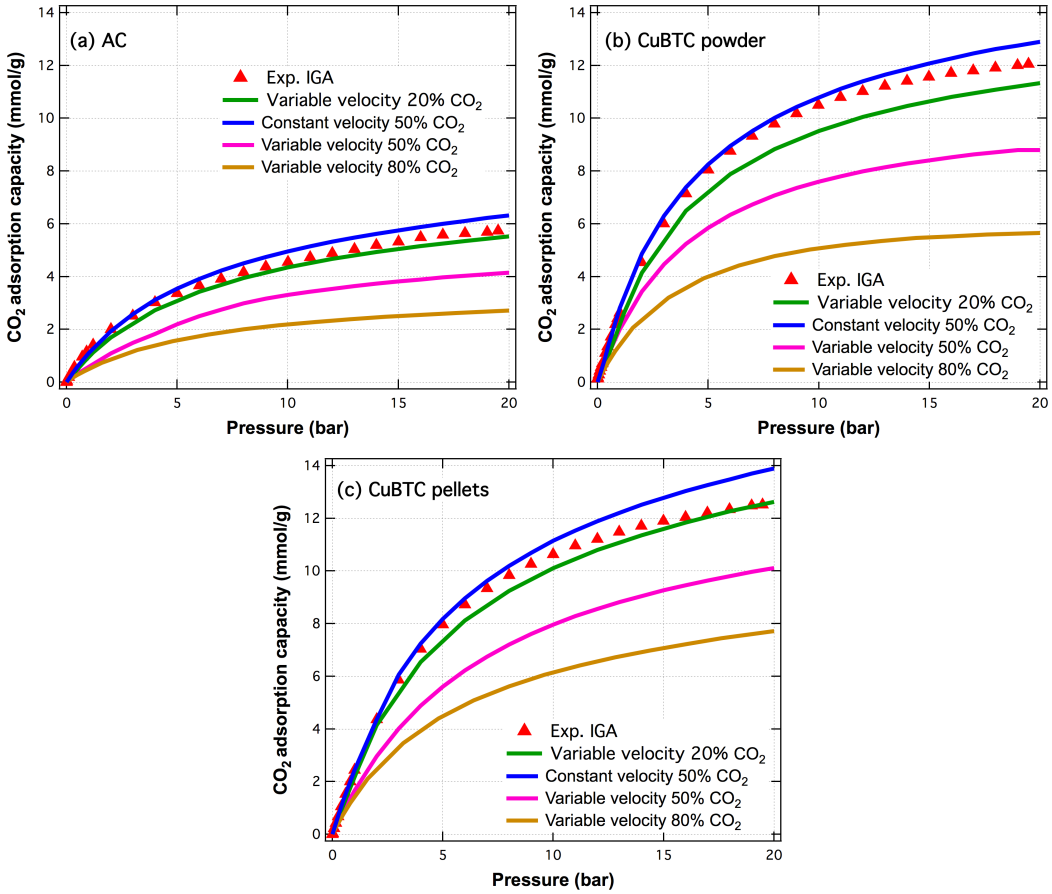

Figure A.8. Deviation in CO_2 adsorption isotherms at 50 ºC for (a) Bulk AC, (b) Bulk CuBTC MOF, (c) Pelleted CuBTC MOF when corrections for variable velocity are not applied in the estimation of the total amount adsorbed.